

UNDERSTANDING STRUCTURE-PROPERTY RELATIONS IN  $\beta$ -EUCRYPTITE UNDER  
PRESSURE AND AT ELEVATED TEMPERATURE

by

Yachao Chen

A thesis submitted to the faculty and the Board of Trustees of the Colorado School of Mines in partial fulfillment of the requirements for the degree of Doctor of Philosophy (Materials Science)

Golden, Colorado

Date: \_\_\_\_\_

Signed: \_\_\_\_\_

Yachao Chen

Signed: \_\_\_\_\_

Dr. Ivar E. Reimanis

Thesis Advisor

Golden, Colorado

Date: \_\_\_\_\_

Signed: \_\_\_\_\_

Dr. Angus Rockett

Professor and Department Head

Department of Metallurgical and Materials Engineering

## ABSTRACT

$\beta$ -eucryptite ( $\text{LiAlSiO}_4$ ) has received widespread attention from both industry and academia due to its negative coefficient of thermal expansion (CTE) and one-dimensional Li ionic conductivity. Additionally,  $\beta$ -eucryptite undergoes a pressure-induced phase transformation at relatively low pressures. These various behaviors arise because the crystal structure is open and highly anisotropic. The present study uses several experimental methods to better understand the relation between the structure and the electrical and mechanical behavior of  $\beta$ -eucryptite.

Synthesis and processing methods were developed to make pure  $\beta$ -eucryptite and  $\beta$ -eucryptite doped with Mg of varying particle sizes. *In-situ* diamond anvil cell - x-ray diffraction was performed to study the pressure induced phase transformation from  $\beta$ -eucryptite to the high pressure phase  $\epsilon$ -eucryptite. With the assistance of Rietveld refinement and atomistic modeling, the crystal structure of the  $\epsilon$ -eucryptite was determined to be an orthorhombic with space group  $\text{Pna}2_1$ . This is the first time that both space group and atomic positions of the high pressure phase have been reported. It is also observed that Mg-doped  $\beta$ -eucryptite undergoes the pressure induced transformation at slightly higher pressures than pure  $\beta$ -eucryptite (2.47 GPa compared with 1.8 GPa hydrostatic stress), implying that Mg stabilizes  $\beta$ -eucryptite. Furthermore, the presence of Mg leads to a state in which two high pressure phases coexist. It was observed that the critical pressure for transformation to the high pressure phase decreases with increasing  $\beta$ -eucryptite grain size, up to a critical grain size beyond which grain size does not play a role. The experimental results were described by a nucleation and growth model for transformation.

The effect of structural changes in  $\beta$ -eucryptite from low to high temperature was examined by measuring the Li ionic conductivity with electrochemical impedance spectroscopy

(EIS). The conductivity is strongly influenced by the Li order-disorder transition at  $\sim 500$  °C where the activation energy dramatically increases. It is shown that the conductivity depends on whether or not the Li ions motion is correlated or uncorrelated, leading to three activation energies: at low temperatures it is correlated, at  $\sim 500$  °C it is uncorrelated and at high temperatures it is correlated again.

The present study focuses on measuring the material properties under pressure and at high temperature, separately. These measurements provide the first step towards elucidating the relation between mechanical and electrical properties. The order-disorder transition is caused by the rearrangement of Li ions at evaluated temperature, an event which is expected to influence the pressure-induced phase transformation. Specifically, a change in the size of the Li channels resulting from Li redistribution, is expected to modify the phase transformation pressure.

## TABLE OF CONTENTS

|                       |   |      |
|-----------------------|---|------|
| ABSTRACT.....         |   | iii  |
| LIST OF FIGURES ..... |   | viii |
| LIST OF TABLES.....   |   | xiii |
| ACKNOWLEDGEMENTS..... |   | xiv  |
| CHAPTER 1             | GENERAL INTRODUCTION.....   | 1    |
| 1.1                   | Motivation.....   | 2    |
| 1.2                   | Thesis organization .....   | 3    |
| CHAPTER 2             | LITERATURE REVIEW .....   | 7    |
| 2.1                   | Materials Overview.....   | 7    |
| 2.2                   | Negative coefficient of thermal expansion .....   | 9    |
| 2.3                   | Pressure-induced phase transformation .....   | 12   |
| 2.4                   | Grain size effect on pressure-induced phase transformation .....  | 15   |
| 2.5                   | Li ionic conductivity-order-disorder transition.....  | 24   |
| CHAPTER 3             | EXPERIMENTS .....   | 28   |
| 3.1                   | Synthesis and processing .....  | 28   |
| 3.2                   | Diamond anvil cell introduction and calibration .....   | 37   |
| 3.3                   | <i>In-situ</i> DAC-X-ray diffraction .....  | 55   |
| 3.4                   | <i>In-situ</i> DAC-Raman spectroscopy .....   | 59   |
| 3.5                   | Rietveld refinement.....  | 60   |
| 3.6                   | Electrochemical Impedance Spectroscopy technique.....   | 65   |
| CHAPTER 4             | PRESSURE-INDUCED PHASE TRANSFORMATION IN $\beta$ -<br>EUCRYPTITE: AN X-RAY DIFFRACTION AND DENSITY<br>FUNCTIONAL THEORY STUDY ..... | 73   |

|           |   |     |
|-----------|---|-----|
| 4.1       | Abstract.....   | 73  |
| 4.2       | Introduction.....   | 73  |
| 4.3       | Experimental Method.....  | 75  |
| 4.4       | Results and discussions.....  | 78  |
| 4.5       | Conclusions.....  | 85  |
| 4.6       | Acknowledgement .....   | 86  |
| 4.7       | Supplemental material .....   | 86  |
| CHAPTER 5 | GRAIN SIZE EFFECT ON THE PRESSURE INDUCED PHASE<br>TRANSFORMATION OF $\beta$ -EUCRYPTITE..... | 94  |
| 5.1       | Abstract.....   | 94  |
| 5.2       | Introduction.....   | 94  |
| 5.3       | Experimental procedure .....  | 96  |
| 5.4       | Results.....  | 98  |
| 5.5       | Discussion.....   | 99  |
| 5.6       | Conclusion .....  | 107 |
| 5.7       | Acknowledgement .....   | 107 |
| CHAPTER 6 | THERMAL REGIMES OF LI-ION CONDUCTIVITY OF $\beta$ -<br>EUCRYPTITE .....                       | 108 |
| 6.1       | Abstract.....   | 108 |
| 6.2       | Introduction.....   | 109 |
| 6.3       | Experimental procedure .....  | 111 |
| 6.4       | Results and discussion .....  | 112 |
| 6.5       | Conclusions.....  | 123 |
| 6.6       | Acknowledgement .....   | 123 |

|            |  |     |
|------------|--|-----|
| CHAPTER 7  | GENERAL DISCUSSION .....                                   | 124 |
| 7.1        | Structural phase transformation under high pressures ..... | 124 |
| 7.2        | Order-disorder transition at high temperatures .....       | 125 |
| CHAPTER 8  | CONCLUSION.....  | 127 |
| CHAPTER 9  | SUGGESTIONS OF FUTURE WORK .....                           | 129 |
| REFERENCES | .....  | 133 |
| APPENDIX A | TRANSPORT IN AN ELECTRICAL POTENTIAL GRADIENT .....        | 156 |

## LIST OF FIGURES

|             |   |    |
|-------------|---|----|
| Figure 2.1  | Crystal structure of $\beta$ -eucryptite viewing from different directions. The blue and green tetrahedra represent $\text{SiO}_4$ and $\text{AlO}_4$ , respectively. Purple balls represent Li ions.....   | 8  |
| Figure 2.2  | The thermal expansion behavior of pure and Zn doped $\beta$ -eucryptite from room temperature and 1000 °C. Zn concentrations are from 0.5 mol% to 3 mol%.....   | 10 |
| Figure 2.3  | The thermal expansion behavior of pure and Zn doped $\beta$ -eucryptite from room temperature and 1000 °C. Zn concentrations are from 0.5 mol% to 3 mol% [50]. .....  | 11 |
| Figure 2.4  | Coordination environments of (a) channel $\text{Li}^+$ in the $\beta$ -quartz framework of $\text{LiAlSiO}_4$ and (b) $\text{Mg}^{2+}$ in the $\alpha$ -quartz framework of $\text{Mg}_{0.5}\text{AlSiO}_4$ . Tetrahedra represent $[\text{Si}/\text{AlO}_4]$ units, and spheres represent $\text{Li}^+$ or $\text{Mg}^{2+}$ [34]......   | 12 |
| Figure 2.5  | Schematic showing the various phase transformation in $\beta$ -eucryptite .....   | 13 |
| Figure 2.6  | Hierarchy of seven crystal systems .....  | 15 |
| Figure 2.7  | Variation of $\Delta G$ with $r$ for a homogeneous nucleus. $\Delta G^*$ represents the activation energy barrier. ....   | 17 |
| Figure 2.8  | Schematic showing that the strain and stress on matrix and particles after transformation. ....   | 19 |
| Figure 2.9  | Schematic describes transformation toughening mechanism using $\text{ZrO}_2$ as an example. In a tetragonal zirconia dispersed ceramic matrix, the stress field advancing ahead of a propagating crack transforms the small tetragonal particles to larger monoclinic particles. The larger transformed monoclinic particles apply a crack-closing force in the process zone, effectively resisting the crack propagation. .... | 21 |
| Figure 2.10 | Reaction coordinate diagram showing energetics of $t$ - $m$ transformation. The reaction coordinate is any variable defining the reaction path such as pressure . ....  | 21 |
| Figure 2.11 | Schematic representation of the various free energy forms associated with the tetragonal to monoclinic transformation with different initial particle sizes: S, small; C, critical; L, large, and uncon, unconstrained [70]......   | 22 |



|             |   |    |
|-------------|---|----|
| Figure 2.12 | Li ionic conductivity of $\beta$ -eucryptite compared with other crystalline lithium-ion conductors [98], [104]–[108].  | 25 |
| Figure 3.1  | A flow chart that describes the major steps for preparing $\beta$ -eucryptite using chemical solution technique.  | 31 |
| Figure 3.2  | Particle size analysis on as calcined powders and powders after ball milling.   | 32 |
| Figure 3.3  | A flow chart that describes the major steps for preparing $\beta$ -eucryptite using EDTA-citrate method.  | 34 |
| Figure 3.4  | Image showing the transparent solution that has $\beta$ -eucryptite compositions.   | 35 |
| Figure 3.5  | Single phase confirmation from XRD on different synthesis routes.   | 35 |
| Figure 3.6  | SEM image of $\beta$ -eucryptite powders synthesized from wet-chemistry method after calcination.   | 36 |
| Figure 3.7  | SEM image showing the microstructure of the cross section of $\beta$ -eucryptite pellet processed from hot press sintering.   | 37 |
| Figure 3.8  | Schematic description of using diamond culets to create pressure on samples.  | 38 |
| Figure 3.9  | Schematic of a stainless steel gasket which placed between the two diamond culets.  | 39 |
| Figure 3.10 | Ruby fluorescence spectra under pressure  | 42 |
| Figure 3.11 | Ruby R lines shifts under temperature. The arrow points the direction of increasing temperature and the highest temperature in this calibration is 250 °C.  | 46 |
| Figure 3.12 | The relations of Ruby R peak positions and temperature from 25 °C to 250 °C. The equations represent the fitting of R positions as a function of temperature, which can be used to calculate the temperature coefficient of Ruby. | 46 |
| Figure 3.13 | The fluorescence spectrum of $\text{SrB}_4\text{O}_7: \text{Sm}^{2+}$ excited by a 532 nm laser.  | 47 |
| Figure 3.14 | $\text{SrB}_4\text{O}_7: \text{Sm}^{2+}$ peak position as a function of pressure  | 48 |
| Figure 3.15 | Misaligned diamonds culets and how they look like from the top of the cell.   | 53 |

|             |   |    |
|-------------|---|----|
| Figure 3.16 | Assembling the diamond anvil cell for high temperature tests. ....  | 55 |
| Figure 3.17 | Schematic diagram showing the output of synchrotron radiation from bending magnets. ....  | 57 |
| Figure 3.18 | Schematic of the diffraction and optical system.....  | 58 |
| Figure 3.19 | A sample of Debye-Scherrer ring that collected from CHESS B1 station.....   | 59 |
| Figure 3.20 | Schematic showing the beam path for Confocal Microscopy in reflection mode.....   | 61 |
| Figure 3.21 | A schematic showing the experimental set up for <i>in situ</i> DAC-Raman spectroscopy tests at high pressure and temperature. ....  | 62 |
| Figure 3.22 | Typical Rietveld full-profile refinement performed using the GSAS program of the X-ray diffraction pattern collect for pure $\beta$ -eucryptite. The black squares, the solid red line and the solid blue line represent an experimental pattern, modeled pattern and the difference between the observed and the refined profile, respectively. .... | 65 |
| Figure 3.23 | Fundamental impedance experiment.....   | 67 |
| Figure 3.24 | Sinusoidal voltage input $V$ at a single frequency $f$ and current response $I$ .....   | 67 |
| Figure 3.25 | Complex impedance plot.....   | 69 |
| Figure 3.26 | Schematic shows the two path ways for conduction. Path 1 represents the case that conduction in grain bulk is much higher than in grain boundary. Path 2 indicates the case when conduction along grain boundary is much higher than in grain bulk. ....  | 70 |
| Figure 3.27 | The equivalent circuit for current conducted through the bulk and grain boundary. ....  | 71 |
| Figure 3.28 | The equivalent circuit and its reduced form for current conducted along the grain boundaries only.....  | 72 |
| Figure 3.29 | Schematic of experimental setup for electrochemical impedance spectroscopy tests.....   | 72 |
| Figure 4.1  | Schematic description of experimental set up for high pressure DAC-x-ray diffraction tests.....   | 77 |

|            |  |     |
|------------|--|-----|
| Figure 4.2 | XRD patterns showing the pressure-induced phase transformation in $\beta$ -eucryptite. (a) Variation of the pattern with pressure in a loading-unloading cycle. The patterns that contain the new phase(s) are shown in black, while the $\beta$ -eucryptite is red. (b)-(d) Detail views of the main peak at three pressures around the transition, showing the main peaks (b) before, (c) during, and (d) after the transition .....80   | 80  |
| Figure 4.3 | Crystal structures of (a) $\beta$ -eucryptite and (b)-(d) three denser polymorphs and their densities at zero pressure. Al-(Si)-centered tetrahedra are shown in grey (tan), Li atoms are purple spheres.....81  | 81  |
| Figure 4.4 | Pressure-dependent enthalpy of LiAlSiO <sub>4</sub> polymorphs, with respect to the $\beta$ -eucryptite. ....82  | 82  |
| Figure 4.5 | (a)XRD pattern for the pure $\beta$ -eucryptite at 5 GPa, compared with the optimized simulated pattern for the Pna2 <sub>1</sub> phase; the other polymorphs have significant deviations from the experimental pattern. (b) XRD pattern of the Mg-doped $\beta$ -eucryptite at 5 GPa, compared with simulations of an optimized mixture of Pna2 <sub>1</sub> and Pca2 <sub>1</sub> . For clarity, only the Miller indices corresponding to Pca2 <sub>1</sub> peaks are shown in panel (b).....84  | 84  |
| Figure 4.6 | Lattice constants of P1c1, Pca2 <sub>1</sub> and Pna2 <sub>1</sub> as a function of pressure .....93   | 93  |
| Figure 5.1 | X-ray diffraction patterns for different grain size samples and the relative SEM images are shown. The increment has been kept as small as 0.1 GPa from ambient pressure to 5 GPa, thus only selected patterns at certain pressures of each sample are shown here. The grain radii are labeled on the SEM images accordingly. The peak at $2\theta=14^\circ$ existing in certain patterns indicates the diffraction from the high-pressure-cell metal gasket. S1 was prepared by long time ball milling, which results in fine grains, whereas S2, S3 and S4 were as-calcined samples.....98 | 98  |
| Figure 5.2 | Schematic description of a grain before and after phase transformation. ....102  | 102 |
| Figure 5.3 | The change in enthalpy in going from $\beta$ to $\epsilon$ -eucryptite as a function of pressure calculated by DFT is shown. ....103   | 103 |
| Figure 5.4 | $\Delta G_{u.f.}$ as a function of pressure with the existence of $\Delta G_e$ , where $\Delta G_e$ includes the influence of dilational strain energy, shear strain and microcracking. The value of $\Delta G_e$ cannot be fully defined from the present study. $P$ represents the transformation pressure, and $P^*$ is the pressure at $\Delta G_{u.f.}=0$ . Hence, $\delta P=P-P^*$ , and $k\delta P$ represents the bulk free energy difference associated with the transformation. ....105  | 105 |

|            |   |     |
|------------|---|-----|
| Figure 5.6 | Experimental data shows the transformation pressure of each sample that expressed by both number of unit formula $N$ (left axis) and grain radius $r$ (right axis). The error bars are associated with the left axis. The red line is the fitting of S1, S2 and S3. ....  | 106 |
| Figure 6.1 | (a) Schematic drawing of polycrystalline $\beta$ -eucryptite, with one current pathway through the structure. The green arrows represent the direction of the $c$ -axis, whose orientation with respect to the pathway renders some grains fast (green, pathway approximately along the $c$ axis), and some grains slow (red, orientation not sufficiently aligned with the pathway). (b) Equivalent circuit to interpret complex impedance spectra: $R_{\parallel}$ , bulk resistance for conduction parallel to the $c$ axis; $R_{slow}$ and $CPE_{slow}$ , resistance and capacitance of the possible slow paths, including grain boundaries and unfavorably oriented grains; $CPE_{electrode}$ , capacitance of the electrode. The constant-phase element $CPE_{\parallel}$ is represented as dotted lines since, even when present, it cannot be detected from the experiments. .... | 113 |
| Figure 6.2 | (a) Impedance spectra of pure $\beta$ -eucryptite at selected temperatures from 300 to 900°C. (b, c) Impedance spectra and equivalent circuit at (b) 850 °C and (c) 350 °C. ....  | 116 |
| Figure 6.3 | Conductivity of total, along the $c$ -axis grains and slow paths as a function of temperature, respectively. ....   | 117 |
| Figure 6.4 | Experimental measured $\ln(R/T)$ as a function of $1/kT$ for total, paralleled grains and slow paths at low temperatures (solid symbols) combined with calculated values at high temperatures (open symbols). ....  | 119 |
| Figure 6.5 | Side view of the $\beta$ -eucryptite structures, with vertical channels in which Li motion can be correlated (a) or uncorrelated (b). Energy variation along the channels and the corresponding activation barrier for moving (a) three Li atoms at a time (correlated), and (b) one Li atom at a time (uncorrelated). ....   | 120 |
| Figure 9.1 | Raman spectra of pure $\beta$ -eucryptite as a function of pressure collected during compression. The onset of phase transformation is indicated by the bold line. ....   | 131 |
| Figure 9.2 | Transformation pressure of $\beta$ to $\varepsilon$ -eucryptite at different temperatures. ....   | 132 |

## LIST OF TABLES

|           |  |     |
|-----------|--|-----|
| Table 2.1 | Studies on grain size effects on pressure-induced phase transformations .....  | 100 |
| Table 2.2 | Li ionic conductivity of $\beta$ -eucryptite studied by various methods. ....  | 27  |
| Table 3.1 | Comparison of two types of diamond anvil cells .....   | 40  |
| Table 3.2 | Summery of useful optical pressure sensors for high temperature high pressure studies.....   | 44  |
| Table 3.3 | Commonly used pressure mediums and their conditions .....  | 50  |
| Table 3.4 | Atomic coordination of $\beta$ -eucryptite .....   | 64  |
| Table 4.1 | Lattice parameters and angles for the crystal structures shown in Figure 4.3 computed at zero pressure using GGA.....  | 83  |
| Table 6.1 | Activation energies of the total, bulk, and grain boundary in $\beta$ -eucryptite, determined from resistance measurements using Arrhenius's law. Above 440 °C, the activation energy is assumed to be 1.197 eV, hence no standard deviation is reported at these temperatures. .... | 119 |

## ACKNOWLEDGEMENTS

First and foremost I would like to give my sincerest thanks to my advisor, Dr. Ivar Reimanis. It is all my pleasure to have this opportunity to work and learn with you throughout this project that is funded by Department of Energy, Basic Energy Sciences, Grant Number DE-FG02-07ER46397. Thank you for supporting me with your patient and knowledge and encouraging me to work in my own way. I would also like to thank Dr. Cristian Ciobanu for providing many insightful discussions on data analysis and interpretation of phase transformations. Thank you to my other committee members: Dr. Brian Gorman, Dr. Corinne Packard. Thank you for all the support and encouragements that you provide throughout these years.

I cannot continue without thanking Dr. Zhongwu Wang, a scientist at Cornell High Energy Synchrotron Source (CHESS). You are a big part of my synchrotron radiation experience. You not only introduced me the key knowledge of operating the system, but also provided me helpful suggestions on experimental set up as much as I need. In addition, you helped me with gaskets drilling, which is completely out of your obligation.

I would like to thank Dr. John Chandler, Dr. Robert Filed and Gary Zito in the electron microscopy lab for training and assistance with the operation of scanning electron microscopes and x-ray diffractions.

Thank you, Dr. Subramanian Ramalingam and Dr. Badri Narayanan. Thank you for your excellent work in the early stage of this project, in both experiments and computational simulations. This research would not have been conducted without your contributions.

A big thanks to my peers in CCAC. You are all very talented and helpful, and I really appreciate the conversations, coffee runs and story sharing. I feel very fortunate to have you around during all these years. I also want to thank my research group members and office mates Amy Morrissey and Jaya Dorsey for your encouragements. You are still quiet supportive even after you left this office. I would also like to thank my qualify buddies, especially Aaron, Adom, San, Jiaojiao and Yujiang. I will always remember the precious time that we spent together on fighting for the qualify exam. Thank you, Zhifen and Teah, for the coffee runs and calls when either of us or both of us feel stressful. You are such a good friend to share feelings. There are too many more of you to name and I hope our paths cross in the future.

I've saved the best for my parents. Thank you for being understanding as I only visited back twice during these five years. You always respect my choices and encourage me to insist my decisions. Thank you for always listening to whatever I am talking about and being helpful with all the solutions.

Finally, I wish to thank my fiancé, Chuancheng Duan. I have heard many people said it is difficult to live with a PhD student, but I feel lucky that we are both PhD students, which makes life easier since we always understand each other. Thank you for your tremendous sacrifices and support, not only in life but also in scientific work. Thank you for making such good food for me and always taking care of me whether I am healthy or sick. Speaking of family members, I cannot ignore my lovely dog, Daisy. It seems strange to include a dog in acknowledgement, but I cannot finish it without thanking you. You always give me the most enthusiastic welcome back kisses and hugs when I get home. You help me to get rid of all the stresses by showing your most lovely smiles. You truly deserve a space in the acknowledgement.

## CHAPTER 1

### GENERAL INTRODUCTION

The interest of science and technology of ceramics has been spurred by the multifunctionality of their properties, not only in high temperature or inexpensive applications, but also varied contributions in optical, electronic, magnetic, thermal, chemical and structural components. This document focuses on the mechanical and electrical behavior of ceramics and in particular, pressure-induced phase transformation and ionic conductivity of  $\beta$ -eucryptite, a lithium aluminosilicate with unique thermo-mechanical-electrical properties.

The family of lithium aluminum silicates (LAS) is generally with the chemical composition of  $\text{Li}_{1-x}\text{Al}_{1-x}\text{Si}_{1+x}\text{O}_4$  ( $0 \leq x \leq 1$ ) [1], [2]. The widespread interest in LAS has been raised firstly due to their unique thermal behavior; they exhibit low, near zero and negative coefficient of thermal expansion (CTE) over wide temperature range and, in turn, are suitable for thermal shock resistant applications, such as heat exchangers and stove cook tops [1], [3]. The most important crystalline phase in the LAS system is  $\beta$ -eucryptite with a chemical composition of  $\text{LiAlSiO}_4$  and a hexagonal crystal structure. It not only exhibits a highly anisotropic CTE, but also well known for its one-dimensional superionic conductivity of Li ions along the crystallographic c-direction [4]–[8], structural phase transitions under pressure [9]–[16]. This makes  $\beta$ -eucryptite a good candidate for applications in lithium ion batteries and transformation-toughening ceramics.

From a fundamental point of view, a study of a material with such unusual properties offers an opportunity to better understand structure-property relationships and design novel composites with tailored properties. In this study, the crystal structure of high pressure  $\epsilon$ -



eucryptite has been solved through a combination of x-ray diffraction and density functional theory, which has been questioned for many years. We also develop the effect of grain size on pressure-induced phase transformation. Li order-disorder transition in polycrystalline  $\beta$ -eucryptite including the grain boundary effect is studied by electrochemical impedance spectroscopy.

## 1.1 Motivation

The present study was motivated by the desire to understand the structure-property relationships in  $\beta$ -eucryptite, a member in lithium-aluminum-silicate family that shows interesting properties due to its unique structure.  $\beta$ -eucryptite has been observed to have different structural changes under pressure and/or temperature. The details of the structure-property relations remain largely unexplored. In addition,  $\beta$ -eucryptite can be considered as a typical structure of those materials formed by corner sharing tetrahedra with open space. Thus, study the structural and property relationship of  $\beta$ -eucryptite is very useful for understanding other materials with similar structure or properties.

The first desire of the present study is to understand the detail about the phase transformation in  $\beta$ -eucryptite, specifically, the reverse transformation between  $\beta$ -eucryptite and  $\epsilon$ -eucryptite. Transformation toughening is recognized as one the most important ceramic toughening mechanisms, and has been well developed in  $ZrO_2$  and  $ZrO_2$  based composites [17].  $\epsilon$ -eucryptite has been confirmed to have smaller volume than  $\beta$ -eucryptite, thus, the volume expansion associated with  $\epsilon$  to  $\beta$ -eucryptite transformation makes it has a great potential to perform as a transformation toughener. Though the concept of using  $\epsilon$ -eucryptite as transformation toughener has been proposed in earlier studies [17], [18], the details of  $\epsilon$  structure still remain largely unexplored. The aim of this study is first to have a deeper understand the  $\epsilon$ -

eucryptite from a crystallography point of view. Though the pressure-induced phase transformations in  $\beta$ -eucryptite have been observed by several groups, no metastability of the high pressure phase to ambient conditions was observed [12]–[14], [19]. Thus, it is very important to find out how to stabilize the  $\varepsilon$ -eucryptite to make it more applicable as a transformation toughening material. In many ceramics, metastability is achieved via the addition of stabilizing dopants or by the modification of grain size [20]–[23]. The present project studies the relation between phase transformation pressures as a function of grain sizes.

$\beta$ -eucryptite not only exhibits structural transformation at high pressure, it also undergoes an order-disorder transition under high temperature. The order-disorder transition is believed to be caused by Li ions positional change in the channel of c axis. However, the Li motion in ordered and disordered structures has not been confirmed, and the mechanism by which the order-disorder transition occurs has not been developed. The present study aims to understand how the crystal structure of  $\beta$ -eucryptite, and in particular, the positional transitions of Li, influence the ionic conductivity at various temperatures.

## **1.2 Thesis organization**

This thesis is organized in the following chapters:

1. CHAPTER 1 presents the general information about the material and the motivation to study this material.
2. CHAPTER 2 provides an overview of existing literature that studied  $\beta$ -eucryptite through different techniques. Interesting properties that  $\beta$ -eucryptite exhibit are talked in details, individually.

3. CHAPTER 3 introduces all experimental procedures in the present study, including synthesis  $\beta$ -eucryptite powders and pellets, diamond anvil cell setup and calibrations, high energy x-ray diffraction, Raman spectroscopy and electrochemical impedance spectroscopy.
4. CHAPTER 4 presents a paper published in Scripta Materialia, titled “Pressure-induced phase transformation in  $\beta$ -eucryptite: An X-ray diffraction and density functional theory study”.

Author list: Yachao Chen<sup>1</sup>, Sukriti Manna<sup>2</sup>, Badri Narayanan<sup>2</sup>, Zhongwu Wang<sup>3</sup>, Ivar E. Reimanis<sup>1,\*</sup>, Cristian V. Ciobanu<sup>2,\*</sup>

<sup>1</sup> Department of Metallurgical and Materials Engineering, Colorado School of Mines, Golden, CO 80401, USA. Y. Chen performed the fabrication and high pressure experiments of  $\beta$ -eucryptite samples. S. Manna performed the DFT modeling and Rietveld Refinement analysis. B. Narayanan provided the entropy analysis on different phases.

<sup>2</sup> Department of Mechanical Engineering, Colorado School of Mines, Golden, CO 80401, USA

<sup>3</sup> Cornell High Energy Synchrotron Source, Cornell University, Ithaca, NY 14853, USA. Z. Wang provided supervisory guide on experimental setup at CHESS.

\* C. Ciobanu and I. Reimanis are authors for correspondence.

In this chapter, we answer a long-standing question about the crystal structure of pressure stabilized  $\varepsilon$ -eucryptite by combining x-ray diffraction experiments with density functional theory (DFT).

5. CHAPTER 5 presents the paper titled “*In-situ* diamond anvil cell-X-ray diffraction study on grain size effects of phase transformation from  $\beta$ - $\epsilon$  eucryptite”, submitted to Journal of American Ceramic Society.

Author list: Yachao Chen<sup>1</sup>, Sukriti Manna<sup>2</sup>, Cristian V. Ciobanu<sup>2</sup> and Ivar E. Reimanis<sup>1</sup>

<sup>1</sup> Department of Metallurgical and Materials Engineering, Colorado School of Mines, Golden, CO 80401, USA. Y. Chen worked on sample fabrication, EIS experiments and EIS analysis.

<sup>2</sup> Department of Mechanical Engineering, Colorado School of Mines, Golden, CO 80401, USA. S. Manna and C. Ciobanu provided the calculations on activation barriers of different Li motions.

We observed a decrease transformation pressure with increase of grain size, which indicates that the high pressure  $\epsilon$ -eucryptite can be stabilized by increasing the grain size. The transformation pressure we measured for grain size around 1  $\mu\text{m}$  is about 0.5 GPa, which makes it more applicable to be used as transformation toughener.

6. CHAPTER 6 presents the paper titled “Thermal regimes of Li-ion conductivity in  $\beta$ -eucryptite”. Here we bring out a method to solve for grain bulk conductivity separate from the influence of grain boundary conductivity in polycrystalline materials by applying a brick layer model and assuming the grain boundary characters. We also interpret the order-disorder transition with Li correlated motion and uncorrelated motion.

7. CHAPTER 7 provides a general discussion to tie together the body of work presented in this thesis and points out the contributions to the field.

8. CHAPTER 8 presents conclusions that obtained from this study.
9. CHAPTER 9 gives suggestions for future work.

## CHAPTER 2

### LITERATURE REVIEW

$\beta$ -eucryptite has been studied since the late 1940s. Many interesting behaviors of  $\beta$ -eucryptite have been investigated. This chapter provides a detailed literature review, including the materials background, thermal properties, mechanical properties and electrical properties, respectively.

#### 2.1 Materials Overview

The structure of  $\beta$ -eucryptite, which has been investigated by Winkler [24], Buerger [25], Hornyak [26], Tscherry et al. [27], [28], and Pillars and Peacor [9], is described as a stuffed derivative of  $\beta$ -quartz with space group  $P6_422$  or  $P6_222$ . At room temperature,  $\beta$ -eucryptite contains 84 atoms in a unit cell [25], [27]–[30]. The crystal structure viewed from different directions is shown in Figure 2.1 The radii of  $Al^{3+}$  and  $Si^{4+}$  in four-coordination are 0.39 and 0.26 Å, respectively [31], [32].  $[SiO_4]^{4-}$  and  $[AlO_4]^{5-}$  tetrahedra are arranged in a spiral along the  $6_4$  (or  $6_2$ ) screw axis parallel to the c-axis, leading to open channels along the c-axis where  $Li^+$  resides to balance the charge [9], [24], [25], [30], [33]. In fully ordered  $\beta$ -eucryptite,  $AlO_4$  and  $SiO_4$  are segregated into alternating tetrahedral sheets parallel to the c axis.  $AlO_4$  tetrahedra tend to connect via corner sharing with  $SiO_4$  tetrahedra as the nearest neighbours, rather than other  $AlO_4$  tetrahedra. In other words, the “Al-avoidance” principle is applicable in ordered  $\beta$ -eucryptite, that Al-O-Si linkages are energetically favored over either Al-O-Al or Si-O-Si [34], [35]. This principle dictates that only Al-O-Si linkages occur in  $\beta$ -eucryptite structure, since  $Si/Al=1$ . As a result, the lattice parameter of c axis of  $\beta$ -eucryptite is doubled ( $a=b=10.497$  Å,  $c=11.20$  Å at room temperature) relative to that of prototype  $\beta$ -quartz ( $SiO_2$ ) [9], [30], [36], [37]. There are two types of channels (primary and secondary) for Li, with six available tetrahedral

sites in each channel [38]. There is one primary channel (A) and three secondary channels (S), and Li atoms only occupy three of the available sites in an alternating sequence with vacancy sites in these channels. Since Al is larger than Si, the Al-tetrahedral sheets are larger than the Si-tetrahedral sheets. Thus, stuffing Li ions into the channels within the Si tetrahedra layers enlarges the Si tetrahedra sheets and reduces the dimensional mismatch of Si tetrahedra sheets with Al tetrahedra sheets [32]. Therefore, in ordered  $\beta$ -eucryptite, 25% of the Li ions are coplanar with Al tetrahedral sheets, while the other 75% of the Li ions are coplanar with Si tetrahedral sheets [32], [39].

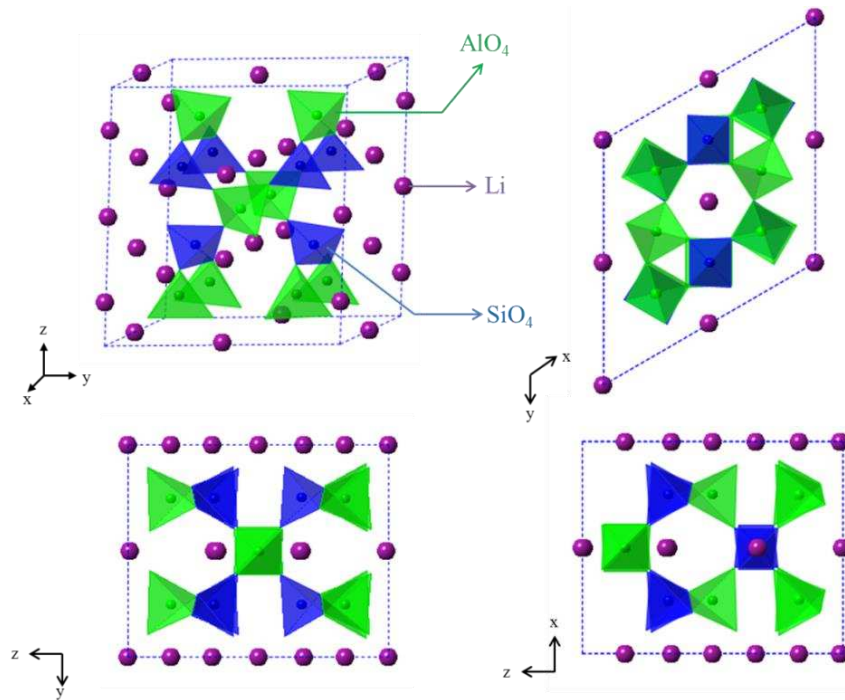


Figure 2.1 Crystal structure of  $\beta$ -eucryptite viewing from different directions. The blue and green tetrahedra represent  $\text{SiO}_4$  and  $\text{AlO}_4$ , respectively. Purple balls represent Li ions.

## 2.2 Negative coefficient of thermal expansion

The crystal structure of  $\beta$ -eucryptite is highly anisotropic, manifesting itself as high thermal expansion anisotropy, high anisotropic compressibility, and one-dimensional Li ion conductivity [4], [15], [24], [29], [32], [40]. The highly anisotropic structure also results in an overall negative coefficient of thermal expansion (CTE). Gillery and Bush were the first that measured the intrinsic CTE ( $\alpha$ ) that is  $\alpha_a=\alpha_b=8.21\times 10^{-6}$  /°C perpendicular to the c axis,  $\alpha_c=-17.6\times 10^{-6}$  /°C parallel to the c axis between room temperature and 800 °C, resulting in an average CTE of  $-0.39 \times 10^{-6}$  /°C in a bulk specimen [41], [42]. This anomalous behavior occurs due to a rigid rotational tilting of the framework tetrahedral, which leads to an expansion in the (001) plane and a contraction along the c-axis with increasing temperature [32]. One of the most obvious uses of negative thermal expansion is in composite materials where the overall CTE can be tailored to a specific value (slightly positive, negative or even near zero) [43]. Controlled expansion composites are likely to be involved where the CTE of certain material needs to be modified to zero or near-zero such as in fiber optic systems, thermal shock resistant applications and also electronic or biomedical applications [29], [32], [40], [44]–[48]. The anisotropic thermal expansion of  $\beta$ -eucryptite leads to large thermal residual stresses in polycrystals which cause spontaneous microcracking [42]. Pelletant *et al.* [49] have studied grain size dependence on the CTE of pure  $\beta$ -eucryptite and found that larger grain sizes promote microcracking, leading to a significant decrease of average CTE of polycrystalline  $\beta$ -eucryptite. Thus, microcracking dominates the negative CTE for large grain size  $\beta$ -eucryptite pellets. The critical grain size above which spontaneous microcracking occurs is 2.8  $\mu\text{m}$ . Ramalingam *et al.* [42] observed that when  $\beta$ -eucryptite is doped with small amounts of Zn (as low as 0.1 mol%), the CTE increases significantly (Figure 2.2). The hysteresis in these plots is indicative of cyclic microcracking.



Hysteresis decreases dramatically in  $\text{Zn}^+$  doped  $\beta$ -eucryptite, indicating the tendency of microcracking decreases greatly compared with pure  $\beta$ -eucryptite (Figure 2.2) [42]. Mg doped  $\beta$ -eucryptite has been shown to have a similar results in the present study (Figure 2.3) [50]. Thus, it is proposed that certain small cations (such as  $\text{Zn}^{2+}$  and  $\text{Mg}^{2+}$ ) may lead to dramatic changes in thermophysical properties of  $\beta$ -eucryptite.

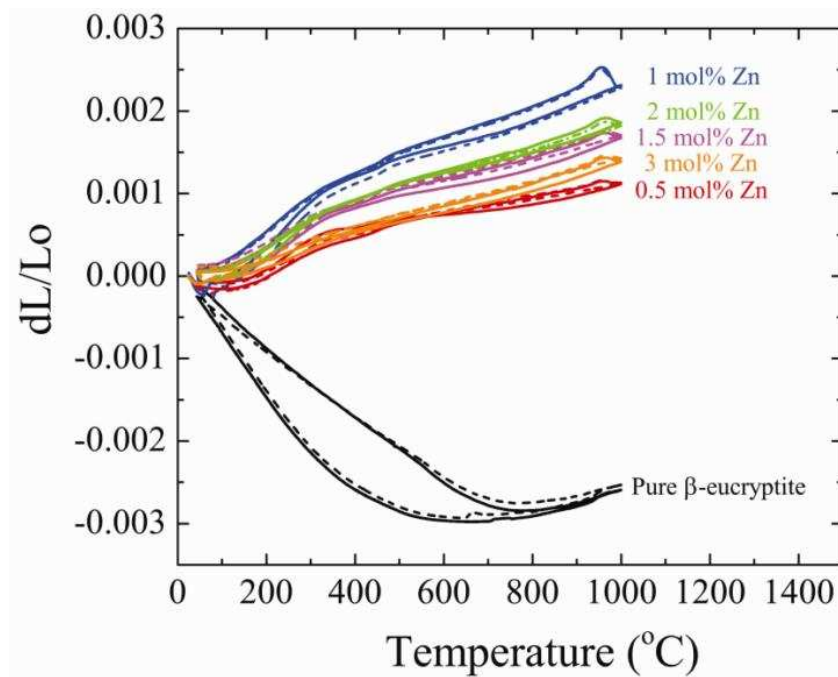


Figure 2.2 The thermal expansion behavior of pure and Zn doped  $\beta$ -eucryptite from room temperature and 1000 °C. Zn concentrations are from 0.5 mol% to 3 mol%.

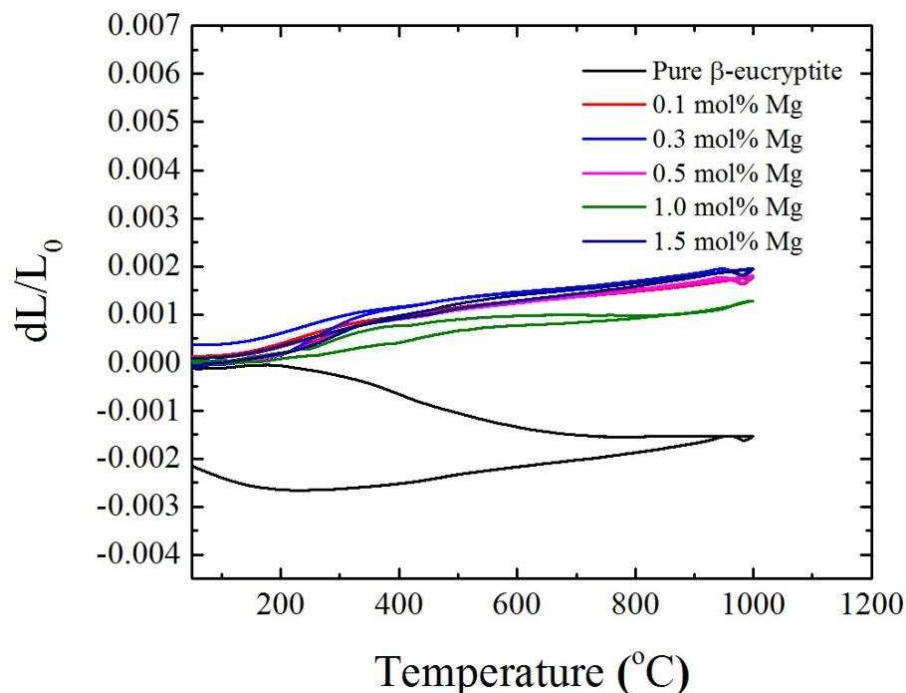


Figure 2.3 The thermal expansion behavior of pure and Zn doped  $\beta$ -eucryptite from room temperature and 1000 °C. Zn concentrations are from 0.5 mol% to 3 mol% [50].

Mg occupancy in aluminosilicates have been investigated using synchrotron X-ray diffraction (XRD), transmission electron microscopy (TEM), and  $^{29}\text{Si}$  nuclear magnetic resonance (NMR) spectroscopy to study  $\text{Mg}_{0.5}\text{AlSiO}_4$  that was grown from a glass [34]. The difference electron Fourier (DELFO) and Rietveld refinement showed that, instead of occupying the tetrahedral channel as Li in  $\beta$ -eucryptite, Mg ions end up with an octahedral coordination and are disordered over all the available sites along the channels [34], [51], [52]. Octahedral channel  $\text{Mg}^{2+}$  results in a higher degree of deformation of neighboring  $[\text{Si}/\text{AlO}_4]$  framework than tetrahedral  $\text{Li}^+$ . This distortion transforms the structure from  $\beta$ - to  $\alpha$ -quartz-like in  $\text{Mg}_{0.5}\text{AlSiO}_4$  and results in a positive thermal expansion in  $\text{Mg}_{0.5-0.5x}\text{Al}_{1-x}\text{Si}_{1+x}\text{O}_4$  [53]–[55]. The coordination environments of  $\text{Li}^+$  in the  $\beta$ -quartz framework of  $\text{LiAlSiO}_4$  and  $\text{Mg}^{2+}$  in the  $\alpha$ -quartz framework of  $\text{Mg}_{0.5}\text{AlSiO}_4$  are shown in Figure 2.4. This also explains the fact that small amounts of cation

dopants lead to a dramatic change in thermophysical properties of  $\text{LiAlSiO}_4$  from a crystallography point of view.

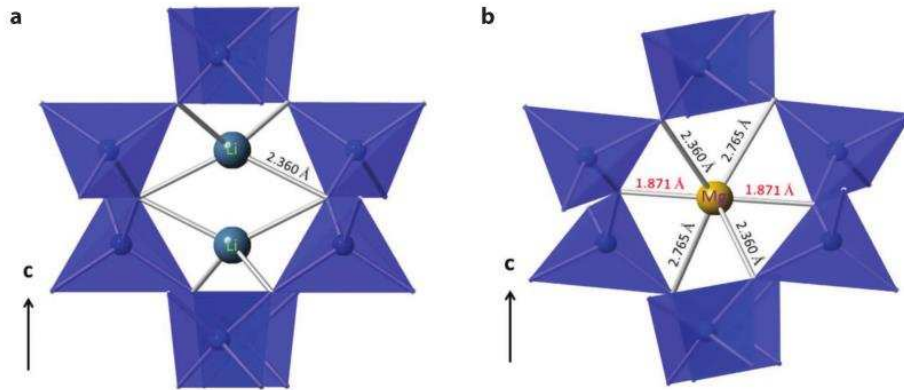


Figure 2.4 Coordination environments of (a) channel  $\text{Li}^+$  in the  $\beta$ -quartz framework of  $\text{LiAlSiO}_4$  and (b)  $\text{Mg}^{2+}$  in the  $\alpha$ -quartz framework of  $\text{Mg}_{0.5}\text{AlSiO}_4$ . Tetrahedra represent  $[\text{Si}/\text{AlO}_4]$  units, and spheres represent  $\text{Li}^+$  or  $\text{Mg}^{2+}$  [34].

### 2.3 Pressure-induced phase transformation

Like other open crystal structures with low or negative CTE's, the  $\beta$ -eucryptite structure also collapses under sufficiently high hydrostatic pressures, resulting in phase transformation and/or amorphization in the material [9]–[11]. Literature has shown various phase transformations under pressure and temperature (Figure 2.5). A reversible phase transformation to  $\varepsilon$ -eucryptite occurs at 1 GPa. Pressure greater than 1 GPa at  $600^\circ\text{C}$  results in an irreversible transformation from  $\beta$  to  $\alpha$ -eucryptite, a thermodynamically stable phase of eucryptite [10], [12], [13], [15], [32]. At pressures greater than 5 GPa,  $\varepsilon$ -eucryptite begins to amorphize and over 17 GPa, it is completely amorphous. When the pressure is released before it reaches 17 GPa,  $\beta$ -eucryptite recrystallizes, indicating the presence of structural memory in the material [13].

Above 17 GPa, it remains amorphous upon decompression. Zhang, et al. [12], [13] reported the crystal structure of  $\epsilon$ -eucryptite as orthorhombic and provided the lattice parameters using *in-situ* high energy x-ray diffraction. From their study, it is found that the  $\epsilon$ -eucryptite has a lattice volume 7.7% lower than that of  $\beta$ -eucryptite [56], [57]. The increase in volume associated with reverse  $\epsilon$  to  $\beta$ -eucryptite transformation at moderate pressure ( $\sim 1$  GPa) is believed to have a potential application in synthesizing transformation toughened composites based on  $\beta$ -eucryptite [17]. In addition to this technological significance, the reversible phase transition between  $\beta$  and  $\epsilon$  provides a plausible explanation for a very interesting phenomenon observed by Reimanis and co-workers [56]: spontaneous ejection upon indenting composites of  $\beta$ -eucryptite and lithium aluminate ( $\text{LiAl}_5\text{O}_8$ ) with particle sizes ranging from sub-micrometer to tens of micrometer. However, the detail including space group and atomic structure of the  $\epsilon$ -eucryptite remains unknown.

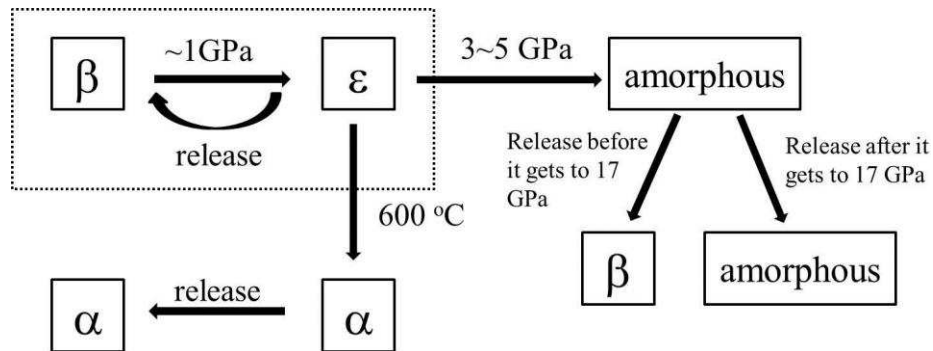


Figure 2.5 Schematic showing the various phase transformation in  $\beta$ -eucryptite

Ramalingam, et al. [16] applied the nanoindentation technique on both polycrystalline and single crystal  $\beta$ -eucryptite. Through examining the rate dependence of the strengths using

maximum shear stress analysis [58], [59] and analyzing the cumulative statistics of the Hertzian deviation loads [60]–[63], the activation volume of phase transformation from  $\beta$  to  $\varepsilon$ -eucryptite was determined to be roughly around  $0.1 \text{ nm}^3$ . A single unit cell of  $\beta$ -eucryptite contains 84 atoms [64] and is arranged in about 12 tetrahedra with a volume of  $1.07 \text{ nm}^3$  [12], [13]. Thus, the process that is responsible for the phase transformation is on the order of the size of the  $[\text{SiO}_4]$  and  $[\text{AlO}_4]$  tetrahedra. The presence of structural memory in the material has been discussed in terms of non-deformable units within the structure that act as templates upon which the original structure can be recovered. The  $[\text{SiO}_4]$  tetrahedra are more rigid than the  $[\text{AlO}_4]$  tetrahedra [13] in both  $\beta$  and  $\varepsilon$ -eucryptite; therefore, the  $[\text{AlO}_4]$  tetrahedra become gradually distorted under compression while the  $[\text{SiO}_4]$  tetrahedra rotate but remain intact. Upon decompression, the nondeformable  $[\text{SiO}_4]$  units act as templates to direct the transformed structure back to the original state [13]. The presence of Li ions along the  $c$  channels also likely to play a role in relaxation, since it is energetically favorable to expand the structure. However, when the pressure exceeds the threshold (17 GPa),  $[\text{SiO}_4]$  tetrahedra start to deform as well, resulting in the disappearance of the structural memory [13]. Although Zhang *et al.* [12] looked at both  $\varepsilon$ -eucryptite and  $\alpha$ -eucryptite under high pressure and temperature through x-ray diffraction and indicated that  $\varepsilon$ -eucryptite adopts an orthorhombic crystal structure, there are some inconsistencies with their determination of the space group and atomic positions of  $\varepsilon$ -eucryptite. Figure 2.6 shows the hierarchy of seven crystal systems, and phase transformation generally proceeds from high symmetry to low symmetry [65].

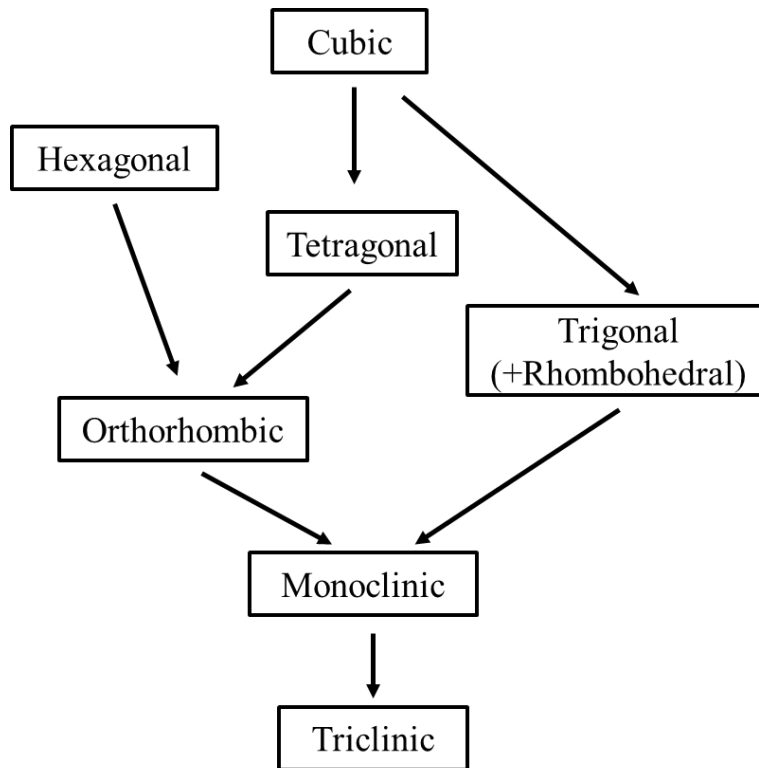


Figure 2.6 Hierarchy of seven crystal systems

## 2.4 Grain size effect on pressure-induced phase transformation

### 2.4.1 Diffusional vs. diffusionless phase transformation

The majority of phase transformations that occur in the solid state take place by thermally activated atomic movements, which require diffusion of atoms in order to form new phase(s). The overall transformation kinetics follows the TTT diagrams. On the other hand, a diffusionless transformation occurs without the long-range diffusion of atoms. This is typically referred to as a martensitic transformation. Martensitic phase transformations are widely used for hardening steel by quenching rapidly enough from the austenitic field. Because of the insufficient time for eutectoidal diffusion-controlled decomposition processes to occur and the presence of carbon interstitially in the face center cubic (fcc) austenitic structure, austenite transforms to martensite.

Martensitic transformation is a term used in physical metallurgy to describe any diffusionless transformation in which individual atomic movements are less than one interatomic spacing from start to completion of the transformation. Martensitic transformations can occur in many types of metallic and nonmetallic crystals, minerals, and compounds [66].

#### 2.4.2 Nucleation model

The nucleation event plays an important role in both diffusional and diffusionless phase transformations. In high pressure studies, the barrier to transition is usually explained in terms of nucleation dynamics. The general nucleation model is expressed as [66]–[68]:

$$\Delta G = V\Delta G_V + A\gamma = \frac{4}{3}\pi r^3 \Delta G_V + 4\pi r^2 \gamma \quad (2.1)$$

where  $\Delta G$  is the total free energy change associated with the transformation;  $\Delta G_V$  is free energy per unit volume released upon creating the new phase particles;  $\gamma$  is the interfacial free energy per unit area upon creating new interfaces associated with the transformation;  $V$  is the volume of the nucleus;  $A$  is the interfacial area;  $r$  is the nucleus radius. Thus, a schematic showing  $\Delta G$  as a function of  $r$  is shown in Figure 2.7.

In order for a phase transformation to occur,  $\Delta G_V$  in (2.1) must be negative, and the interfacial energy term is always positive, since energy is increased in making an interface.[67] It is seen that because of the positive term,  $\Delta G$  possesses a maximum before it becomes negative. For successful nucleation, small clusters must form and then grow to larger size by decreasing the free energy. In other words, the critical nuclei form when the free energy is at a maximum. Thus, critical nucleus size ( $r^*$ ) represents the minimum viable nucleus size. If nuclei are formed with  $r < r^*$ , it is energetically favorable to spontaneously decompose back to the parent phase. However, if nuclei are formed with  $r > r^*$ , it is energetically favorable for the nuclei to keep

growing. The free energy at maximum is referred to as the “critical free energy”. The values of critical nucleus size ( $r^*$ ) and critical free energy ( $\Delta G^*$ ) can be found from the condition:

$$\frac{\partial \Delta G}{\partial r} = 0 \quad (2.2)$$

Thus, for the case where  $\gamma$  is isotropic,  $r^*$  and  $\Delta G^*$  are given by:

$$r^* = -\frac{2\gamma}{\Delta G_V} \quad (2.3)$$

$$\Delta G^* = \frac{4}{3}\pi(r^*)^3 \Delta G_V + 4\pi(r^*)^2 \gamma = \frac{16\pi^2 \gamma^3}{3(\Delta G_V)^2} \quad (2.4)$$

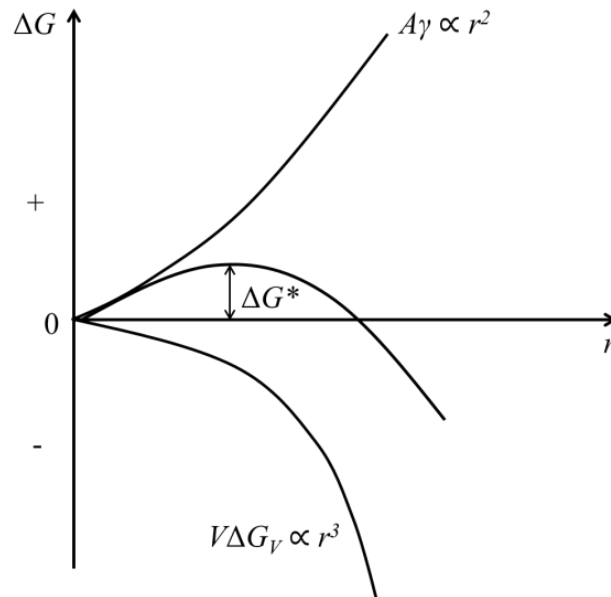


Figure 2.7 Variation of  $\Delta G$  with  $r$  for a homogeneous nucleus.  $\Delta G^*$  represents the activation energy barrier.



Misfit stresses may also contribute to  $\Delta G_v$ . They generally arise in association with a shape change. Eshelby [76] showed that there is an elegant solution to this problem and approached it by visualizing a series of cutting, straining and welding operations illustrated in Figure 2.8. The processes to determine the misfit stresses may be described with the following steps.

- A region (inclusion) is first cut from the unstressed elastically homogeneous material, and is then imagined to undergo a shape change, resulting in a transformation strain  $\epsilon^T$  free from the constraining matrix.
- The inclusion has changed shape and thus cannot be replaced directly back into the cavity in the matrix from whence it came. In order to put the inclusion back to its original place, surface tractions are applied on the inclusion to return it to its original shape. At this point, zero stress is in the matrix, but there is stress on inclusion because of the applied surface tractions.
- Apply equal and opposite force at the interface between the matrix and the inclusion to remove the surface tractions. Equilibrium is then reached between the matrix and the inclusion at a constrained strain ( $\epsilon^C$ ) of the inclusion.
- The stresses in the matrix only result from the constrained strain ( $\epsilon^C$ ), whereas, the stresses in the inclusion result from both transformation and constrained strains ( $\epsilon^C - \epsilon^T$ ).

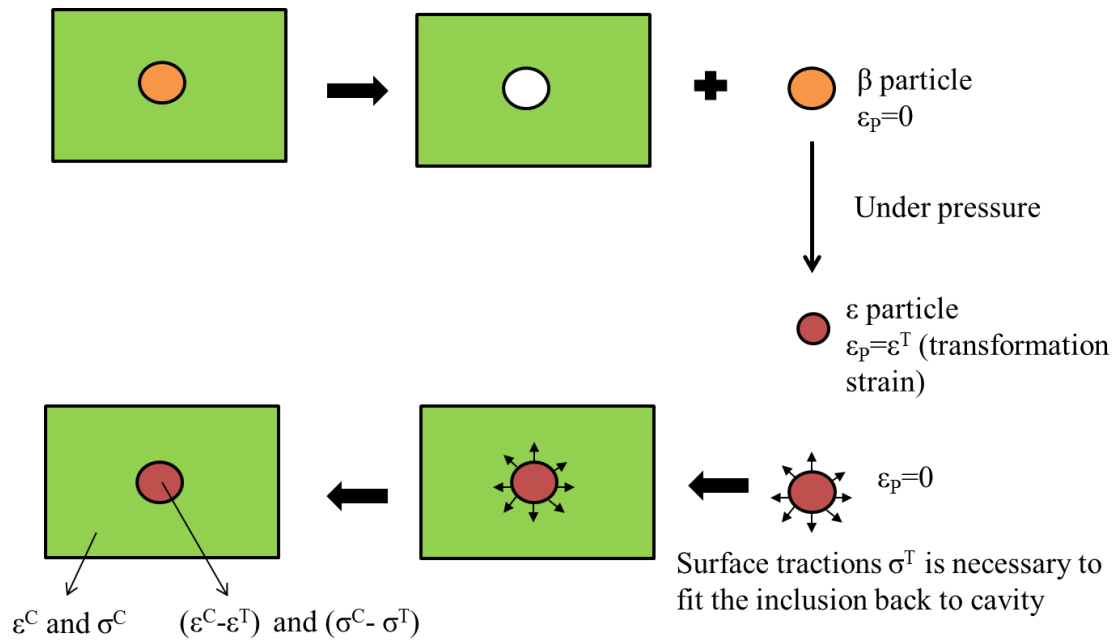


Figure 2.8 Schematic showing that the strain and stress on matrix and particles after transformation.

### 2.4.3 Transformation toughening

Among different toughening mechanisms (e.g. crack deflecting, fiber bridging toughening, pull out toughening, *et.al*), transformation toughening is recognized as one of the most potent. For example, in  $ZrO_2$  system, toughness contributions from microcrack and deflection mechanisms are 2-6 and 2-4  $MPa \cdot m^{1/2}$ , respectively [77], [78]. These are considerably smaller compare with that of transformation toughening, which may be as high as 15  $MPa \cdot m^{1/2}$  [79]. Particles which undergo a stress-induced martensitic transformation are known to toughen certain brittle materials [80]–[86].  $ZrO_2$  and  $ZrO_2$  reinforced composites are the most widely studied in transformation toughening [20], [87]–[94]. The mechanism of transformation toughening is illustrated in Figure 2.9, taking  $ZrO_2$  (tetragonal to monoclinic phase transformation) as an example. The enhanced toughness can be considered to generate from the

volume expansion that is associated with the transformation from a metastable phase to a stable phase due to the crack-tip stress field, thereby limiting the crack opening [20], [92], [95], [96]. Transformation toughening of  $ZrO_2$  was first reported by Garvie *et al.* in Nature [80]. A martensitic phase transformation of  $ZrO_2$  from tetragonal (*t*-) to monoclinic (*m*-) can be triggered by the crack tip stress field and a volumetric expansion is associated with the transformation, which gives the principle contribution to toughening in these ceramics. It is widely accepted that for the transformation toughener, the reinforcing phase must (a) exhibit a martensitic phase transformation (diffusionless) that can be induced by stress field, (b) exist in a metastable state, and (c) have a dilatational strain associated with the transformation.

Retention of the tetragonal  $ZrO_2$  during cooling from high to ambient temperature is the most important factor for the utilization of transformation toughening. For zirconia, the transformation barrier may be overcome by either thermal activation or stress (strain). Heuer *et al.* studied the stability of *t*- $ZrO_2$  in both  $Al_2O_3$  and cubic  $ZrO_2$  matrices by considering how the thermodynamics of the *t-m* transformation is effected by surface and strain energy effects, nucleation considerations, etc [21]. The transformation state of *t-m* transformation can be visualized with the free energy diagram as shown in Figure 2.10. The total free energy released on transformation is  $\Delta G_V$ , where  $G_V$  is the free energy per unit volume of a crystal.  $\Delta G^*$  represents the nucleation barrier that must be overcome for transformation to occur. It is the activation energy.

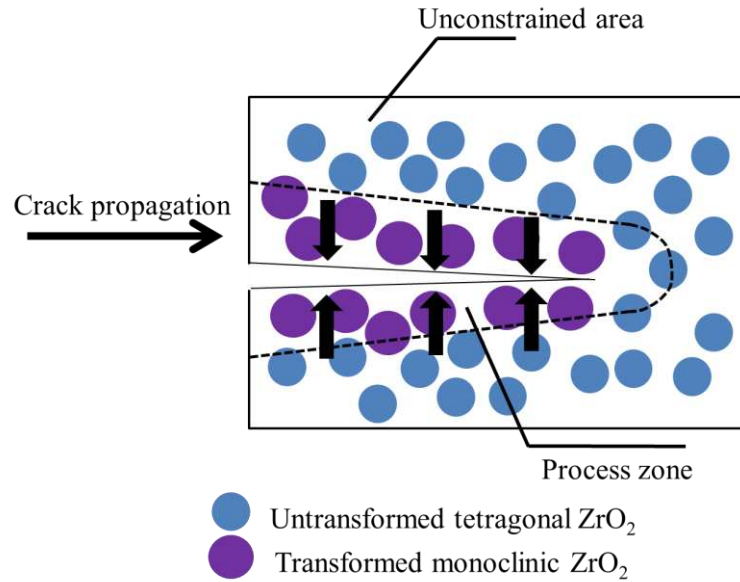


Figure 2.9 Schematic describes transformation toughening mechanism using  $ZrO_2$  as an example. In a tetragonal zirconia dispersed ceramic matrix, the stress field advancing ahead of a propagating crack transforms the small tetragonal particles to larger monoclinic particles. The larger transformed monoclinic particles apply a crack-closing force in the process zone, effectively resisting the crack propagation.

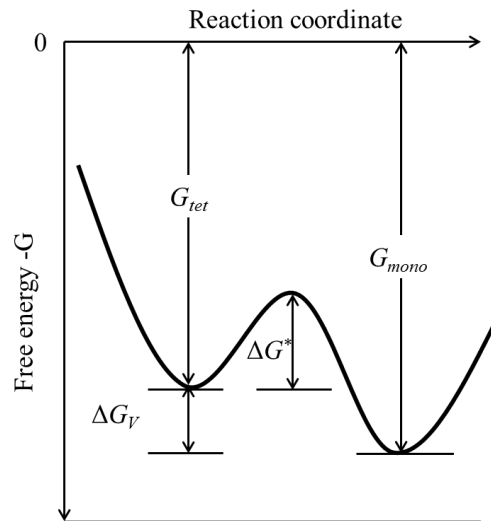


Figure 2.10 Reaction coordinate diagram showing energetics of  $t-m$  transformation. The reaction coordinate is any variable defining the reaction path such as pressure.

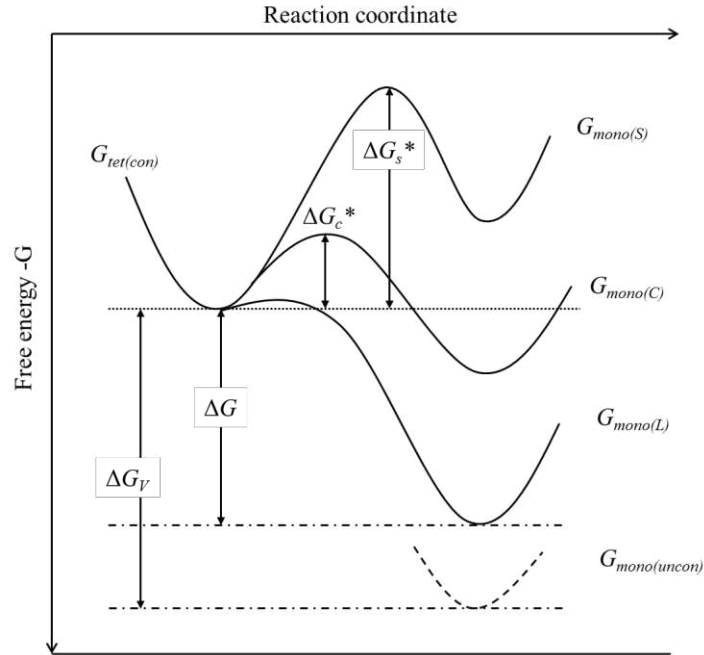


Figure 2.11 Schematic representation of the various free energy forms associated with the tetragonal to monoclinic transformation with different initial particle sizes: S, small; C, critical; L, large, and uncon, unconstrained [77].

In the case of particles constrained in a solid matrix, the ease with which the tetragonal to monoclinic transformation can occur in zirconia will depend upon a number of physical and chemical factors, especially the particle size [82], [85], [97] and the matrix in which the particles are being constrained. The various energetic states of the tetragonal and monoclinic phases are shown in Figure 2.11. It is aim to use fabrication treatment to produce *t*-ZrO<sub>2</sub> with the transformation temperature at or near room temperature, so that the transformation toughening works at room temperature. When the particle is a critical size, the transformation temperature is just below room temperature. In this situation,  $\Delta G^*$  becomes very small and can be overcome as a result of an applied stress. When the particle is smaller than the critical size, it requires sufficient undercooling. In addition, in this situation, the free energy of the constrained particle is

higher than that of the tetragonal phase, which leads no net driving force for the transformation. The activation barrier for nucleation is also quite large and virtually insurmountable. On the other hand, for a large particle, whose transformation temperature is above room temperature, will transform upon cooling naturally. Linear temperature dependence of reciprocal radius for the tetragonal-monoclinic transformation in Ca-PSZ, Al<sub>2</sub>O<sub>3</sub>, and Mullite-ZrO<sub>2</sub> has been shown by Garvie and Swain by considering surface and strain energy terms [22], [98], [99]. The stability of the tetragonal phase can also be enhanced by the addition of high-solubility dopants, such as Y<sub>2</sub>O<sub>3</sub> or CeO<sub>2</sub>, or by the addition of low solubility divalent stabilizing oxides, such as MgO and CaO by taking the surface energy and matrix constraint into consideration [20]–[23], [77], [100]. Thus, it is the aim of processing and fabrication to provide an optimized microstructure comprising metastable tetragonal particles that cooperate in the transformation-toughening process. Although ZrO<sub>2</sub> has been successfully employed as transformation toughener, there are many other ceramics that exhibit martensitic phase transformation but are largely unexplored [101]–[103].

$\beta$ -eucryptite has been recognized as a transformation toughening material due to its reversible phase transformation to the denser  $\epsilon$ -eucryptite at moderate pressure (~1 GPa). Clearly, control over the metastability of  $\epsilon$ -eucryptite in order to design a transformation toughened composite. Doping  $\beta$ -eucryptite with Mg or Zn tends to stabilize  $\beta$ -eucryptite according to Raman spectroscopy and x-ray diffraction studies [19], [104]. In other words, the pressure required to transform  $\beta$ -eucryptite to  $\epsilon$ -eucryptite increases. Thus, doping  $\beta$ -eucryptite with small ions does not work on the right direction to stabilize the  $\epsilon$ -eucryptite. It was hypothesized that residual thermal stresses arising due to the mismatch in CTE between the matrix and the particulate may be utilized to induce the stresses necessary to stabilize the high pressure phase

[17]. The stresses caused by thermal mismatch on  $\beta$ -eucryptite particle from matrix such as MgO, 10YSZ,  $\text{Al}_2\text{O}_3$ , etc., have been calculated from the steps described above [17]. 10YSZ has been shown to act as the best candidate to provide enough stress to stabilize  $\varepsilon$ -eucryptite particles. Though no evidence of the high pressure  $\varepsilon$ -eucryptite was found, the toughness of 10YSZ changes with volume fraction of  $\beta$ -eucryptite, indicating a transformation toughening model should be considered in conjunction with the toughening decrement predicted due to matrix tensile stresses which arise due to the thermal expansion mismatch. Thus, grain size effects are worthwhile to be investigated.

## 2.5 Li ionic conductivity-order-disorder transition

Generally, ionic conductors can be classified into three categories based on the ion conductors' mobile dimensions (1D, 2D or 3D). For instance,  $\text{Li}_3\text{N}$  is reported to be a three dimensional (3D) conductor [105];  $\text{Na-}\beta\text{-Al}_2\text{O}_3$  is a good example for 2D conducting as the  $\text{Na}^+$  ions moving in planes (2D) [106]. Several materials such as  $\text{Li}_2\text{Ti}_3\text{O}_7$  [107] and  $\text{LiFePO}_4$  are known to exhibit a pronounced one dimensional conductance (1D) along structural channels. The dimensionality and topology of the compounds is found to play an important role in the diffusion of Li ions [108], [109]. Similarly,  $\beta$ -eucryptite exhibits one-dimensional super-ionic conductivity as well as the anisotropic thermal expansion behavior that was described in 2.2. Li ionic conductivity along the  $c$  axis is nearly three decades of that within the  $a$ - $b$  plane in the temperature range from 200 °C to 600 °C [4], [29], [110]. Renker *et al.* [7] showed a  $\text{Li}^+$  diffusion along the hexagonal  $c$ -direction and the  $\text{Li}^+$  jump distance of  $c/3$ , where  $c$  is the lattice constant of  $c$ -axis of  $\beta$ -eucryptite ( $c=11.19 \text{ \AA}$ ), through quasi-elastic neutron scattering studies. The Li ionic conductivity of  $\beta$ -eucryptite compared with other crystalline lithium-ion conductors is shown in Figure 2.12. The high mobility of Li finds it applicable as a battery material [4], [44],

[110]. One can tell that due to this high activation energy, the conductivity of  $\beta$ -eucryptite drops fast and becomes lower than the other oxides at low temperatures, but it is comparable with other Li ion conductors at a high temperature range.

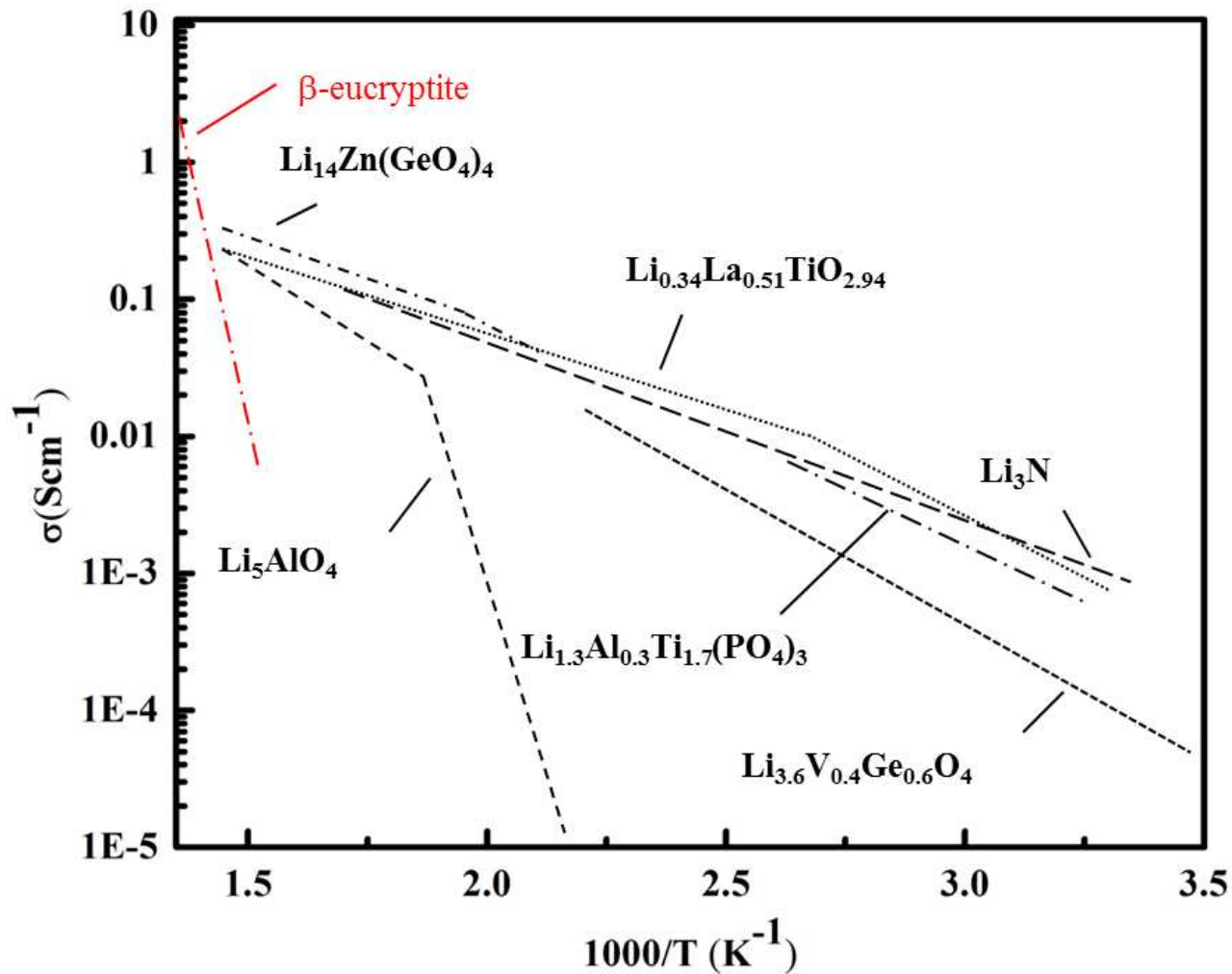


Figure 2.12 Li ionic conductivity of  $\beta$ -eucryptite compared with other crystalline lithium-ion conductors [105], [111]–[115].



The crystal structure of  $\beta$ -eucryptite as a function of temperature has been investigated, and two types of disordering at high temperature were proposed: (1) Li positional disordering, and (2) tetrahedral disordering [9], [32]. Al/Si tetrahedral disordering is kinetically unfavorable, and it requires a long time annealing at a temperature near the melting point from ordered  $\beta$ -eucryptite [32]. The Li order-disorder transition, on the other hand, occurs much more readily. It has been confirmed that Li disordering leads  $\beta$ -eucryptite to undergo a structural phase transition into an incommensurate structure at around 460 °C [5], [9], [27], [36], [116]–[119]. A high-resolution powder neutron diffraction study shows that the  $\text{Li}^+$  ions hop between ideal Wyckoff positions and another vacant site in ordered  $\beta$ -eucryptite [120]. Above the transition temperature, Li ions do not statically occupy only one of the two sets of tetrahedral positions that alternate along the  $c$  axis, but they are dynamically distributed over all possible sites within the channels [10], [27], [28], [32]. Moreover, an intermediate phase is suggested to exist between 442–507 °C [38]. However, the details of this intermediate phase are still not clear. Generally, people use x-ray diffraction or synchrotron radiation to perform crystallographic studies. Since Li is a light element, it is very hard to study the occupancy of Li ions through those measurements. For the materials that have Li conduction, one could learn about the structure changes by measuring Li mobility. Thus, studying the conductivity provides promising information on  $\beta$ -eucryptite structure. Table 2.1 lists several studies on Li ionic conductivity of  $\beta$ -eucryptite through various methods. Despite a large body of work on Li-ion conduction in  $\beta$ -eucryptite, the effects of the grain boundaries on conductivity still remain unknown.

Table 2.1 Li ionic conductivity of  $\beta$ -eucryptite studied by various methods.

| Author (s)         | Ea (eV)  | Temp range (°C) | Sample preparation                           | Experimental methods   |
|--------------------|--|-----------------|--|--|
| Sartbaeva [8]      | 0.89   | 503-540         | Solid state sintering                        | Dielectric spectroscopy  |
| Lichtenstein [121] | 0.8  | -273            |  | DFT calculation  |
| Nagel and Bohm [6] | 0.79   | 30-500          | Single crystal                               | AC-impedance spectroscopy  |
| Bohm [122]         | 0.62 (L)<br>0.83 (H)                               | RT-400          | Single crystal                               | Dielectric measurements  |
| Johnson [40]       | 0.68(glass)<br>1.05(glass-ceramic)                 | RT-600          | Glass to glass-ceramic                       | 2 terminal a.c.<br>4 terminal d.c.<br>2 terminal d.c.<br>Pulsed method |
| Shin-ichi [123]    | 1.02<br>(500K-700K)<br>0.84<br>(700K-1000K)        | 227-727         | Solid state sintering and PLD thin film bulk | AC-impedance spectroscopy  |
| Munro [124]        | 0.75 ( <i>a/b</i> -axis)<br>0.60 ( <i>c</i> -axis) | 25-350          | glass to ceramics                            | DC-impedance spectroscopy  |

## CHAPTER 3

### EXPERIMENTS

This Chapter first introduces the details on synthesis and processing of  $\beta$ -eucryptite from different routes. Later in this Chapter, principles and details of characterization methods are described, including diamond anvil cell, Raman spectroscopy, high energy x-ray diffraction, impedance spectroscopy and Rietveld analysis.

#### 3.1 Synthesis and processing

Generally, ceramic powders can be synthesized through mechanical synthesis (top down) or chemical synthesis (bottom up). Traditional ceramics that consist of mixtures of naturally occurring materials (e.g., clay, minerals, etc.) can be made through mechanical methods such as crushing, grinding or milling. But the characteristics of the powders are not well-controlled. On the other hand, advanced ceramics, such as  $\beta$ -eucryptite, do not occur naturally with high purity. In addition, advanced ceramics usually require high purity with well-controlled grain size and morphology to meet engineering requirements. Thus, one needs to consider using advanced chemical synthesis to “build” the material. The various methods used for producing  $\beta$ -eucryptite powders in the present study are discussed here.

##### 3.1.1 Solid state synthesis

The most popular and simplest method to prepare  $\beta$ -eucryptite uses mixed oxides and/or carbonates. The solid state synthesis is selected for synthesizing  $\beta$ -eucryptite because it was well-documented in the literature [8], [49]. Alumina ( $\text{Al}_2\text{O}_3$ -Sigma Aldrich, St. Louis, MO USA), silica ( $\text{SiO}_2$ -Sigma Aldrich, St. Louis, MO USA) and lithium carbonate ( $\text{Li}_2\text{CO}_3$ -Alfa Aesar, Ward Hill, MA USA) were mixed in the appropriate proportions with a molar ratio of 1:2:1 to

produce stoichiometric  $\beta$ -eucryptite. The mixture was ball milled with yttria-stabilized zirconia (YSZ) balls as grinding media. Calcination was performed at 1100 °C for ~15 hours in a box furnace (Deltech Inc.) in air condition. The resulting material was then ground and resintered at 1300 °C for ~24 hours in the same box furnace and air condition [14], [125]. The simple procedures make solid state synthesis a good choice for synthesizing  $\beta$ -eucryptite. However, the long time and high temperature calcination process requires more energy and results in fairly large particle sizes.

### 3.1.2 Chemical solution technique

The production of  $\beta$ -eucryptite powders through the chemical solution method has been widely developed [42], [126]–[129]. In this process, it can be viewed as a sol-gel process plus a precipitation process.  $\text{SiO}_2$  was formed from a sol-gel route involving hydrolysis and condensation reactions. Hydrolysis occurs when tetraethylorthosilicate (TEOS) and water are mixed in a mutual solvent, generally ethanol [130]. Silica hydrolysis exhibits a minimum rate at  $\text{pH}=7$  and a higher rate at both lower and higher  $\text{pH}$  [131]. At acidic conditions (low  $\text{pH}$  level), the hydrolysis reaction occurs slowly and the silica tends to form linear molecules that are occasionally cross-linked. Gelation takes place through molecular chains entangling and forming additional branches, resulting in fine pore networks and dense structure. Thus, an equal volume of TEOS (Sigma Aldrich, St. Louis, MO USA) and ethanol (95%) were first mixed in a clean beaker with half the volume of distilled water to achieve an R-factor (water moles/TEOS moles) of about 7 [126], [127]. A lot of studies have focused on the effects of catalysts on hydrolysis, condensation, gelation and properties of silica gels [132]–[139].  $\text{HNO}_3$  (approximately 70 wt%) was added to help obtain a clear solution with a  $\text{pH}$  about 0.5-1 after a few minutes of stirring at room temperature. Under these conditions, TEOS is firstly partially hydrolysed to silanol

monomers. The metal ions of  $\beta$ -eucryptite were provided by lithium nitrate ( $\text{LiNO}_3$ -Sigma Aldrich, St. Louis, MO USA) and aluminum nitrate ( $(\text{Al}(\text{NO}_3)_3 \cdot 9\text{H}_2\text{O})$ -Sigma Aldrich, St. Louis, MO USA). An aqueous nitrate solution was then obtained by mixing these precursors and an equal weight of water together with the stoichiometric quantity of the TEOS solution. After about 30 minutes of mixing on a hot plate with a magnetic stirrer at about  $50\text{ }^\circ\text{C}$ , a homogeneous solution was obtained. Condensation and crosslinking of the silanols and gelation of the solution occurred together with aluminium hydroxide precipitates in the form of an amorphous gel by treating the solution with excess aqueous ammonium hydroxide ( $\sim 10\text{-}15\%$ ). Amorphous powders were obtained after drying at about  $80\text{ }^\circ\text{C}$ , and then followed by calcination at  $1100\text{ }^\circ\text{C}$  for 15 hours to form pure  $\beta$ -eucryptite (ICDD PDF Card # 01-070-1574). Figure 3.1 describes the main steps of the chemical solution technique. Synthesizing doped  $\beta$ -eucryptite can adopt this method by adjusting the molar ratio of Li ions and dopants. The chemical solution synthesis method uses nitrates as ion sources and mixes everything in a solution, which provides a very homogeneous mixture. In addition, it is very easy to operate. However, this technique also produces highly agglomerated powders that are not easily dispersed, which requires long time ball milling. In addition, the resulting large grain size easily introduces microcracks during sintering. Particle size analysis (PSA) was used to measure the particle sizes of the powders. As shown in Figure 3.2, the particle size of as calcined powders is as large as about  $100\text{ }\mu\text{m}$ , and after about 100 hours ball milling it decreases down to around  $1\text{ }\mu\text{m}$ .

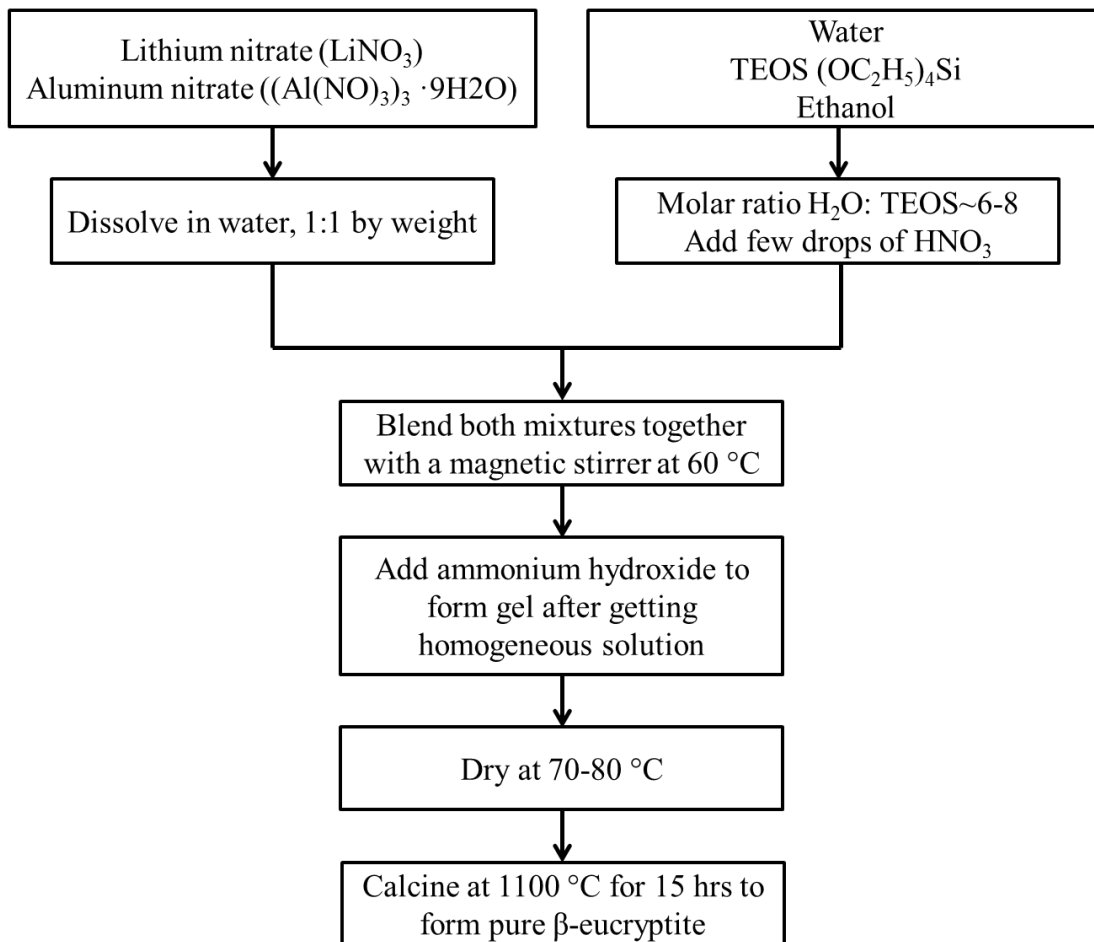


Figure 3.1 A flow chart that describes the major steps for preparing  $\beta$ -eucryptite using chemical solution technique.

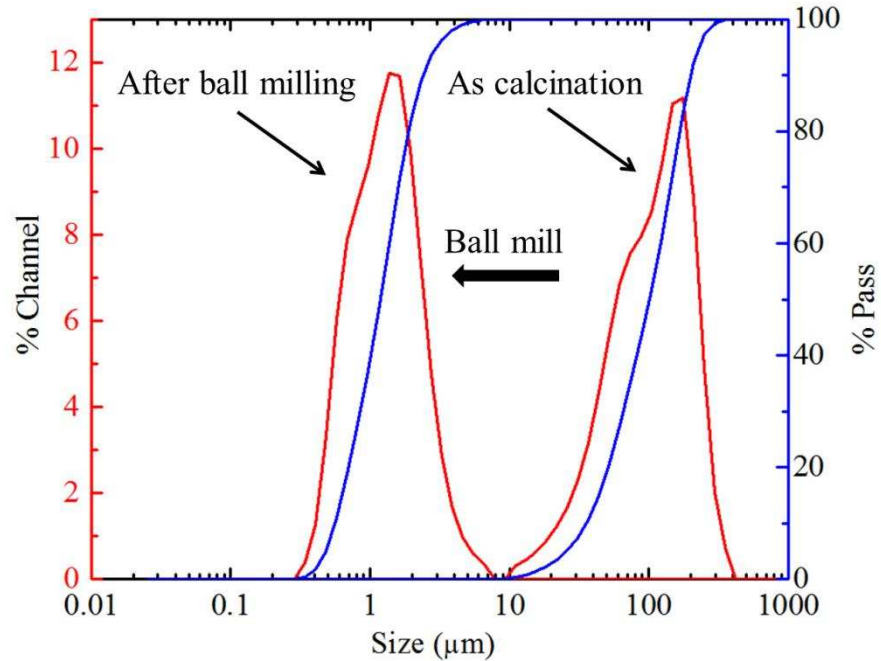


Figure 3.2 Particle size analysis on as calcined powders and powders after ball milling.

### 3.1.3 Wet chemistry synthesis (EDTA-citrate method)

It has been noticed that the long calcination time that required for forming pure  $\beta$ -eucryptite from precipitates in chemical precursor synthesis can easily cause grain growth. In order to decrease the particle size, long time ball milling is necessary for this process, where contamination from the containers may get involved. To get fine  $\beta$ -eucryptite grain size ( $\sim 2 \mu\text{m}$ ) after calcination is very critical. The idea of wet-chemistry synthesis is to allow the metal ions to become fully mixed and chelated in solution and form a uniform network that contains nanoclusters from carbonization, thus getting a fine grain size from the beginning [140].

The EDTA-citrate complexing synthesis method was first introduced by Anderson *et al.* [141] for synthesizing perovskites using ethylenediaminetetraacetic (EDTA) acid and citric acid chelating agents. EDTA acid can hold up to six atoms coordinated to the central metal ion, due to

its hexadentate ligand structure. Citric acid cross-links the complexes to other ligands present in the solution. The EDTA-citrate method using nitrate precursors to synthesize  $\beta$ -eucryptite is discussed below.

The major steps for preparing  $\beta$ -eucryptite using the EDTA-citrate method are shown in Figure 3.3 (Figure 3.3). Aluminum nitrate ( $\text{Al}(\text{NO}_3)_3 \cdot 9\text{H}_2\text{O}$  – Sigma-Aldrich, St. Louis, MO, USA) and lithium nitrate ( $\text{LiNO}_3$  – Sigma-Aldrich, St. Louis, MO, USA) were used as resources of  $\text{Al}^{3+}$  and  $\text{Li}^+$  ions.  $\text{SiO}_2$  colloid (200 nm particle size) was used as a  $\text{Si}^{4+}$  resource instead of TEOS, which was used in the synthesis method described previously since TEOS evaporates easily. Appropriate amounts of citric acid and EDTA were introduced such that the molar ratio of EDTA acid: citric acid: total metal ions was around 1.5:1.5:1. The precursors, EDTA acid and citric acid, were dissolved in  $\text{NH}_3 \cdot \text{H}_2\text{O}$  (8 mol/L) under continuous heating (around  $200^\circ\text{C}$ ) and stirring. The compound ions were chelated with EDTA acid and citric acid to form a stable aqueous solution [140] (Figure 3.4). Precipitation may occur due to the pH value and then nitric acid or ammonium hydroxide was added to adjust the pH value to keep the transparency of the solution. After the excess water evaporated, the chelated solution was thickened to form a viscous translucent gel. Carbonization of the viscous gel took place in a drying oven at  $160^\circ\text{C}$ , resulting in a fluffy black mass. The charcoal was calcined at  $1100^\circ\text{C}$  for 5 hours and finally formed single phase  $\beta$ -eucryptite powders. The x-ray diffraction analysis revealed the same pattern as reported in ICDD PDF Card # 01-070-1574 (Figure 3.5). Figure 3.6 clearly shows the fine particles of  $\beta$ -eucryptite powders made through the wet-chemistry method after calcination.



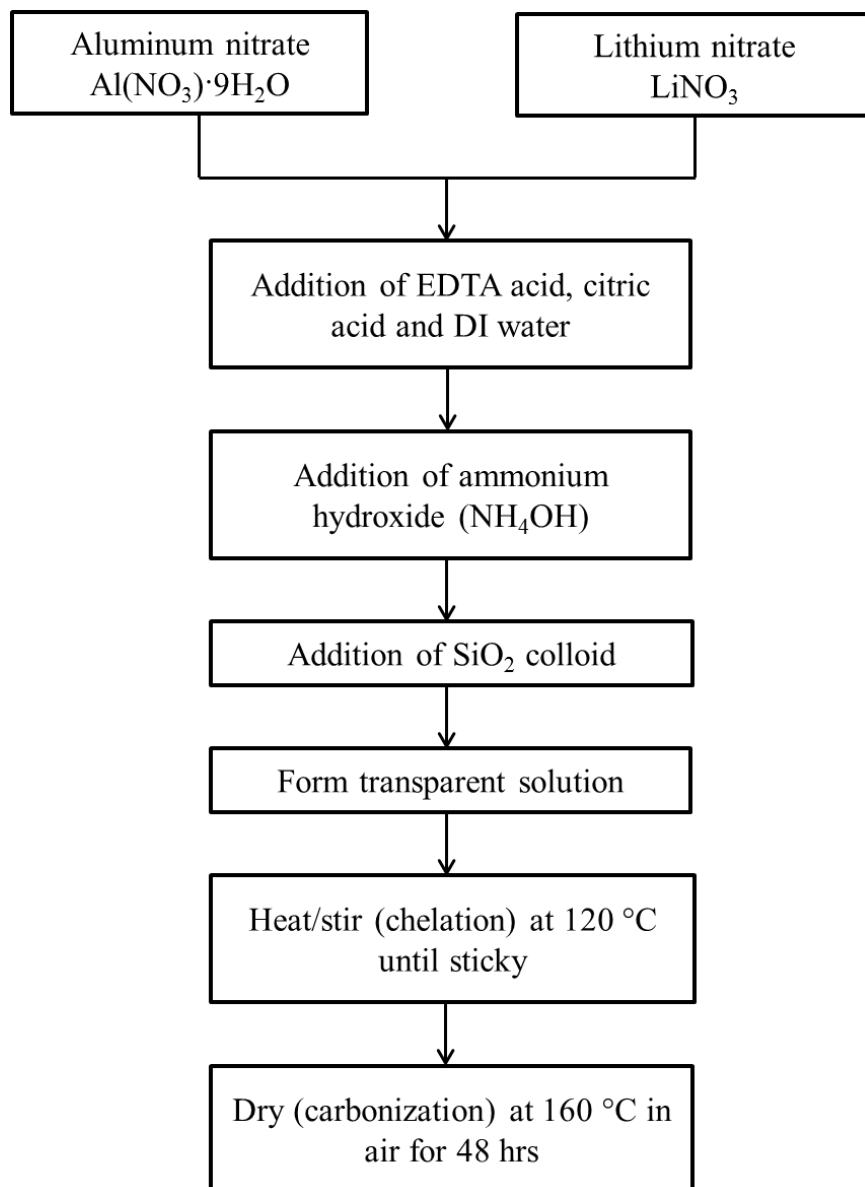


Figure 3.3 A flow chart that describes the major steps for preparing  $\beta$ -eucryptite using EDTA-citrate method



Figure 3.4 Image showing the transparent solution that has  $\beta$ -eucryptite compositions.

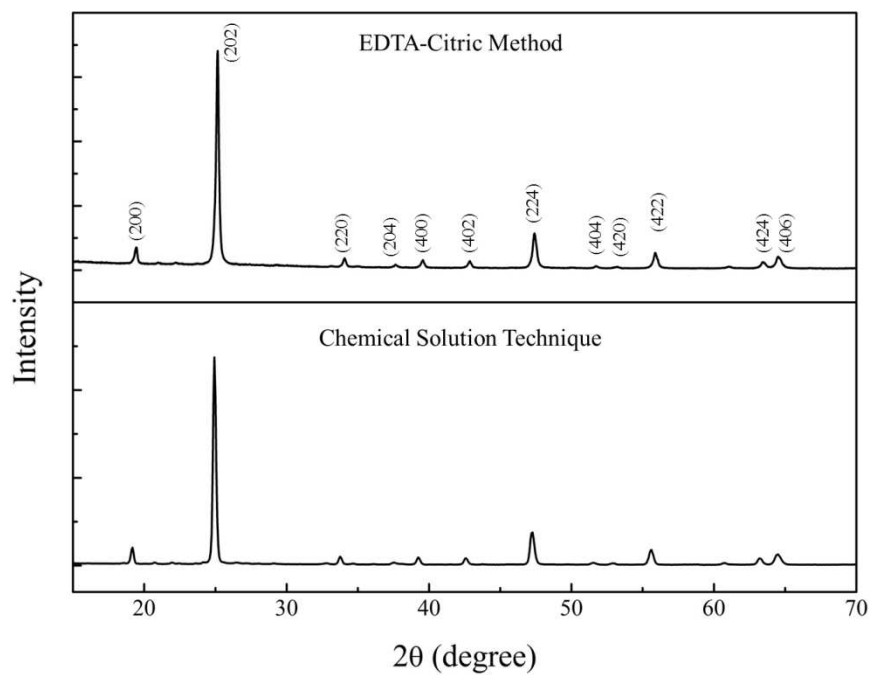


Figure 3.5 Single phase confirmation from XRD on different synthesis routes

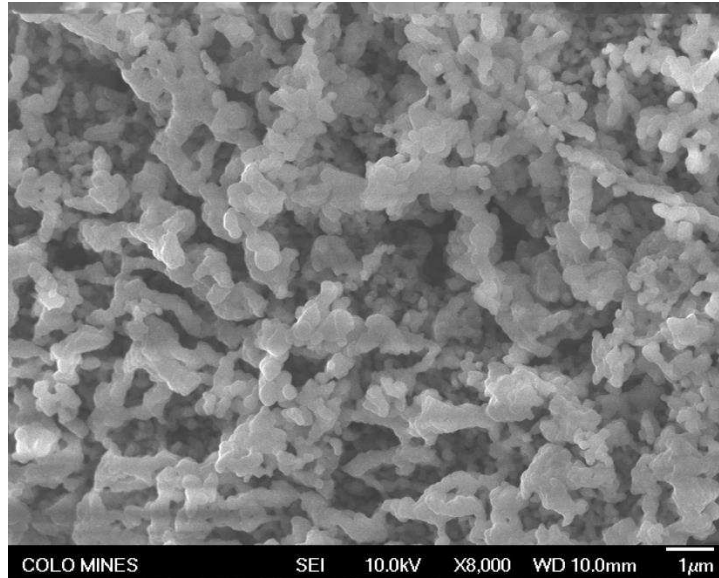


Figure 3.6 SEM image of  $\beta$ -eucryptite powders synthesized from wet-chemistry method after calcination.

#### 3.1.4 Hot pressing

Certain experiments that used in this study require solid pellet samples. The sintering process took place under hot pressing. The synthesized powders were grounded in a ball mill using yttria stabilized zirconia (YSZ) balls as grinding media in alcohol medium to achieve a final particle size of about 1  $\mu\text{m}$ . The fine powders were then sintered in a vacuum hot press (Model: 610 G-25T, Thermal Technology Inc., Concord, NH USA) at 1200  $^{\circ}\text{C}$  for two hours under an applied load of 35 MPa using a graphite die. The graphite papers placed between the powders and the die were coated with boron nitride (BN) to prevent the diffusion of carbon from graphite paper to samples. Cooling rate needs to be very slow (1  $^{\circ}\text{C}/\text{min}$ ), since cracks typically occur with high cooling rate in  $\beta$ -eucryptite due to its anisotropic thermal expansion coefficient. The fracture surface microstructure of  $\beta$ -eucryptite in this sintering condition is shown in Figure

3.7. The density of sintered pellets was measured using Archimedes technique, and all the final densities achieved 98% and above.

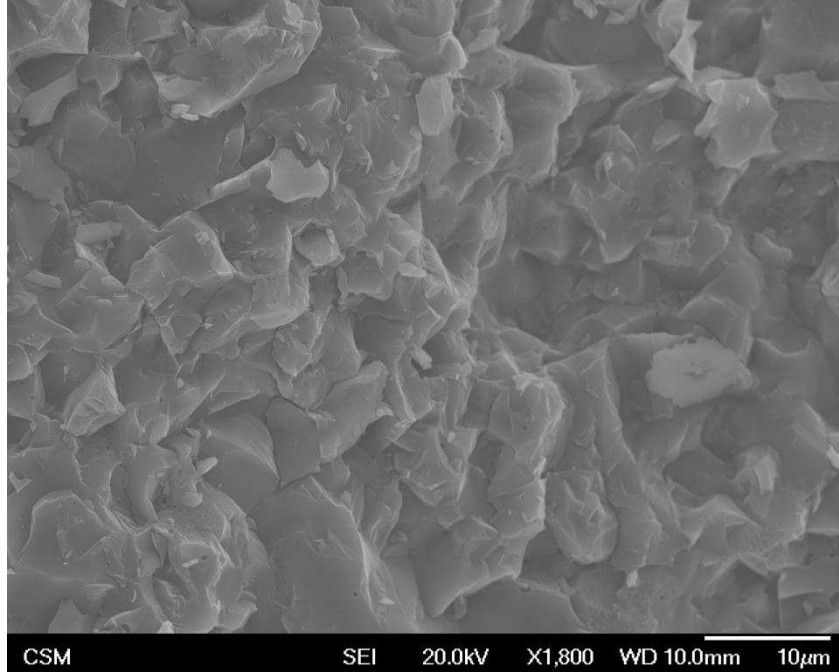


Figure 3.7 SEM image showing the microstructure of the cross section of  $\beta$ -eucryptite pellet processed from hot press sintering.

### 3.2 Diamond anvil cell introduction and calibration

The Diamond anvil cell (DAC) was first developed to study materials under high pressure as Alvin Van Valkenburg and his colleagues realized that they could look through the diamond anvils while the sample was at high pressures [142]. The basic idea of DAC is to apply pressure on a small amount of samples by pushing two diamond culets with flat surfaces towards each other. A schematic of a general DAC is displayed in Figure 3.8 [143]–[149]. A stainless steel gasket with a hole in the middle needs to be placed in between the upper and lower

diamonds to serve as a sample chamber (shown in Figure 3.9). The reasons that make diamond an ideal material for containing high-pressure samples are (1) diamond is the hardest material with a high compressive strength, and (2) diamond is transparent to X-ray, visible light and infrared. Thus diamonds could provide a clear window for those radiations, which makes diamond a perfect choice for studying various properties of material *in-situ* under high pressures. DAC was later developed to be used at high temperatures up to 4000 K, rather than under pressure only. The DAC technique has provided an impressive amount of information about materials at high pressures and high temperatures. In the present study, Raman spectroscopy and X-rays were used to study the pressure induced phase transformation of  $\beta$ -eucryptite.

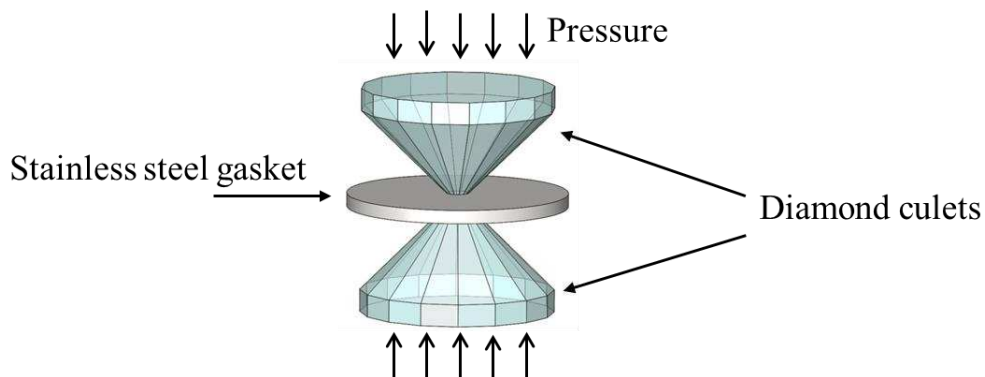


Figure 3.8 Schematic description of using diamond culets to create pressure on samples.

### 3.2.1 Classes of DAC

Diamond anvil cells can be divided into two main groups: screw-type (screw/bolt driven DAC) and gas-membrane type (pneumatic driven DAC). In general, screw-driven DACs have three or four screws connecting the two diamond holders together, and force is loaded by tightening the screws directly onto diamond anvils or through a system of levers, arms, or

wedges [139], [143], whereas in a gas-membrane DAC, pressure is created by the expansion of a membrane, which is filled with gas and pushes the two parts of the cell towards each other. In both types, the pressure is given by the two diamond culets as described above. The strong and weak sides of the two types are listed in Table 3.1.

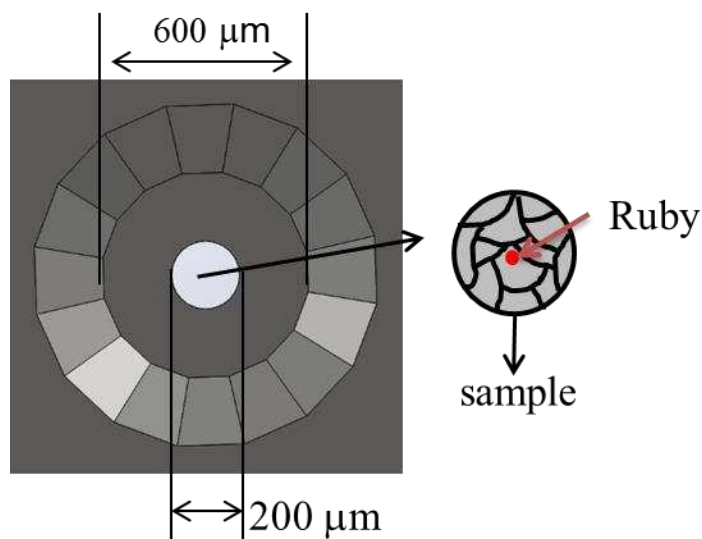



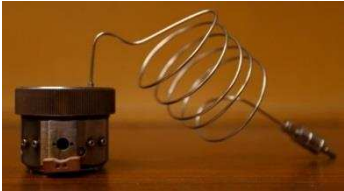
Figure 3.9 Schematic of a stainless steel gasket which placed between the two diamond culets.

### 3.2.2 Gasket technology

In the early days of diamond anvil cell work, the sample was simply placed on the face of the lower diamond anvil. The upper anvil was then lowered onto it, and the sample was squeezed between the upper and lower anvil faces. As force was applied, the sample extruded from between the anvils until it was so thin that it ceased to flow. This usually results in the forming of a very smooth pressure gradient from highest pressure in the center to low pressure at the edges [142]. Therefore, it is important to introduce a gasket in a high pressure cell to provide a

chamber for the sample confinement, pressure marker, and pressure medium. Generally, the gasket is prepared by pre-indenting a metal foil (250  $\mu\text{m}$ -300  $\mu\text{m}$  thick) to 1/3 of original thickness between the upper and lower diamonds and drilling a small hole through the center of the indentation created by the culets. The most commonly used gasket materials are stainless steel, tungsten, Inconel (Ni-Cr-Fe) alloy, or rhenium [17].

Table 3.1 Comparison of two types of diamond anvil cells

|               | Screw-driven type  | Gas-membrane type  |
|---------------|--|--|
| Example       |    |   |
| Advantages    | <ul style="list-style-type: none"> <li>• Simpler construction</li> <li>• Ease of checking the diamond alignment</li> <li>• Ease of movement from place to place with pressure maintained inside, even for a long time</li> <li>• No need for a gas controller</li> </ul> | <ul style="list-style-type: none"> <li>• More accurate control over pressure in the sample chamber</li> <li>• Remote pressure adjustment allowed without touching and moving a DAC</li> <li>• Ease of controlling for high temperature tests</li> <li>• The piston fits tightly so that alignment will be maintained under pressure</li> </ul> |
| Disadvantages | <ul style="list-style-type: none"> <li>• Difficulty controlling the increasing step due to the manual rotation of the screws</li> </ul>  | <ul style="list-style-type: none"> <li>• Difficulty aligning the diamonds and loading the samples due to the existence of the piston and the gasket stage</li> <li>• Complex construction needs to be connected to a gas controller and a gas cylinder, needs more space to run the tests</li> </ul>   |

### 3.2.3 Pressure markers at room temperature

Determining the pressure value in a diamond anvil cell is of critical importance for high pressure tests. In early days, people who used diamond anvil cells for XRD studies were able to measure the lattice parameters of the calibrator, which were mixed with sample powders. NaCl, for example, was found to be a good pressure reference, due to the linear compression of NaCl below 15 GPa [150]–[153]. This method works well for those who are using XRD, but makes it hard for others who are using other techniques to study high pressure behaviors [142]. Making an XRD pattern just for determining pressure seems inconvenient.

The ruby fluorescence method was developed to determine the pressure in 1971 [142]. Unlike NaCl, the wavelength of the ruby fluorescence changes with pressure and could be easily calibrated. The calibration of Ruby R lines under pressure has been performed up to 150 GPa [154]. Ruby is corundum doped with chromium ( $\alpha$ -Al<sub>2</sub>O<sub>3</sub>), with Cr<sup>3+</sup> ions substituting for the aluminum, which results in the system Al<sub>2</sub>O<sub>3</sub>-Cr<sub>2</sub>O<sub>3</sub> forming a complete solid solution between the two oxide phases [155]. Doping of corundum by Cr results in a small expansion of the host lattice and an off-center displacement from the central octahedral positions, due to the Cr<sup>3+</sup> ion (0.064 nm) having a slightly larger ionic radius than Al<sup>3+</sup> (0.057 nm) [155]. Under laser excitation, the transition from the two lowest energy excited states to the ground state are denoted as R1 and R2 peaks [17], which are spin-forbidden no-phonon emissions [155], [156]. They are observed near 14404 cm<sup>-1</sup> (694.25 nm) and 14433 cm<sup>-1</sup> (692.86 nm) at room temperature [154], [155], [157], [158]. Under hydrostatic conditions and room temperature, the R1 and R2 lines nearly shift by the same amount ( $\sim 7.6$  cm<sup>-1</sup>/GPa), and the R1-R2 separation remains the same (shown in Figure 3.10). The depth of the trough between the two peaks is very sensitive to peak broadening, which is very sensitive to non-hydrostaticity [142], [159], [160].



The shift of the R2 is little affected by non-hydrostatic strain, while R1 line shift is more sensitive to inhomogeneous strain.[161] In other words, ruby not only can be used as a pressure calibrator, but it also provides a quick way to check whether the pressure media is continuing to act like a liquid. Ruby therefore became a widely used pressure marker in diamond anvil cell high pressure study by mixing a small chip of ruby crystal in the sample [155], [159], [160], [162]–[165]. For the tests lower than 5 GPa with the presence of a pressure medium, there is only a negligible difference observed between the pressures calculated through R1 and R2 line shifts.

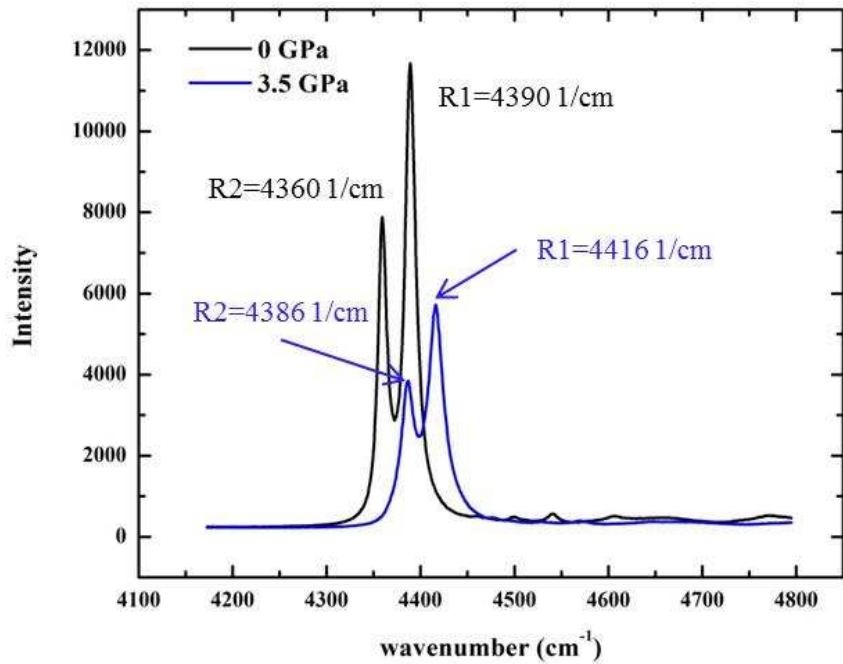


Figure 3.10 Ruby fluorescence spectra under pressure

### 3.2.4 Pressure markers at high temperature

It is hard to use ruby as the pressure marker at very high temperatures because the ruby signal starts to fade when the temperature is over 400 °C [166]. Sm: YAG and SrB<sub>4</sub>O<sub>7</sub>: Sm<sup>2+</sup> were proposed as alternative substances for a temperature range up to 500-600 °C [167]–[170]. However, those materials are not inert to samples and easily dissolve into supercritical H<sub>2</sub>O fluid [166]. Many investigators prefer to use a chemically inert pressure marker, which is suitable to be used at high temperature with a standard optical spectrometer in a synchrotron facility, due to the beamtime limitation. <sup>13</sup>C diamond is a good candidate, since it has a Raman peak at a lower frequency than a usual <sup>12</sup>C diamond below 13 GPa. Yet, when pressure is higher than 13 GPa, this peak overlaps with a Raman peak from an anvil composed of <sup>12</sup>C diamond [166], [171]. Besides, <sup>13</sup>C chips are not commercially available. Gold is another good candidate, since it is chemically inert and it is an efficient scatterer of X-rays [142], [172]. However, for the measurements other than X-rays, it becomes hard to use gold (similar with NaCl as a pressure marker at room temperature). Kawamoto *et al.* [166] discussed the possibility of cubic boron nitride (*c*BN) being a new pressure marker at high temperature by comparing high pressure and temperature experiments using ruby and gold pressure markers. The advantages of *c*BN are that the Raman TO band (1054 cm<sup>-1</sup> at ambient) is intense and well separated from that of diamond anvils (1333 cm<sup>-1</sup> at ambient). Moreover, *c*BN is thermally and mechanically stable over a large *P-T* range and is chemically resistant to corrosive media [173]. This pressure scale should be useful up to 100 GPa and temperatures in excess of 1000K [173]. The comparisons of commonly used optical sensors mentioned above are listed in Table 3.2.

Table 3.2 Summary of useful optical pressure sensors for high temperature high pressure studies

| Sensor  | $\lambda_0$ or $\nu_0$<br>(at 295K) | Pressure coefficient<br>(/GPa) | Temperature<br>coefficient (cm <sup>-1</sup> /K) | Useful P-T<br>range       |
|---|-------------------------------------|--------------------------------|--|---------------------------|
| Ruby (R1 line)<br>[144], [174]–[178]                              | 694.28 nm                           | 7.6 cm <sup>-1</sup>           | 0.115  | 0-250 GPa,<br>0-700 K     |
| SrB <sub>4</sub> O <sub>7</sub> :Sm <sup>2+</sup><br>[159], [179] | 684.41 nm                           | 0.255 nm                       | ~0   | 0-250 GPa,<br>0-900 K     |
| c-BN (TO band)<br>[180], [181]                                    | 1054 cm <sup>-1</sup>               | 3.27 cm <sup>-1</sup>          | -0.021   | 0-100 GPa,<br>300-2500 K  |
| <sup>12</sup> C (LTO band)<br>[157], [182], [183]                 | 1332.5 cm <sup>-1</sup>             | 2.83 cm <sup>-1</sup>          | -0.016   | 15-150 GPa,<br>300-2500 K |
| <sup>13</sup> C (LTO band)<br>[157], [182], [183]                 | 1284.05 cm <sup>-1</sup>            | 2.83 cm <sup>-1</sup>          | -0.016   | 0-13 GPa,<br>0-2500 K     |

Although it is not possible to use ruby over 400 °C, the experiments in the present study were carried out under 200 °C. Wunder and Schoen [176] pointed out that in the temperature interval 25-300 °C and pressure interval 0-4 GPa, the temperature and pressure coefficients of the frequency shift of ruby fluorescence are independent of each other. That is

$$d\mathcal{G} = \alpha dT + \beta dP \quad (3.1)$$

where  $\mathcal{G}$  is the frequency shift of ruby fluorescence;  $\alpha$  and  $\beta$  are the temperature coefficient and pressure coefficient of ruby frequency shift, respectively. The relation of  $\alpha$ ,  $\beta$  and  $\mathcal{G}$  can be expressed by:

$$\alpha = \left( \frac{\partial \mathcal{G}}{\partial T} \right)_P, \beta = \left( \frac{\partial \mathcal{G}}{\partial P} \right)_T, \frac{\partial^2 \mathcal{G}}{\partial T \partial P} = 0 \quad (3.2)$$

Calibration of ruby R lines shifts with temperature at ambient pressure was carried out from 25-250 °C, and is shown in Figure 3.11. Plotting the R1 and R2 peak positions as a function of temperature yields a temperature coefficient  $\sim 0.115 \text{ cm}^{-1}/^{\circ}\text{C}$  (Figure 3.12).

### 3.2.5 Synthesis of $\text{SrB}_4\text{O}_7: \text{Sm}^{2+}$

The sample of  $\text{SrB}_4\text{O}_7: \text{Sm}^{2+}$  was synthesized through the wet-chemistry method [140].  $\text{Sr}(\text{NO}_3)_2$ ,  $\text{Sm}_2\text{O}_3$ ,  $\text{H}_3\text{BO}_3$  were calculated in amounts corresponding to  $\text{Sr}_{0.95}\text{Sm}_{0.05}\text{B}_4\text{O}_7$  stoichiometry taking into account  $\text{Sm}^{3+}$  to  $\text{Sm}^{2+}$  reduction [184].  $\text{Sm}_2\text{O}_3$  was first dissolved in nitric acid and mixed with  $\text{Sr}(\text{NO}_3)_2$  and  $\text{H}_3\text{BO}_3$ . Then appropriate amounts of citric acid and EDTA acid were introduced such that the molar ratio of EDTA acid: citric acid: total metal ions was around 1.5:1.5:1. The precursors, EDTA acid and citric acid, were dissolved in  $\text{NH}_3 \cdot \text{H}_2\text{O}$  (8 mol/L) under continuous heating (around 200 °C) and stirring. The compound ions were chelated with EDTA acid and citric acid to form a stable aqueous solution. Precipitation sometimes occurred due to the pH value, and then nitric acid or ammonium hydroxide were added to adjust the pH value to let the solution become transparent. After evaporating the excess water, the chelated solution was thickened to form a viscous translucent gel. Carbonization of the viscous gel took place in a drying oven at 160 °C, resulting in a fluffy black mass. The charcoal was calcined at 850 °C for 40 hrs, and finally formed light pink color powders. The x-ray diffraction analysis revealed the same pattern as reported [184], [185]. The fluorescence spectrum measured is shown in Figure 3.13, which is comparable to literature [169], [184].

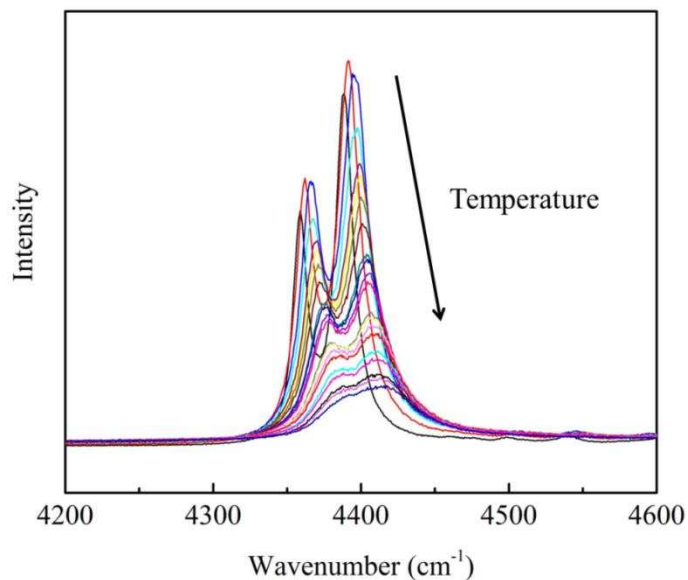


Figure 3.11 Ruby R lines shifts under temperature. The arrow points the direction of increasing temperature and the highest temperature in this calibration is 250 °C.

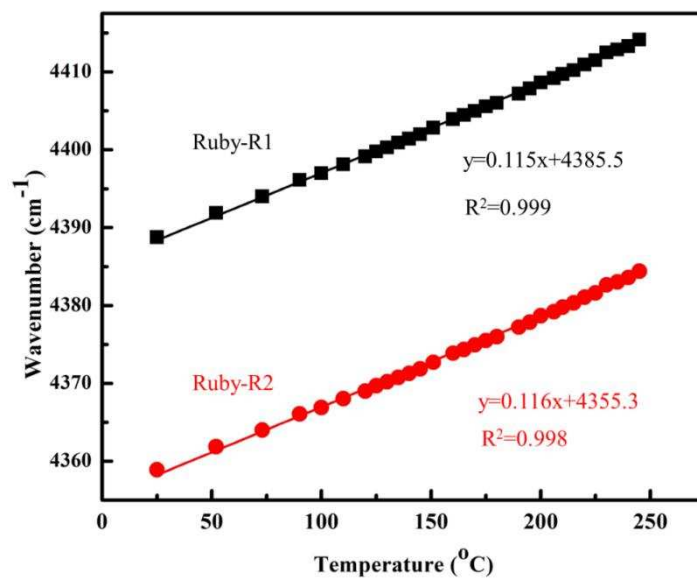


Figure 3.12 The relations of Ruby R peak positions and temperature from 25 °C to 250 °C. The equations represent the fitting of R positions as a function of temperature, which can be used to calculate the temperature coefficient of Ruby.

The calibration of SrB<sub>4</sub>O<sub>7</sub>: Sm<sup>2+</sup> under pressure was carried out in a diamond anvil cell (Diacell HeliosDAC A59000, EasyLab Technologies Ltd., Berkshire, UK). SrB<sub>4</sub>O<sub>7</sub>: Sm<sup>2+</sup> crystals and ruby crystals were both introduced into the sample chamber, and a 16:3:1 mixture of methanol: ethanol: water was introduced as pressure medium. Both ruby and SrB<sub>4</sub>O<sub>7</sub>: Sm<sup>2+</sup> spectra were scanned at the same pressure. Using ruby as a pressure reference to calculate the pressure value yielded the SrB<sub>4</sub>O<sub>7</sub>:Sm<sup>2+</sup> peak shifts as a function of pressure (Figure 3.14), resulting in a slope of 5.34 cm<sup>-1</sup>/GPa (0.25 nm/GPa), which is in the range of 0.245 nm/GPa and 0.255 nm/GPa as reported [169], [186]. SrB<sub>4</sub>O<sub>7</sub>: Sm<sup>2+</sup> peaks shift with temperature was also calibrated using the same way as ruby under temperature calibration described above. A linear fit of the temperature shift of the SrB<sub>4</sub>O<sub>7</sub>: Sm<sup>2+</sup> led to dλ/dT=-0.0032 cm<sup>-1</sup>/GPa, which can be ignored as expected.

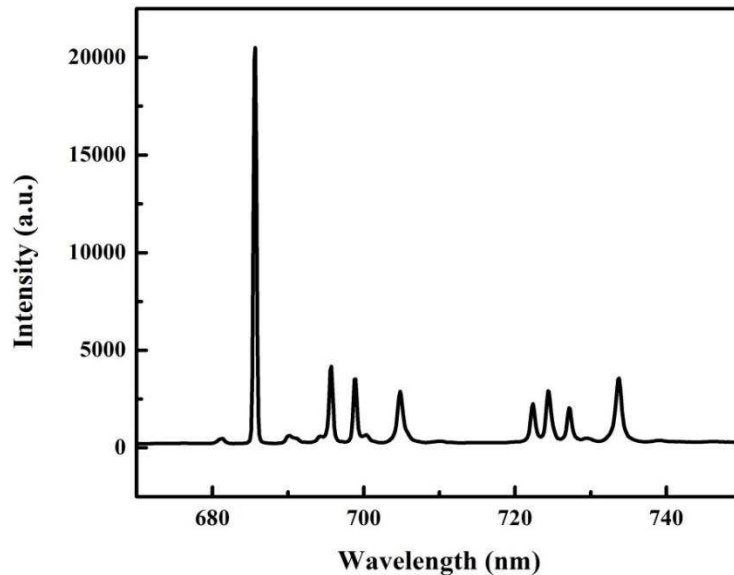


Figure 3.13 The fluorescence spectrum of SrB<sub>4</sub>O<sub>7</sub>: Sm<sup>2+</sup> excited by a 532 nm laser.

cBN has also been considered as potential pressure markers in this study. However, cBN has comparably lower intensity and requires longer integration time than ruby and SrB<sub>4</sub>O<sub>7</sub>: Sm<sup>2+</sup>. Using cBN as a pressure marker seems harder than the other two candidates. SrB<sub>4</sub>O<sub>7</sub>: Sm<sup>2+</sup>, on the other hand, has a fairly high intensity even at high temperatures and pressures. In addition, SrB<sub>4</sub>O<sub>7</sub>: Sm<sup>2+</sup> barely shifts with temperature, which makes it an even better pressure marker than ruby at high temperatures.

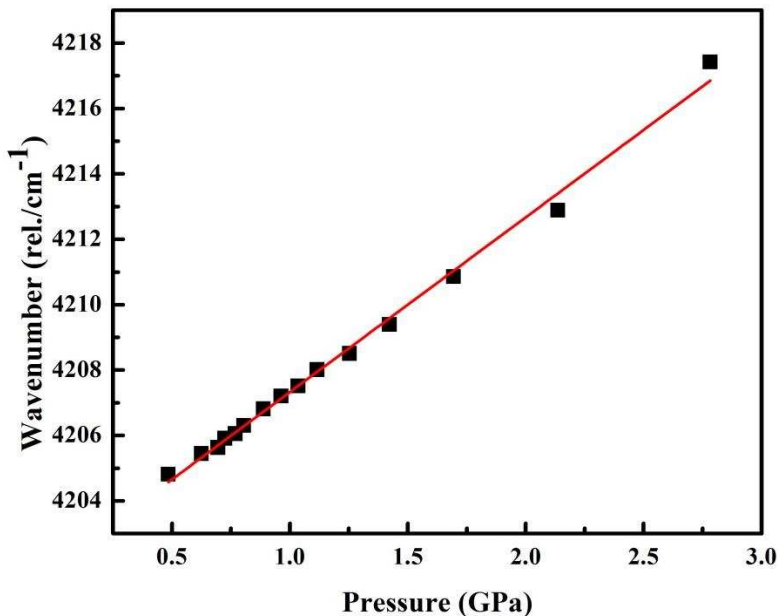


Figure 3.14 SrB<sub>4</sub>O<sub>7</sub>: Sm<sup>2+</sup> peak position as a function of pressure

### 3.2.6 Pressure medium

Materials may behave differently under non-hydrostatic conditions and may promote or suppress phase transitions. The non-hydrostatic conditions also cause difficulties in quantifying the pressure by the ruby fluorescence technique or internal diffraction standards. Thus, the pressure media play an important role in high pressure studies by providing a hydrostatic pressure on the samples and reducing the pressure gradient in the gasket [148], [187]. First, the

pressure medium should not react with the sample during tests. In addition, the medium should not overlap significantly with peaks from the sample, for example in XRD or Raman spectroscopy [17]. Generally, rare gasses and organic solvents are widely used as pressure media in high pressure studies.

Rare gases become fluid at a pressure of a few hundred MPa at room temperature and are stable over a wide pressure range, offering purely hydrostatic pressure environments. Rare gas fluids other than helium solidify in a pressure range of 0.4-12 GPa. After solidification, rare gas solids gradually lose the ability to provide hydrostatic conditions in the same way as other solid pressure media do [188]. Helium, on the other hand, has been observed with no evidence of non-hydrostaticity until at least 50 GPa [188], [189]. Two ways have been developed to load the rare gases to a DAC: one is using the cryogenic technique to liquefy the gases, and the other is using a gas compressor to densify the gases at room temperature [188]. Gases have different boiling temperatures, which makes it impossible for the cryogenic technique to load gas mixtures. Besson and Pinceaux [190], who loaded helium to a DAC, were the first to use the high-pressure-gas-loading method. They proved helium to be remarkably inert and to be the best pressure-transmitting medium for solid-state studies [190]. However, helium does have its own shortcoming. Helium atoms are so small and can easily diffuse into the crystal lattice of the samples [191], [192].

Organic solvents are also widely used as pressure mediums as they are easy to work with. A mixture of 4:1 methanol-ethanol was developed and confirmed to provide a quasi-hydrostatic environment to about 9.8 GPa [187]. A small addition of water in the proportion 16:3:1 H<sub>2</sub>O to methanol-ethanol extends the hydrostatic range to 14.5 GPa [145]. Table 3.3 shows the comparison of some pressure media that are commonly used and their useful pressure ranges.



Table 3.3 Commonly used pressure mediums and their conditions

| Medium                        | Pressure range of nearly hydrostatic behavior (GPa) | Loading technique                  |
|-------------------------------|---|------------------------------------|
| Helium                        | ~50   | Cryogenic or high-pressure filling |
| Methanol:ethanol=4:1          | ~9.8  | Easy filling                       |
| Methanol:ethanol:water=16:3:1 | ~14.5   | Easy filling                       |

### 3.2.7 High temperature in a diamond anvil cells

#### (a) External resistance heating

Temperature was first applied to a diamond anvil cell because researchers were trying to observe the effect of temperature on crystals as they grew from liquids [142]. Samples could be heated with a cylindrical heater placed around the anvils. Later, researchers found that temperature could be routinely brought up to 1000 °C by wrapping resistance wires around the diamond based on the fact that diamond is a good thermal conductor [142].

#### (b) Laser heating

Higher temperature may also be required for the high-temperature-high-pressure studies. Heating samples with a focused laser beam was first proposed in 1966 [142]. First laser heating was applied through a pulsed ruby laser, although this laser was hard to control. These experiments worked best when dark-colored particles of the sample were surrounded with a transparent, insulating medium such as NaCl [142]. Eventually, investigators switched to a YAG laser with a 1.06 μm emission and 60W maximum power. This technique could bring the temperature up to 2000 °C depending on the focusing [169] and allow a rapid quenching (around  $2 \times 10^6$  °C/s) due to the local character and the very high thermal conductivity of

diamond anvils [193]. Laser heating, while capable of very high temperatures, has the disadvantages of creating non-uniform temperatures and very steep thermal gradients [142]. Nowadays, the uniformity of the temperature across a heated spot has been improved by using a laser mode with a larger diameter. Moreover, using a more powerful laser helps to minimize temperature fluctuation during continuous laser heating [142].

#### (c) Internal resistance heating

For those who study a sample that is electrically conducting, the sample itself can be made to serve as the heater. The first case was in 1974, when people were trying to collect data on pure iron at simultaneous high pressure and temperature. They ran a very fine iron wire between two large electric leads, surrounded it with  $\text{Al}_2\text{O}_3$  and  $\text{MgO}$  between the diamond anvils, and applied 60 Hertz AC to heat the sample [142]. However, there are still a lot of researchers not working on electrically conducting materials who also would like to have access to very high temperature and pressure in a diamond anvil cell. Chang-Sheng Zha had an idea of using a thin metal strip with a hole in it to receive a solid sample. Bassett later helped him by laser machining a fine rhenium strip with a hole only microns across to receive the sample [142]. Cornell High Energy Synchrotron Source (CHESS) by then was able to provide an extremely small, intense X-ray beam, which was able to pass through the very small sample and obtain X-ray data on it. This is a very difficult experimental procedure but has great potential.

### 3.2.8 Experimental set-up

#### (a) Alignment check

Checking alignment before each test and/or pre-indentation is very important because altered diamonds may lead to an uneven pressure in the cell and may even break. For the gas-

membrane type DAC (Diacell HeliosDAC A59000, EasyLab Technologies Ltd., Berkshire, UK), the aligning should be based on the following procedures:

1. Clean the anvils' surfaces with a cotton bud or a small stick wrapped in tissue moistened with acetone or alcohol.
2. Insert the two extraction screws into the cell from the bottom of the cylinder and screw them in far enough to prevent the piston anvil from touching the lower anvil.
3. Carefully insert the piston into the cell body until it touches the extraction screws.
4. Let the cell stand on its side and view down the microscope through the lateral holes at about  $\times 40$  magnification. Lower the piston by unscrewing the extraction screws. As the piston is further inserted, you will be able to see the anvils approaching each other through the lateral holes. In this way, gently bring the anvils almost but not quite into contact.
5. Diamond culets could be misaligned in two ways: translation-wise (Figure 3.15 (a)) or tilt (Figure 3.15 (b)). Check through each set of lateral holes to ensure that the anvil culets match translation-wise. Then, check through the top of the cell. If the cell is correctly aligned, when the anvils are in contact there should be a clear, probably colored, field of view, or perhaps part of a colored fringe may be seen. If the culets are translation-wise misaligned, the reflection of the surfaces of the two culets will not be on top of each other; in other words, two dislocated bright circles shall be seen (Figure 3.15 (a)). In this case, use the four lateral screws to move the lower plate until the two anvil culets are coincident. If the culets are far from parallel, the fringes will be seen as a closely-spaced set of lines at one side of the field of view (Figure 3.15 (b)). The fringes can be removed by altering the three tilt adjustment screws on

the piston. It will require some practice as the movements needed are generally quite small. Finally, tighten all screws.

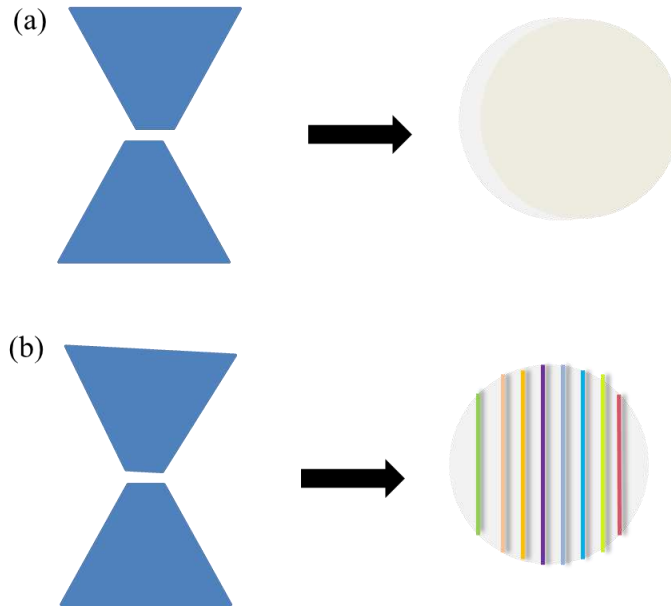


Figure 3.15 Misaligned diamonds culets and how they look like from the top of the cell

(b) Gasket pre-indentation procedure

(c) Each gasket blank needs to be pre-indented to a desired thickness before it gets drilled.

The procedure of pre-indenting varies with different types of diamond anvil cells. The detailed procedure of the gas-membrane type is as follows:

1. Align the diamond anvils.
2. Measure the thickness of the gasket blank.
3. Make a clear orientation mark between the gasket and the cell (gasket needs to be in the exact same position when it needs to be re-loaded)
4. Place the gasket on the bottom anvils of the cell, just as one performs the experiments.
5. Close the cell without dislodging the gasket.

6. Use the clamping screws to apply pressure to the gasket by tightening these screws. Do this in small steps and increments. Use a cross-tightening pattern so that the piston remains parallel to the cylinder.
7. Release the screws and open the cell.
8. Check and measure the thickness of the indentation in the gasket. One is looking for a pre-indentation thickness of about  $1/3$  of the original thickness of the gasket blank.
9. Quickly check that if the diamond anvils are still aligned.
10. If the thickness has not reached the desired level, re-load the gasket back in the same orientation as before and repeat the above steps until the thickness reaches the desired value.

(d) Pressure tests only

Setting up a diamond anvil cell for pressure tests of both screw-driven type and gas-membrane type is straightforward. There are several tips that could help with the setting up:

1. One could mix the medium with samples first and then pick up a small amount of the mixture and put it into the chamber. In this way, it is easier to operate sample loading and also prevent samples from floating away by the medium droplets.
2. After placing the pressure plate on the piston, one needs to tighten the gas membrane on the cell. The gas membrane needs to be screwed as tight as one can. Otherwise, there will be space between the membrane and the pressure plate. When the gas flows in, it will cause the membrane to deform first to reach the plate surface instead of applying pressure on the sample. This will make the membrane exceed its deformation limitation and it won't be usable anymore.

(e) Pressure and temperature tests

The gas-membrane type diamond anvil cell also allows one to apply temperature on the samples together with the pressure. To avoid the tarnishing of the interior of the cell and the exposed faces of the diamond anvils, a mildly reducing gas, such as an argon-2% hydrogen mixture, needs to be flushed through the system. The assembling of the diamond anvil cell needs to be changed as shown in Figure 3.16. Lower and upper mica disks need to be located for high temperature tests. A thermocouple probe can be inserted through the probe holder until the tip of the probe reaches the foot of the lower diamond anvil and the thermocouple probe measures the temperature at the level of the lower diamond anvil. A thermocouple reader for thermocouple type-K is needed in order to read the temperature.



Figure 3.16 Assembling the diamond anvil cell for high temperature tests.

### 3.3 *In-situ* DAC-X-ray diffraction

Synchrotron radiation is generally emitted by charged particles (electrons and ions) that are accelerated in a curved path or orbit. The schematic diagram illustrating the output of synchrotron radiation is shown in Figure 3.17. The storage ring consists of several magnets, which constrain an electron or positron beam to move in a circular path. The electrons change

direction at each bending magnet which has its field perpendicular to the plane of the ring, being subjected to an inward radial acceleration [194]. Synchrotron radiation provides five orders of magnitude more x-radiation than conventional sources such as x-ray tubes [195]. This produces electromagnetic radiation (synchrotron radiation), which is emitted at a tangent to the orbit. The loss of energy in this way is replenished by supplying an appropriate electromagnetic radiation input in one or more of the straight sections between bending magnets [196]. Synchrotron radiation offers various benefits, such as high intensity, broad spectral range, high polarization, high-vacuum environment, small-source-spot size and stability. These properties make synchrotron radiation an important experimental tool [195].

High pressure coupled with synchrotron x-ray diffraction is recognized as a powerful technique for discovering novel physics and chemistry with a wide spectrum of applications. In the present study, DAC is used in conjunction with synchrotron radiation to study pressure-induced phase transformation of  $\beta$ -eucryptite at Cornell High Energy Synchrotron Source (CHESS) B1 station. Research capabilities at CHESS B1 station include a three-dimensional rotating stage for side x-ray diffraction, laser-excited Raman spectroscopy, Mar345 detector control system etc. The beam is stopped down to about 3 mm before entering the station and further reduced to the final beam size of 5 to 1000 microns by a set of apertures. A schematic of the diffraction stage and optical system in the B1 hutch is shown in Figure 3.18. Ruby pressures are measured by a miniature solid state laser (532 nm). Due to the experimental set-up at CHESS B1 station, DAC needs to be removed from the hutch to be placed under laser exposure, so screw-type DAC is being used for convenience.

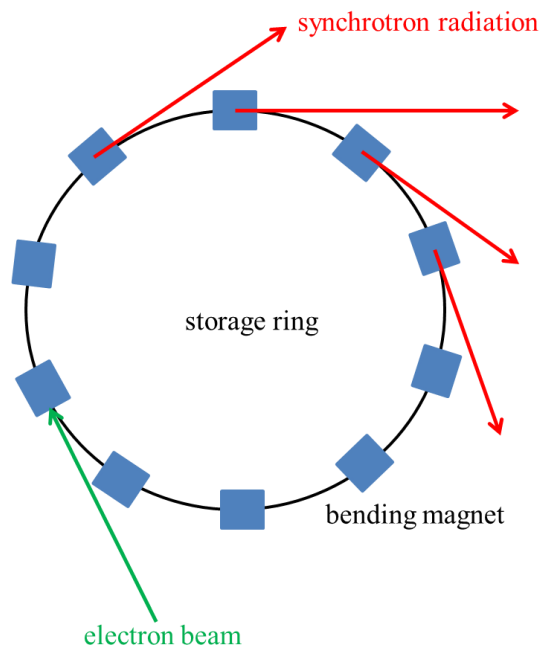


Figure 3.17 Schematic diagram showing the output of synchrotron radiation from bending magnets.

After sample exposing under synchrotron radiation for 20 mins, a typical frame with Debye-Scherrer rings is collected on the 2D detector (Figure 3.19). One needs to visualize the data by using Fit2D program [197]. The 2D frame can be converted to 1D pattern by “caking” and integrating the data through the Fit2D package [198]. In order to perform the conversion, sample-to-detector distance, rotation, and angle need to be calibrated through a standard material, such as  $\text{CeO}_2$ .



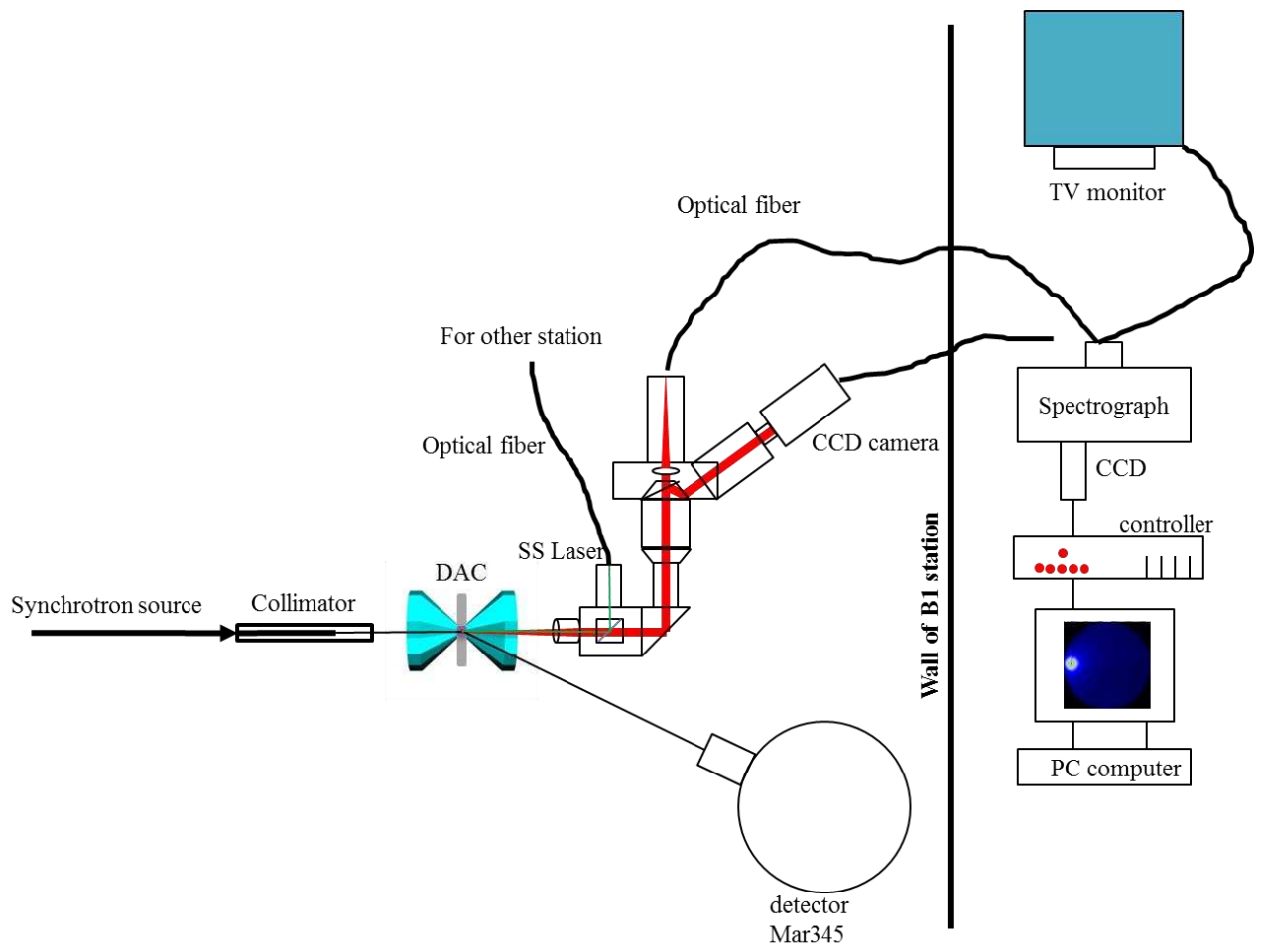


Figure 3.18 Schematic of the diffraction and optical system.

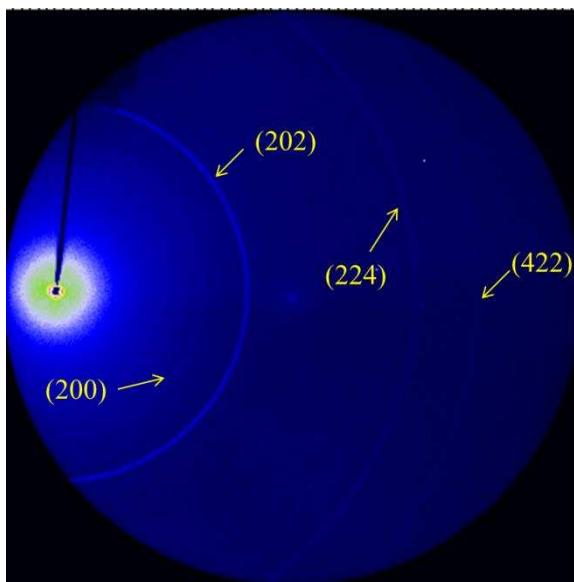


Figure 3.19 A sample of Debye-Scherrer ring that collected from CHESS B1 station.

### 3.4 *In-situ* DAC-Raman spectroscopy

Raman spectroscopy is a widely used technique for studying structures of materials and solid surfaces as it is sensitive to vibrational modes which are either not observed via IR or give rise to only weak IR absorption bands. This technique is applicable to small areas of a sample surface since it uses laser as the excitation source. A schematic diagram of a typical Raman experiment is given in Figure 3.20. Unlike CHESS B1 station, where synchrotron radiation comes horizontally, the specific beam path allows the laser to come vertically. Thus, it allows the DAC to stand in a regular way, which makes it easy to operate gas-membrane type DAC for both high pressure and high temperature measurements. In addition, the size of the hole in the stainless steel gasket in DAC changes under pressure, due to how densely the powder samples are loaded. If the samples are not densely packed, the hole may shrink a lot at high pressure. The beam size of Raman spectroscopy is about several microns. Thus, even the hole size shrinks

under pressure, Raman spectroscopy is still able to measure the pure sample instead of detecting the gasket as well.

The *in-situ* DAC-Raman spectroscopy measurement in the present study used a gas-membrane type DAC (Diacell HeliosDAC A59000, EasyLab Technologies Ltd., Berkshire, UK) combined with an Alpha 300R Confocal Raman microscope (WiTec Instruments Corp., Knoxville, TN, USA) with a doubled Nd: YAG green laser operating at 532 nm. The objective used for all experiments was an Olympus SLMPLN 20X (Olympus, Center Valley, PA, USA) with a 25 mm working distance. Experimental setups for high temperature and pressure tests are much more complicated than for high pressure only. The detail of experimental design for measurement at high temperature and pressure is described in Figure 3.21. N<sub>2</sub> was used to apply pressure on the gas-membrane, and 2% H<sub>2</sub> provided reducing atmosphere that prevent the interior of the cell from vanishing. A K-type thermocouple is inserted into the cell and placed right next to the sample. These setups currently work well at temperatures below 200 °C. The cell itself is not able to hold the temperature very stable for temperatures above 200 °C. In addition, the heat brings very high background to Raman signals.

### **3.5 Rietveld refinement**

Rietveld refinement has been shown to be a powerful tool to model x-ray diffraction data and gather sufficient structural information [199], [200]. The general procedure is to apply known equations to the diffraction profile, and then refine individual parameters until the best fit is achieved. Rietveld refinement is applicable to suitable radiation, e.g., conventional X-ray, synchrotron X-ray or neutron. It is essential that the powder diffraction data be collected appropriately in order to get reliable refinement results. An appropriate data-collection strategy will depend on how well the sample scatters, how quickly the pattern degrades, peak-broadening

effects and the degree of peak overlap. At least five steps across the top of each peak should be included, and the time per step should approximately compensate for the gradual decline in intensity with  $2\theta$  [201], [202].  $2\theta$  range should be chosen as to give the maximum useful data. The background in a synchrotron experiment tends to be more sensitive to structural disorder and fluctuations than that in a laboratory X-ray experiment, due to the excellent signal-to-noise discrimination that is routinely obtained with synchrotron radiation. The high resolution allows the background intensities between peaks to be estimated more reliably. Thus, background interpolation and subtraction usually yield good starts for the following procedures.

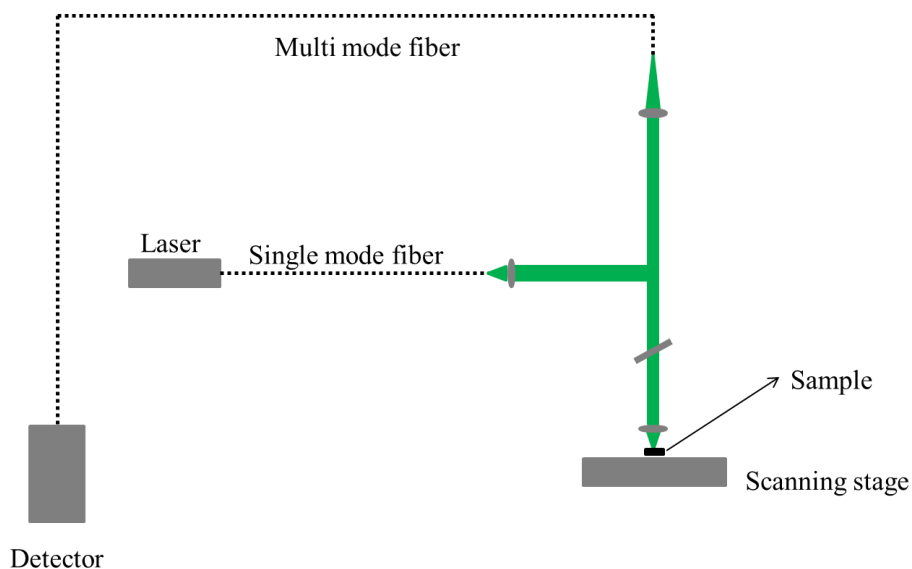


Figure 3.20 Schematic showing the beam path for Confocal Microscopy in reflection mode.

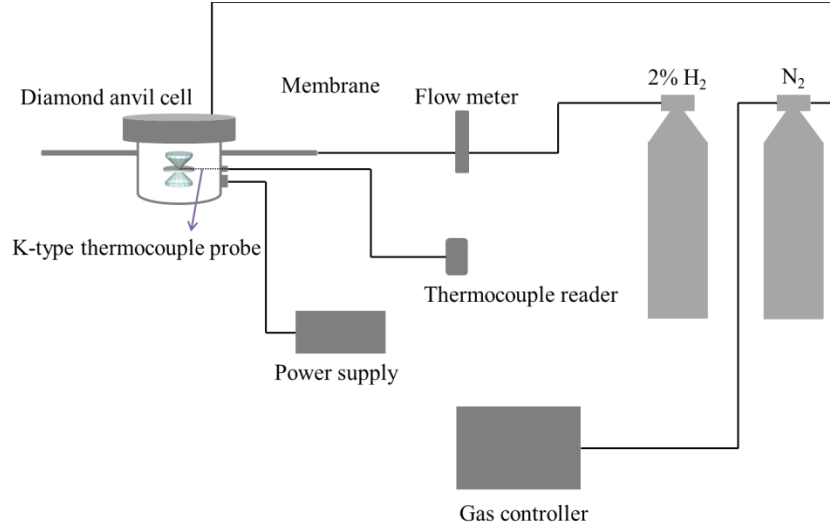


Figure 3.21 A schematic showing the experimental set up for *in situ* DAC-Raman spectroscopy tests at high pressure and temperature.

An accurate description of the shapes of the peaks in a powder pattern is critical to the success of a Rietveld refinement. The peak shapes are a function of both the sample (e.g. domain size, stress/strain, defects) and the instrument (e.g. radiation source, geometry, slit sizes). The analytical peak-shape functions that have been investigated are mainly Lorentzian function, Gaussian function and pseudo-Voigt function. The normalized functions are expressed as:

Normalized Gaussian:

$$G(\theta) = \frac{2}{H_G} \sqrt{\frac{\ln 2}{\pi}} \exp\left(-\frac{4 \ln 2}{H_G^2} \theta^2\right) \quad (3.3)$$

Normalized Lorentzian:

$$L(\theta) = \frac{2}{\left[ \pi H_L \left( 1 + \frac{4}{H_L^2} \theta^2 \right) \right]} \quad (3.4)$$

Pseudo-Voigt:

$$P(\theta) = \eta L(\theta) + (1 - \eta)G(\theta); 0 \leq \theta \leq 1 \quad (3.5)$$

where  $H_G$  is the Caglioti formula [203] to describe the Gaussian peak width and  $H_L$  is the Lorentzian peak width solved by Thompson [204]:

$$H_G^2 = U^2 \tan^2 \theta + V \tan \theta + W \quad (3.6)$$

$$H_L = \frac{X}{\cos \theta} + Y \tan \theta \quad (3.7)$$

The pseudo-Voigt function is probably the most widely accepted, since it is the weight sum of a Gaussian and Lorentzian function with a mixing factor ( $\eta$ ), where  $\eta=0$  is Gaussian and  $\eta=1$  is Lorentzian. Several other terms need to be considered for powder refinement:

SHFT-Sample displacement

TRNS-Sample transparency

ZERO-correction to  $2\theta$  (refine for neutron and synchrotron, not for flat-plate Bragg-Brentano)

Rietveld refinement allows one to refine multiple parameters to optimize the fitting between the experimental data and calculated values to model the crystalline nature of a material. However, in many cases, too many parameters are varied initially, which leads the refinement of various parameters to be physically unrealistic values, though they provide good fits. To avoid this, a guideline has been developed to apply on all the refinements, which progress to parameters of least influence [205]–[207]. In this study, General Structure Analysis System (GSAS) [208], [209] is used for determining lattice parameters of  $\beta$ -eucryptite in different

pressure and temperature conditions. The CIF file can be found in Crystallography Open Database [210]. The atomic positions of pure  $\beta$ -eucryptite are listed in Table 3.4. The refinements of  $\beta$ -eucryptite follow the same sequence: background and scale factor terms for each histogram had converged first; specimen displacement and lattice parameters were added and optimized. Peak profiles were fitted by pseudo-Voigt functions with a peak asymmetry correction. Atomic positions and isotropic temperature factors for Li, Al, Si and O were upon convergence of the above parameters, if necessary [204], [211], [212]. An example of a typical Rietveld full-profile refinement performed using the GSAS program of the X-ray diffraction pattern is shown in Figure 3.22.

Table 3.4 Atomic coordination of  $\beta$ -eucryptite

| name | x      | y      | z      | multiplicity | occupancy | Uiso    |
|------|--------|--------|--------|--------------|-----------|---------|
| Si1  | 0.2502 | 0.0000 | 0.0000 | 6            | 1.0000    | 0.00684 |
| Si2  | 0.2474 | 0.4948 | 0.0000 | 6            | 1.0000    | 0.00925 |
| Al1  | 0.2530 | 0.0000 | 0.5000 | 6            | 1.0000    | 0.00760 |
| Al2  | 0.2503 | 0.5006 | 0.5000 | 6            | 1.0000    | 0.00988 |
| Li1  | 0.0000 | 0.0000 | 0.5000 | 3            | 1.0000    | 0.04053 |
| Li2  | 0.5000 | 0.0000 | 0.0000 | 3            | 1.0000    | 0.03420 |
| Li3  | 0.5000 | 0.0000 | 0.3240 | 6            | 1.0000    | 0.02913 |
| O1   | 0.0870 | 0.1945 | 0.2454 | 12           | 1.0000    | 0.01570 |
| O2   | 0.6035 | 0.7019 | 0.2653 | 12           | 1.0000    | 0.01317 |
| O3   | 0.1061 | 0.7109 | 0.2585 | 12           | 1.0000    | 0.03268 |
| O4   | 0.5924 | 0.2035 | 0.2497 | 12           | 1.0000    | 0.01722 |

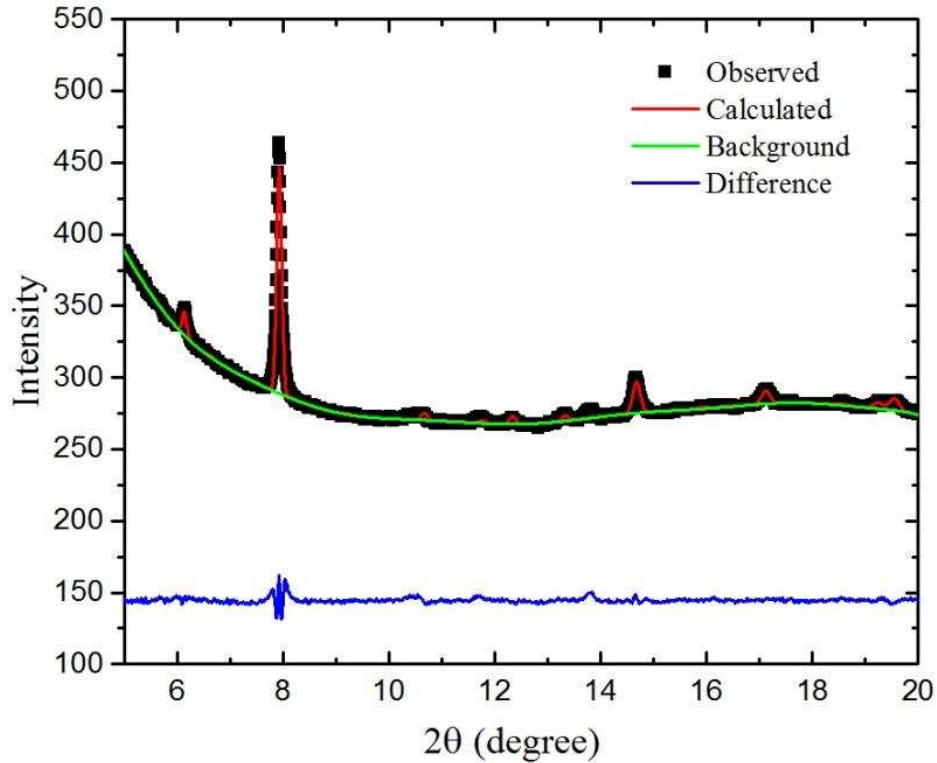


Figure 3.22 Typical Rietveld full-profile refinement performed using the GSAS program of the X-ray diffraction pattern collect for pure  $\beta$ -eucryptite. The black squares, the solid red line and the solid blue line represent an experimental pattern, modeled pattern and the difference between the observed and the refined profile, respectively.

### 3.6 Electrochemical Impedance Spectroscopy technique

Electrochemical impedance spectroscopy has been established as one of the most informative and irreplaceable investigation methods and has been widely used as an empirical quality-control procedure that can be employed to interpret fundamental electrochemical and electronic processes [213]. The impedance technique appears to play an increasingly important role in fundamental and applied electrochemistry and material science.



### 3.6.1 Technique background

Like resistance, impedance demonstrates the ability of a circuit to resist the flow of electrical current and mathematically is the ratio between voltage and current. But unlike pure resistance or capacitance, impedance is a more general concept that takes the phase differences between the input voltage and output current into account [213]. The definition of impedance can be described as a complex resistance encountered when current flows through a circuit composed of various resistors, capacitors, and inductors, and is represented by the terms “real impedance” and “imaginary impedance”. “Real impedance” demonstrates the ability of a circuit to resist the flow of electrical current, and “imaginary impedance” reflects the ability of a circuit to store electrical energy.

Figure 3.23 describes a typical EIS experiment, where material characteristics such as conductivity, resistivity, and permittivity are analyzed. Impedance is applied to both direct current (DC) and alternating current (AC). But in experimental situations, the electrochemical impedance is normally measured using excitation AC voltage signal  $V$  with small amplitude  $V_A$  applied at frequency  $f$  (Hz or 1/s). In a linear system, the current response to a sinusoidal voltage input will be a sinusoid at the same frequency, but have a phase-shift, determined by the ratio of capacitive and resistive components of the output current (Figure 3.24). The voltage  $V(t)$  is expressed as a function of time ( $t$ ):

$$V(t) = V_A \sin(2\pi ft) = V_A \sin(\omega t) \quad (3.8)$$

where  $\omega$  is related to the applied AC frequency  $f$  as  $\omega=2\pi f$ . The response current signal  $I(t)$  is then shifted in phase ( $\phi$ ) and has an amplitude  $I_A$ , that described as:

$$I(t) = I_A \sin(\omega t + \phi) \quad (3.9)$$

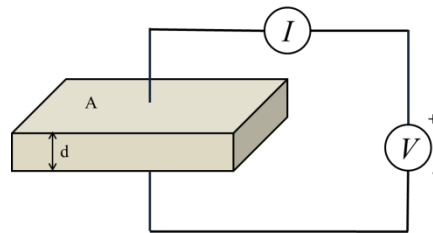


Figure 3.23 Fundamental impedance experiment

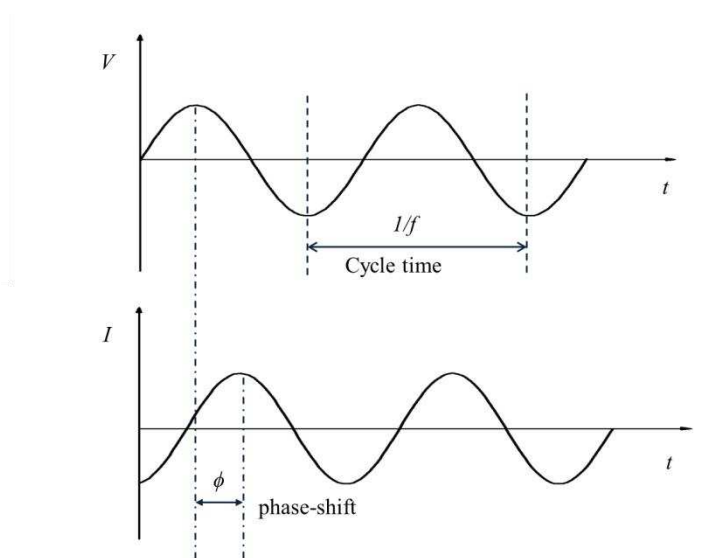


Figure 3.24 Sinusoidal voltage input  $V$  at a single frequency  $f$  and current response  $I$

The complex impedance of the system ( $Z^*$ ) follows Ohm's Law:

$$Z^* = \frac{V(t)}{I(t)} = \frac{V_A \sin(\omega t)}{I_A \sin(\omega t + \phi)} = Z_A \frac{\sin(\omega t)}{\sin(\omega t + \phi)} \quad (3.10)$$

The impedance is therefore expressed in terms of a magnitude (absolute value),  $Z_A=|Z|$ , and a phase shift,  $\phi$ . By applying Euler's relationship:

$$\exp(j\phi) = \cos\phi + j\sin\phi \quad (3.11)$$

where  $j$  represents the imaginary number ( $j = \sqrt{-1}$ ) the impedance can be expressed as a complex function:

$$V(t) = V_A e^{j\omega t} \quad (3.12)$$

and

$$I(t) = I_A e^{j\omega t - j\phi} \quad (3.13)$$

The impedance is then mathematically expressed as a combination of “real” or in-phase ( $Z_{real}$ ), and “imaginary” or out-of-phase ( $Z_{imag}$ ) parts (Figure 3.25):

$$Z^* = \frac{V}{I} = Z_A e^{j\phi} = Z_A (\cos\phi + j\sin\phi) = Z_{real} + jZ_{imag} \quad (3.14)$$

and the phase angle  $\phi$  can be written as:

$$\tan \phi = \frac{Z_{imag}}{Z_{real}} \text{ or } \phi = \arctan\left(\frac{Z_{imag}}{Z_{real}}\right) \quad (3.15)$$

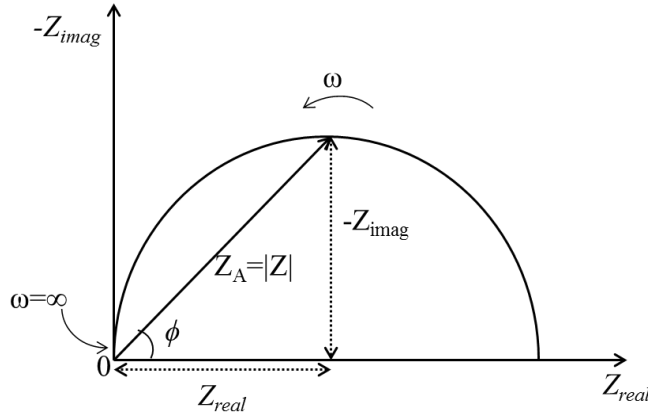


Figure 3.25 Complex impedance plot

### 3.6.2 Brick Layer Model

The materials used in EIS are usually imperfect, thus not acting like an ideal capacitor. A constant phase element (CPE) is used to model the behavior of the imperfect dielectrics, which is defined as:

$$Z_{CPE} = \frac{1}{Q_0 \omega^n} e^{-\frac{\pi}{2}ni} \quad (3.16)$$

$Z_{CPE}$  is the impedance, where  $Q_0$  and  $n$  ( $0 < n < 1$ ) are frequency independent parameters [214], and the response is purely capacitive when  $n=1$  [215]–[218]. Therefore, capacitors were replaced with CPE to model the impedance nonlinearity.

The samples we have used in our experiments are compressed powders. Unlike single crystal, polycrystalline pellets normally have grain boundary effects. The general way to calculate the effect of grain boundaries is to use the brick-layer model (BLM). The BLM can be described as a 3-D array of cubes (grain/bulk) with uniform grain boundary layers separating them [219], where the grains have a side length  $D$  and the grain boundaries a thickness  $d$  ( $d \ll D$ ).

Only half of each grain boundary belongs to a given grain. The fraction of the total volume composed of grain boundaries is then  $3d/D$  [220]. There are basically two possible paths for current to flow through (shown in Figure 3.26): (1) across the grain and then across one of the grain boundaries, and (2) along the grain boundaries [220], [221].

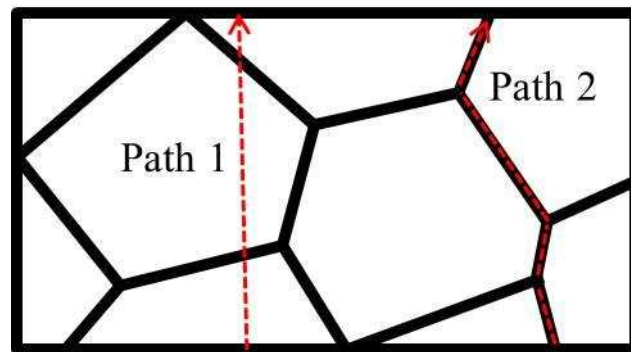


Figure 3.26 Schematic shows the two path ways for conduction. Path 1 represents the case that conduction in grain bulk is much higher than in grain boundary. Path 2 indicates the case when conduction along grain boundary is much higher than in grain bulk.

There are two possible cases when considering the value of conductivity for both bulk and grain boundary:

- (a) If the conductivity of the bulk is much greater than that of the grain boundaries:

In this case, the current will primarily flow through the grain interiors and across the grain boundaries, and then conduct through the next grain interior (Path 1 in Figure 3.26). The equivalent circuit can be described as two parallel RC circuits connected in series (Figure 3.27), since both the grain interior and grain boundary act like an independent layer of materials. Since the case is for when grain interior conductivity is much higher than grain boundary conductivity,

the time constant (RC) for bulk is much lower than that of the grain boundary. Thus, the semi-circle occurring at high-frequency range corresponds to the bulk conduction, and the semi-circle at the low frequency range corresponds to the grain boundary conduction.

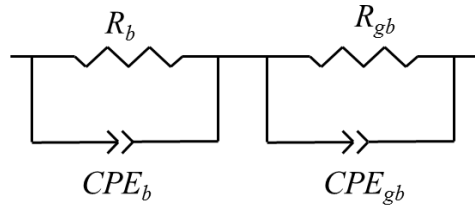


Figure 3.27 The equivalent circuit for current conducted through the bulk and grain boundary.

(b). If the conductivity of the grain interior is much less than that of the grain boundaries:

The current will primarily flow through the grain boundaries only (Path 2 in Figure 3.26). In this case, the separate sides (boundaries) act in parallel; so the equivalent circuit is described as two parallel RC circuits connected in parallel, which can be further reduced to one parallel RC circuit (Figure 3.28). Thus, in the rare cases when grain boundary conductivity is greater than grain interior, only one semi-circle can be collected from EIS.

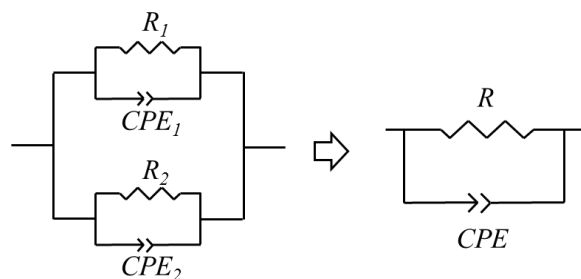


Figure 3.28 The equivalent circuit and its reduced form for current conducted along the grain boundaries only.

### 3.6.3 Experimental setup

The samples used for the ionic conductivity measurements were cut with a diamond saw to obtain the dimensions of about  $1 \times 1 \times 0.1 \text{ cm}^3$  and polished on the surfaces to be contacted. Silver mesh and gold wire were attached to the pellet surfaces using platinum as a current collector. Electrochemical impedance spectroscopy (EIS) of  $\beta$ -eucryptite was performed with a two-probe method using Solartron with a signal amplitude of 10 mV under open circuit voltage (OCV) conditions in the temperature range of 300 °C to 900 °C with the frequency from 1 Hz to 6 MHz. A thermal couple was placed next to the sample in the tube. Data analysis was carried out with software Zview. The experimental setup is shown in Figure 3.29.

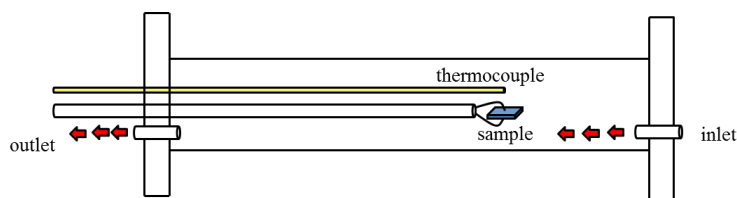


Figure 3.29 Schematic of experimental setup for electrochemical impedance spectroscopy tests.

## CHAPTER 4

### PRESSURE-INDUCED PHASE TRANSFORMATION IN $\beta$ -EUCRYPTITE: AN X-RAY DIFFRACTION AND DENSITY FUNCTIONAL THEORY STUDY

A paper published in Scripta Materialia [104]

Yachao Chen, Sukriti Manna, Badri Narayanan, Zhongwu Wang, Ivar E. Reimanis,

Cristian V. Ciobanu

#### 4.1 Abstract

Certain Li alumino-silicates display exotic properties due to their framework structure made of tetrahedral rigid units. Using *in situ* diamond anvil cell (DAC) x-ray diffraction (XRD), we study the pressure-induced phase transformation of  $\beta$ -eucryptite, a prototypical alumino-silicate.  $\beta$ -eucryptite undergoes a phase transformation at moderate pressures, but the atomic structure of new phase has not yet been reported. Based on density functional theory stability studies and Rietveld analysis of XRD patterns, we find that the pressure-stabilized phase belongs to the  $Pna2_1$  space group. Furthermore, we discover two other possible pressure-stabilized polymorphs,  $P1c1$  and  $Pca2_1$ .

#### 4.2 Introduction

The crystal structure of  $\beta$ -eucryptite (space group  $P6_422$  or  $P6_222$ ) [10], [27], [28], [30], [33], [123] may be described as a stuffed derivative of  $\beta$ -quartz [9], [24], [25]. Like other open crystal structures with low or negative CTE's,  $\beta$ -eucryptite structure also collapses under sufficient hydrostatic pressures, resulting in phase transformation to another crystal structure or amorphization [10]–[13]. Morosin *et al.* [15] were the first to report the pressure-induced transformation in  $\beta$ -eucryptite at around 0.8GPa. Interestingly, Morosin reported the persistence of the high pressure phase under ambient conditions. Zhang, et al. [12], [13] later reported the



existence of the high pressure polymorph above about 0.8GPa and showed that it reverted to  $\beta$ -eucryptite upon unloading, indicating the transformation is reversible. They proposed an orthorhombic crystal system for the high pressure phase, which they named  $\epsilon$ -eucryptite, but crystallographic details such as the space group remain unknown. Reimanis et al. [18][57] observed a unique phenomenon in composites of  $\beta$ -eucryptite and lithium aluminate ( $\text{LiAl}_5\text{O}_8$ ): the material responded to the indentation by ejecting multiple particles with sizes ranging from sub-micrometer to tens of micrometers in diameter for a time period up to several minutes. The behavior was attributed to two mechanisms: (1) the energetic release of residual stresses arising due to the large CTE anisotropy and (2) a reversible phase transformation involving a 7.7 % volume change [14], [16], [19], [56], [57]. More recent in situ indentation experiments under Raman spectroscopy revealed that the critical pressure for the forward ( $\beta$  to  $\epsilon$ ) transformation is higher than that for the reverse [14], indicating that it may be possible to produce metastable  $\epsilon$ -eucryptite under ambient conditions. Finally, nanoindentation experiments at various loading rates were used to show that forward transformation is thermally activated and that the activation volume for the transformation is about equal to the volume of a tetrahedral unit [16], indicating that the transformation is likely controlled by the movement of the individual tetrahedra. They further showed that  $\beta$ -eucryptite begins to amorphize at pressures above about 5GPa, but retains a structural memory, whereby upon unloading to ambient from pressures below 17GPa,  $\beta$ -eucryptite re-forms [13]. Structural memory has been observed in other ceramics and has been attributed to the persistence of specific tetrahedral units [222]. In  $\beta$ -eucryptite, it has been shown that  $[\text{SiO}_4]^{4-}$  tetrahedra persist while  $[\text{AlO}_4]^{5-}$  tetrahedra decompose under either applied hydrostatic pressure [223] or under irradiation [224], and therefore the subsequent structural

memory that arises in both cases is probably connected to the positioning of the  $[\text{SiO}_4]^{4-}$  tetrahedra.

While there is no doubt about the existence of the phase transformation in  $\beta$ -eucryptite under pressure, the atomic structure of the  $\varepsilon$ -eucryptite remains unknown. The crystal system, lattice constants, and Miller indices associated with the  $\varepsilon$ -eucryptite diffraction peaks reported by Zhang *et al.* [12] have not been reproduced by other groups. Here, we have carried out x-ray diffraction (XRD) experiments and density functional theory (DFT) calculations in order to elucidate the atomic structure of  $\varepsilon$ -eucryptite. We have found that there are several polymorphs that become more stable than the  $\beta$ -eucryptite upon increasing pressure. From these, we have determined that the best match for the experimental XRD patterns is achieved by an orthorhombic  $\text{Pna}2_1$  structure. Furthermore, we have found that the presence of dopants leads to two phases (different than  $\beta$ ) coexisting past the transition pressure.

### 4.3 Experimental Method

#### 4.3.1 Materials preparation

The production of  $\beta$ -eucryptite powders through sol-gel route has been developed in literature [126]–[128], [225]. A modified chemical precursor synthesis was carried in this study [17], [42]. An aqueous nitrate solution was prepared by mixing equal molar ratio of aluminum nitrate ( $\text{Al}(\text{NO}_3)_3 \cdot 9\text{H}_2\text{O}$  – Sigma-Aldrich, St. Louis, MO, USA) and lithium nitrate ( $\text{LiNO}_3$  – Sigma-Aldrich, St. Louis, MO, USA). Then, a measured volume of tetraethylorthosilicate (TEOS – Sigma-Aldrich, St. Louis, MO, USA) was added to an equal volume of ethanol (95%) and half volume of distilled water. With a few drops of  $\text{HNO}_3$  added to the solution, the pH value of the solution was adjusted to about 0.5-1. The solution became clear after a few minutes of stirring at room temperature. A homogeneous solution was obtained by blending aqueous nitrate solution

and TEOS solution together after about 30 minutes of mixing using a magnetic stirrer. Ammonia hydroxide was added to the solution and then dried at about 80°C to form amorphous powders. The powders were calcined at 1100°C for 18 hours to form pure single  $\beta$ -eucryptite, then followed by a ball milling process to decrease the particle size till around 1  $\mu\text{m}$ .

#### 4.3.2 Diamond anvil cell (DAC) set up

A schematic description of experimental setup is shown in Figure 4.1. Two gem-quality diamond anvils with culet sizes of 500  $\mu\text{m}$  were aligned and assembled into a DAC for pressurizing the samples [226]. A stainless steel gasket placed in between the upper and lower diamond was pre-indented to a thickness of 100  $\mu\text{m}$ , and a hole of 200  $\mu\text{m}$  was drilled through the gasket to serve as sample chamber [226]. The deposition of sample powders was carried under a microscopy with  $\times 40$  magnification. Several cycles of drop-casting procedures were applied to ensure sufficient powders in the chamber [226]. Micron-sized ruby crystals were introduced on the top of the samples as a pressure reference. A few drops of 16:3:1 methanol-ethanol-water were added as pressure medium, which could maintain hydrostatic pressures up to  $\sim 10.5$  GPa [187]. Finally, the other diamond anvil was used to cover the sample for pressurization.

The pressure was monitored by changes in the ruby fluorescence [157] via  $P(\text{GPa})=0.274(\lambda-\lambda_0)$ , where  $\lambda(\text{\AA})$  is the ruby wavelength being detected and  $\lambda_0(\text{\AA})=6942.1$   $\text{\AA}$  is the ruby wavelength at ambient pressure [158]. As evidenced by the lack of band splitting in ruby fluorescence, shear was absent in the sample so all experiments were carried out in hydrostatic conditions. Pressures were kept below 5 GPa so as to prevent amorphization [12].

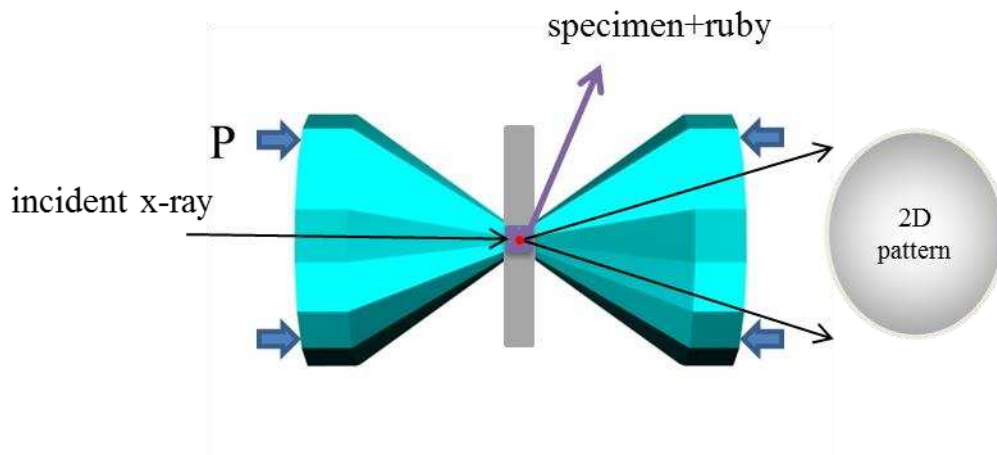


Figure 4.1 Schematic description of experimental set up for high pressure DAC-x-ray diffraction tests.

The conditions in the sample are likely to be isotropic, given a large number of particles: for a volume of about  $3 \times 10^6 \mu\text{m}^3$ , at  $1 \mu\text{m}$  average particle size means that there are  $10^7$  particles in the hole. In addition, there is no significant shear stress applied, as evidenced by the lack of ruby fluorescence band splitting [155], [160]. Thus, all the measurements could be considered under hydrostatic condition within the pressure range explored in this study.

#### 4.3.3 X-ray Diffraction

In-situ XRD experiments were conducted using an angle-dispersive synchrotron source at B2 station of Cornell High Energy Synchrotron Source (CHESS) [227]. Incident X-rays were converted by a double-bouncing Ge (111) monochromator at a wavelength of  $0.48596 \text{ \AA}$ , which was parallel to the uniaxial compression direction. The beam was cut down to  $100 \mu\text{m}$  in diameter for irradiating the samples. While the cell was exposed to x-ray for 20 min, the scattered signals from the sample were collected using a large area MAR345 detector; these

original 2D images were subsequently integrated into x-ray diffraction patterns using the Fit2D software package [197], [198].

#### 4.4 Results and discussions

Incident X-rays were converted by a double-bouncing monochromator at a wavelength of  $\lambda=0.48596\text{\AA}$ . Our data [Figure 4.2 (a)] shows that at an ambient pressure only the  $\beta$ -eucryptite is present, which has a dominant peak [Figure 4.2 (b)] corresponding to the (202) planes. Above a threshold pressure, this peak changes shape as shown in Figure 4.2 (c): new, smaller peaks appear at that pressure and are marked by black dots on the 2.47 GPa curve in Figure 4.2 (a). By fitting the complex peak shape at 2.47 GPa [Figure 4.2 (c)] with Lorentzian functions, the three peak locations have been identified - one corresponding to  $\beta$ , and the other two corresponding to the new phase(s). A small increase in pressure past 2.47 GPa leads to the disappearance of the main  $\beta$  peak, while the intensity of the other two peaks increases [Figure 4.2 (d)]. Thus, for the Mg-doped samples analyzed, the transition occurs between 2.47 GPa and 2.83 GPa, with the  $\beta$ -eucryptite absent past 2.83 GPa; pure samples exhibit somewhat smaller transition pressures.

We now focus on searching for crystalline phases that can become more stable than  $\beta$  upon pressure loading, and hence could be the product of the pressure-induced phase transformation of  $\beta$ . To this end, we have analyzed over thirty structures made of corner sharing  $\text{AlO}_4$  and  $\text{SiO}_4$  tetrahedra such that any Al-centered tetrahedron is surrounded by four Si-centered tetrahedra, and vice versa. These structures have been obtained in two ways: (a) by creating Li-stuffed derivatives of known  $\text{SiO}_2$  structures, similar to the way in which  $\beta$ -eucryptite is related to  $\beta$ -quartz; and (b) by converting the alkaline atom M (M=Li, Na, K) of known  $\text{MAISiO}_4$  and  $\text{MAlGeO}_4$  structures [228] into Li, and Ge into Si when necessary. All structures have been relaxed using DFT in the generalized gradient approximation (GGA) [229], [230], for

each pressure from 0 to 5 GPa in increments of 0.5 GPa. After eliminating duplicates, the crystals that we identified as having a higher density than the  $\beta$  and low heat of formation are shown in Figure 4.3, with the space group and density at zero pressure identified;  $\beta$  is included as a reference. The higher-density phases also have lower symmetry, as expected from the symmetry hierarchy of crystal systems [65]. Two of the three new phases are orthorhombic, with space groups No. 33 ( $Pna2_1$ ) and 29 ( $Pca2_1$ ); the remaining phase is monoclinic (No. 77,  $P1c1$ ).

Next, we discuss the relative stability of these phases with respect to  $\beta$ . In Figure 4.4, we plot the difference between the enthalpy of each candidate phase and that of  $\beta$ , per unit formula. Interestingly, past a certain pressure, each of these phases becomes more stable than  $\beta$ -eucryptite (Figure 4.4); for these pressure-stabilized phases, the lattice parameters are given in, and the atomic positions are given in 4.7. Furthermore, all threshold pressure fall between 2 GPa and 3 GPa (Figure 4.4), in good agreement with the experimental assessment of the range of pressures required for transition (Figure 4.2). We cannot expect a more quantitative agreement because of the uncertainties related to the indirect pressure measurements in the DAC, and of the approximations made in the DFT calculations (for example, the enthalpies are computed at 0 K and not at room temperature). In order to identify more precisely the phases to which  $\beta$  transitions upon loading, we examine the XRD patterns at high pressures.

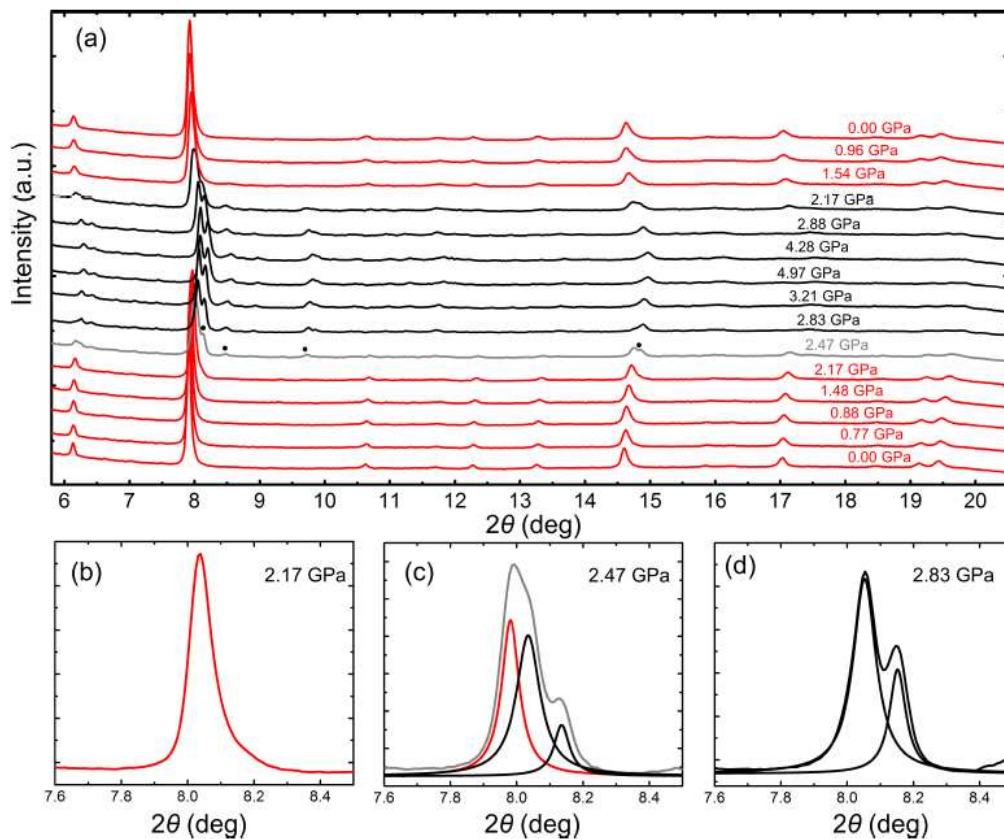


Figure 4.2 XRD patterns showing the pressure-induced phase transformation in  $\beta$ -eucryptite. (a) Variation of the pattern with pressure in a loading-unloading cycle. The patterns that contain the new phase(s) are shown in black, while the  $\beta$ -eucryptite is red. (b)-(d) Detail views of the main peak at three pressures around the transition, showing the main peaks (b) before, (c) during, and (d) after the transition.

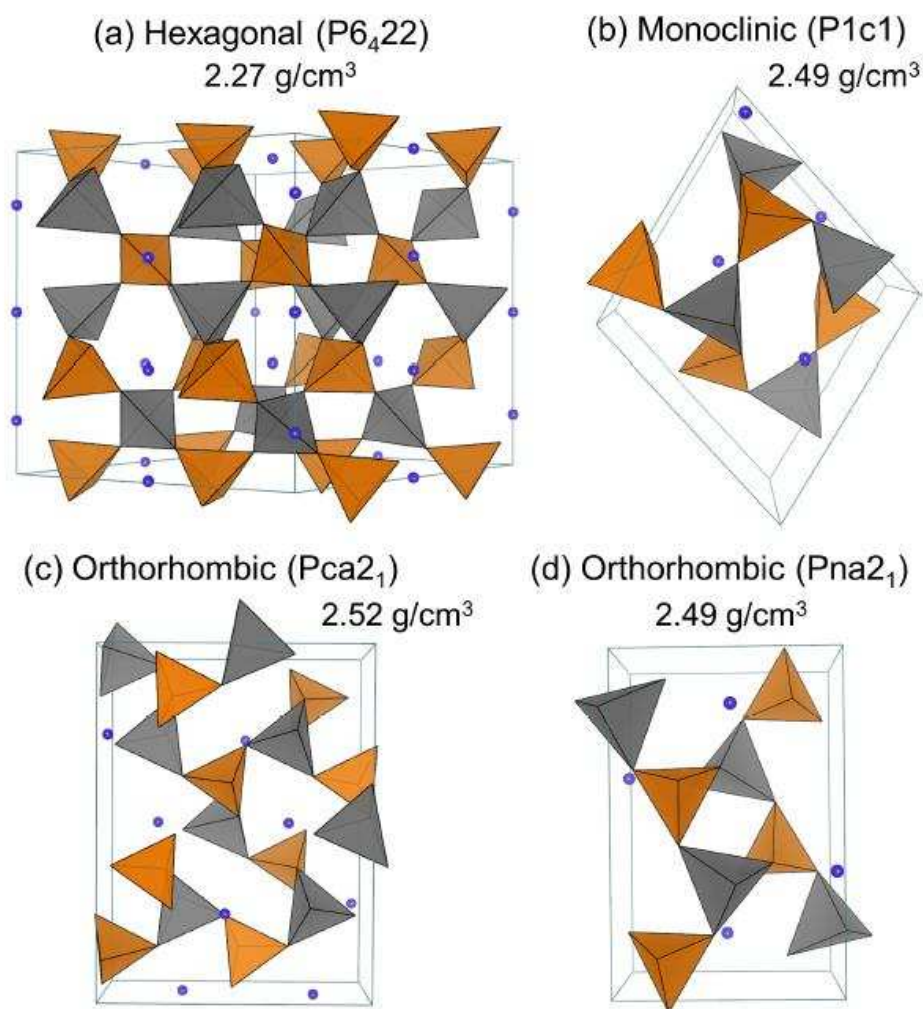


Figure 4.3 Crystal structures of (a)  $\beta$ -eucryptite and (b)-(d) three denser polymorphs and their densities at zero pressure. Al-(Si)-centered tetrahedra are shown in grey (tan), Li atoms are purple spheres.

We have performed Rietveld analysis of the XRD data using MAUD software [231], designed to refine the background, structural (atomic coordinates, occupancies, lattice parameters and angles), and microstructural (particle size, lattice strain, residual stress, texture, etc) parameters via a least-squares method [232]. As input, we have supplied the XRD pattern and a candidate structure with its atomic coordinates and symmetry group. The optimization



proceeds with fitting the background and the peak shape; the shape of the peaks was assumed to be of asymmetric, pseudo-Voigt form so it can fit crystal size and strain broadening of the experimental profiles [233]. Without refining the fractional atomic coordinates and thermal vibration parameters, the following parameters have been optimized: background coefficients, scale, lattice parameters, zero-shift error, and peak shape parameters. The procedure yields a simulated optimized spectrum for comparison with the experimental data. We have carried out this procedure for each of the candidate structures [Figure 4.3 (b)-(d)]. The best fit for the XRD pattern of the pure, undoped sample is the Pna2<sub>1</sub> structure, shown in Figure 4.2(a) for an XRD pattern at ~5 GPa.

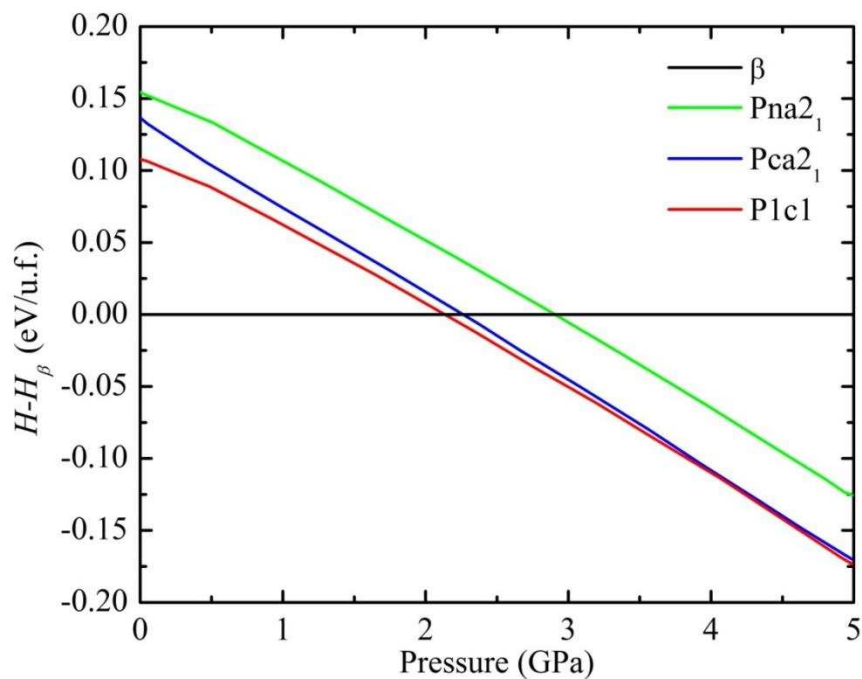


Figure 4.4 Pressure-dependent enthalpy of LiAlSiO<sub>4</sub> polymorphs, with respect to the  $\beta$ -eucryptite.

Table 4.1 Lattice parameters and angles for the crystal structures shown in Figure 4.3 computed at zero pressure using GGA.

| Phase             | a (Å)  | b (Å)  | c (Å)  | $\alpha(^{\circ})$ | $\beta(^{\circ})$ | $\gamma(^{\circ})$ |
|-------------------|--------|--------|--------|--------------------|-------------------|--------------------|
| $\beta$           | 10.575 | 10.575 | 11.391 | 90.000             | 90.000            | 120.000            |
| P1c1              | 8.200  | 8.288  | 5.147  | 90.000             | 90.000            | 106.290            |
| Pca2 <sub>1</sub> | 10.079 | 5.033  | 13.114 | 90.000             | 90.000            | 90.000             |
| Pna2 <sub>1</sub> | 10.082 | 6.673  | 4.990  | 90.000             | 90.000            | 90.000             |

It is worthwhile to compare this result with the previous reports on the phase transformations of  $\beta$ -eucryptite. Morosin *et al.* observed a phase transformation around 0.8 GPa, and interpreted it as a hexagonal phase with lattice constants commensurate with half of those of  $\beta$ . [15] The structure of our monoclinic P1c1 phase is stabilized at the lowest pressure (Figure 4.4) and is somewhat close to being hexagonal (a and c are within 1.1% of each other, and the angle between them  $\sim 12\%$  away from  $120^{\circ}$ ), so it is reasonable to infer that this phase may actually be the one found by Morosin *et al.* [15] Zhang *et al.* reported a reversible transformation around 1.5 GPa to  $\varepsilon$ -eucryptite: [12] although these authors conclude that the  $\varepsilon$ -eucryptite is orthorhombic, its space group and the atomic structure have not been reported so far. Our data also indicates that  $\varepsilon$ -eucryptite is orthorhombic, but with different lattice constants; in addition, we report here the space group (No.33, Pna2<sub>1</sub>) and the atomic structure [Figure 4.3 (e) and 4.7]. The previous indexing [12] is not consistent with the reflection conditions for most orthorhombic groups [234]. On the other hand, the planes that we have found in our XRD pattern [indexed in Figure 4.2 (a)] obey the reflection conditions for group No. 33, and are largely the same as those encountered in other materials with the space group Pna2<sub>1</sub> [235], [236].

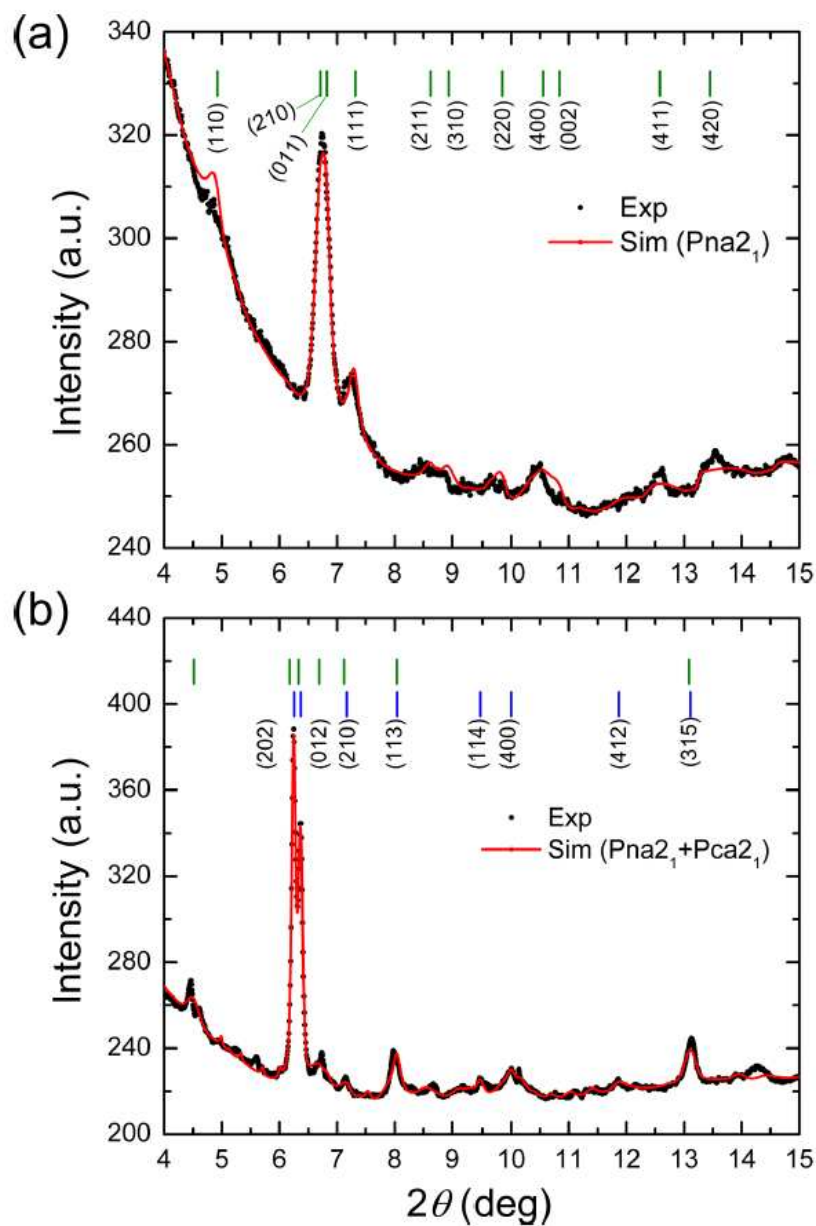


Figure 4.5(a) XRD pattern for the pure  $\beta$ -eucryptite at 5 GPa, compared with the optimized simulated pattern for the  $Pna2_1$  phase; the other polymorphs have significant deviations from the experimental pattern. (b) XRD pattern of the Mg-doped  $\beta$ -eucryptite at 5 GPa, compared with simulations of an optimized mixture of  $Pna2_1$  and  $Pca2_1$ . For clarity, only the Miller indices corresponding to  $Pca2_1$  peaks are shown in panel (b).

We have also analysed XRD data of 0.3 mol% Mg-doped samples such as those in Figure 4.5, and have found that no single phase gives a satisfactory fit to the XRD data. Therefore, we are led to assume that in the presence of Mg, there can be two or more phases present at high pressures. We have analyzed phase mixtures using MAUD for all possible combinations of the XRD pattern of the Mg-doped eucryptite at 5 GPa [shown in Figure 4.2 (b)] is obtained from a mixture of 45.3% (by volume) Pna2<sub>1</sub> and 54.7% Pca2<sub>1</sub>. It is rather intriguing that the presence of Mg in very small amounts facilitates the occurrence of more than one crystalline phase upon pressure loading, which may be due to entropic (mixing) or kinetic factors.

#### **4.5 Conclusions**

We have used XRD measurements and DFT calculations to elucidate the structure of pressure-stabilized  $\epsilon$ -eucryptite. While this answers a long-standing question, deeper investigations are necessary to understand how to control the presence of different polymorphs at low and moderate pressures. The reversible nature  $\beta$ - $\epsilon$  transition, coupled with moderate values of the transition pressure (2-3 GPa) and of volume change (~9%), make it suitable for transformation toughening of ceramic composites for various applications. Knowledge of the  $\epsilon$ -eucryptite can enable a better control over the design of such composites (e.g., optimizing the particle size, and distribution of  $\beta$ -eucryptite particles to be employed in a suitable matrix). Furthermore, we have found that the presence of small amounts of dopants facilitates the coexistence of distinct polymorphs under pressure, which may lead to novel properties displayed by such phase mixtures.

## 4.6 Acknowledgement

We gratefully acknowledge the support of U.S. Department of Energy's Office of Basic Energy Sciences through Grant No. DE-FG02-07ER46397 and that of the National Science Foundation for CHESS under Grant No. DMR-1332208.

## 4.7 Supplemental material

### 4.7.1 Crystal structures for the pressure-stabilized polymorphs

We present here the atomic structures of the polymorphs shown in Fig. 2(b)-(d) of the main text, and the variation of their lattice constants as functions of pressure.

#### **1. Coordinates at zero GPa from DFT calculations.**

We have used the FINSYM utility (<http://stokes.byu.edu/iso/findsym.php>) to extract the symmetry-irreducible fragments from our VASP output coordinate files (CONTCAR files, which are available upon request): we give here the resulting .cif files for the three new polymorphs, at 0 GPa, reported in the main text:

#### **P1c1**

# CIF file

# This file was generated by FINDSYM

# Harold T. Stokes, Branton J. Campbell, Dorian M. Hatch

# Brigham Young University, Provo, Utah, USA

data\_findsym-output

\_audit\_creation\_method FINDSYM

\_symmetry\_space\_group\_name\_H-M "P 1 c 1"

\_symmetry\_Int\_Tables\_number 7

\_cell\_length\_a 8.20013

\_cell\_length\_b 5.14684

\_cell\_length\_c 8.28825

\_cell\_angle\_alpha 90.00000

\_cell\_angle\_beta 106.28957

\_cell\_angle\_gamma 90.00000

loop\_

\_space\_group\_symop\_id

\_space\_group\_symop\_operation\_xyz

1 x,y,z

2 x,-y,z+1/2

loop\_

\_atom\_site\_label

\_atom\_site\_type\_symbol

\_atom\_site\_symmetry\_multiplicity

\_atom\_site\_Wyckoff\_label

\_atom\_site\_fract\_x

\_atom\_site\_fract\_y

\_atom\_site\_fract\_z

\_atom\_site\_occupancy

Si1 Si 2 a 0.49381 0.32894 0.75669 1.00000  
Si2 Si 2 a -0.01188 0.17323 0.09260 1.00000  
Al1 Al 2 a 0.36778 0.83089 0.87745 1.00000  
Al2 Al 2 a 0.86623 0.67757 0.21821 1.00000  
Li1 Li 2 a 0.25931 0.34536 0.00905 1.00000  
Li2 Li 2 a 0.73277 0.16848 0.31771 1.00000  
O1 O 2 a 0.18013 0.20846 0.21678 1.00000  
O2 O 2 a 0.01544 0.27815 -0.08521 1.00000  
O3 O 2 a 0.41870 0.16594 0.89177 1.00000  
O4 O 2 a 0.35691 0.69193 0.06851 1.00000  
O5 O 2 a 0.85405 0.34638 0.16439 1.00000  
O6 O 2 a -0.08867 0.12314 0.56345 1.00000  
O7 O 2 a 0.51941 0.36150 0.31090 1.00000  
O8 O 2 a 0.67503 0.79676 0.25068 1.00000

**Pca2<sub>1</sub>**

# CIF file

# This file was generated by FINDSYM

# Harold T. Stokes, Branton J. Campbell, Dorian M. Hatch

# Brigham Young University, Provo, Utah, USA

data\_findsym-output

\_audit\_creation\_method FINDSYM

\_symmetry\_space\_group\_name\_H-M "P c a 21"

\_symmetry\_Int\_Tables\_number 29

\_cell\_length\_a 10.07850

\_cell\_length\_b 5.03261

\_cell\_length\_c 13.11393

\_cell\_angle\_alpha 90.00000

\_cell\_angle\_beta 90.00000

\_cell\_angle\_gamma 90.00000

loop\_

\_space\_group\_symop\_id

\_space\_group\_symop\_operation\_xyz

1 x,y,z

2 -x,-y,z+1/2

3 -x+1/2,y,z+1/2

4 x+1/2,-y,z

loop\_

\_atom\_site\_label

\_atom\_site\_type\_symbol



\_atom\_site\_symmetry\_multiplicity  
\_atom\_site\_Wyckoff\_label  
\_atom\_site\_fract\_x  
\_atom\_site\_fract\_y  
\_atom\_site\_fract\_z  
\_atom\_site\_occupancy  
Li1 Li 4 a 0.29232 0.44740 0.49877 1.00000  
Li2 Li 4 a 0.03865 -0.06957 0.24548 1.00000  
Al1 Al 4 a 0.78725 0.55377 0.75099 1.00000  
Al2 Al 4 a 0.03517 0.08672 0.49674 1.00000  
Si1 Si 4 a 0.28453 -0.04928 0.37277 1.00000  
Si2 Si 4 a 0.46298 0.57665 0.12468 1.00000  
O1 O 4 a 0.30444 0.51921 0.13923 1.00000  
O2 O 4 a 0.51667 0.41552 0.02390 1.00000  
O3 O 4 a 0.27649 0.09950 0.77200 1.00000  
O4 O 4 a 0.50464 0.10633 0.60834 1.00000  
O5 O 4 a 0.74292 0.37032 0.86173 1.00000  
O6 O 4 a 0.04584 0.53213 0.22425 1.00000  
O7 O 4 a 0.44422 0.00926 0.38587 1.00000  
O8 O 4 a 0.79205 -0.07595 -0.02774 1.00000

**Pna2<sub>1</sub>**

# CIF file

# This file was generated by FINDSYM

# Harold T. Stokes, Branton J. Campbell, Dorian M. Hatch

# Brigham Young University, Provo, Utah, USA

data\_findsym-output

\_audit\_creation\_method FINDSYM

\_symmetry\_space\_group\_name\_H-M "P n a 21"

\_symmetry\_Int\_Tables\_number 33

\_cell\_length\_a 10.08168

\_cell\_length\_b 6.67316

\_cell\_length\_c 4.99043

\_cell\_angle\_alpha 90.00000

\_cell\_angle\_beta 90.00000

\_cell\_angle\_gamma 90.00000

loop\_

\_space\_group\_symop\_id

\_space\_group\_symop\_operation\_xyz

1 x,y,z

2 -x,-y,z+1/2

3 -x+1/2,y+1/2,z+1/2

4 x+1/2,-y+1/2,z

```

loop_
  _atom_site_label
  _atom_site_type_symbol
  _atom_site_symmetry_multiplicity
  _atom_site_Wyckoff_label
  _atom_site_fract_x
  _atom_site_fract_y
  _atom_site_fract_z
  _atom_site_occupancy
Li1 Li 4 a 0.64890 0.48513 0.74516 1.00000
Al1 Al 4 a 0.32821 0.01414 0.24838 1.00000
Si1 Si 4 a 0.40613 0.77773 0.74915 1.00000
O1 O 4 a 0.83014 0.53721 0.59610 1.00000
O2 O 4 a 0.37678 0.79557 0.07262 1.00000
O3 O 4 a 0.43389 0.22498 0.19071 1.00000
O4 O 4 a 0.16302 0.06846 0.14351 1.00000

```

## 2. Variations of the lattice constants with pressure

For the P1c1 structure with the cif file given above, we now interchange the lattice parameter labels  $b$  and  $c$  in Table 1 of the main text and in the graph below so as to show it as a quasi-hexagonal structure. ( $a \sim b$ ,  $\gamma \sim 120$  deg).

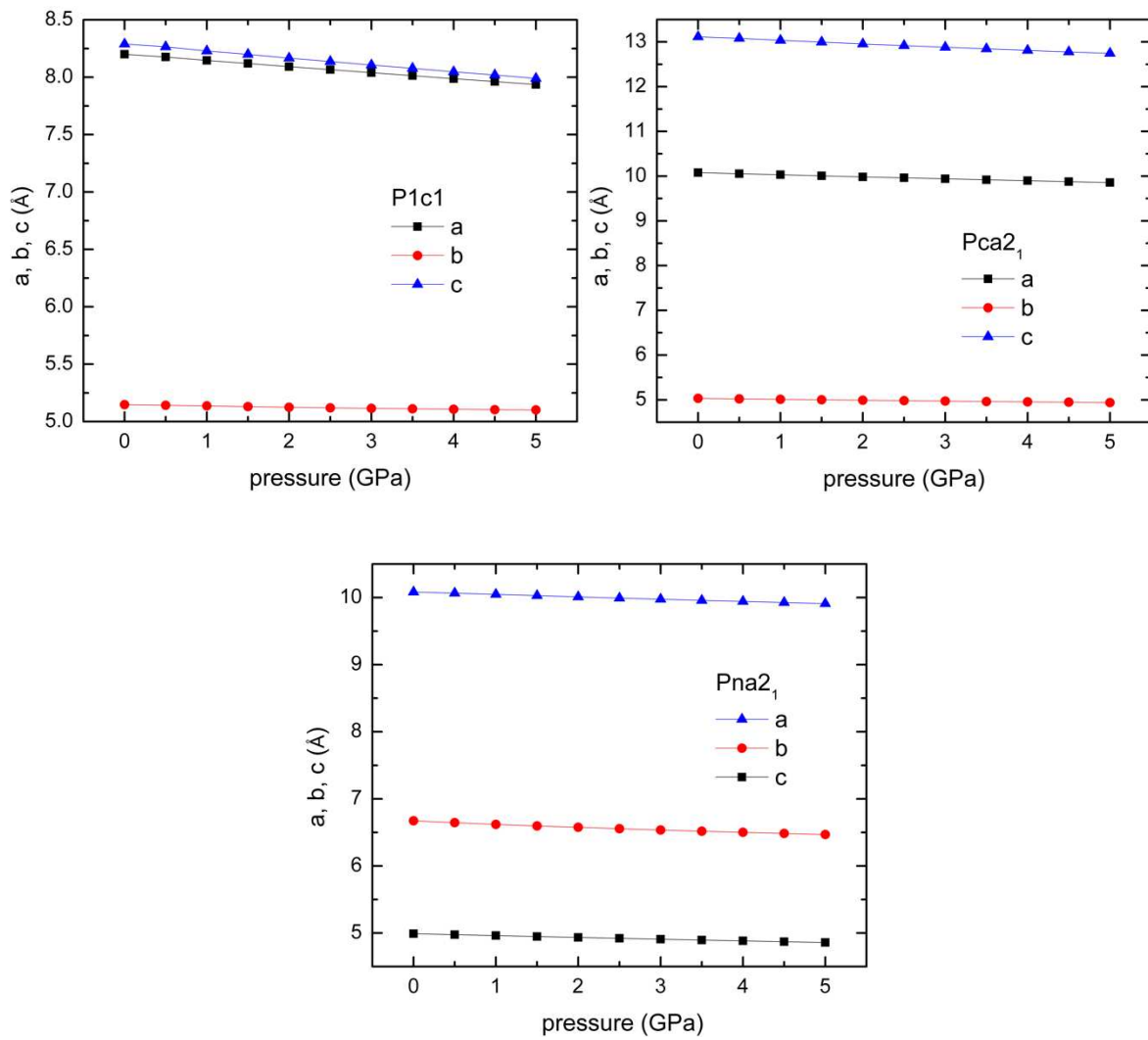


Figure 4.6 Lattice constants of P1c1, Pca2<sub>1</sub> and Pna2<sub>1</sub> as a function of pressure.

## CHAPTER 5

### GRAIN SIZE EFFECT ON THE PRESSURE INDUCED PHASE TRANSFORMATION OF $\beta$ -EUCRYPTITE

A paper to be submitted to the Journal of the American Ceramic Society [237]

Yachao Chen, Zhongwu Wang, Cristian V. Ciobanu, Ivar E. Reimanis

#### 5.1 Abstract

*In-situ* diamond anvil cell (DAC)-x-ray diffraction experiments have been performed on  $\beta$ -eucryptite partially sintered powders with different grain sizes (0.1  $\mu\text{m}$  to 5  $\mu\text{m}$ ) up to 5 GPa, with the goal to establish the thermodynamic driving force for the reversible pressure-induced phase transformation to  $\varepsilon$ -eucryptite. Within the size range of 0.1  $\mu\text{m}$  to about 0.5  $\mu\text{m}$ , the transformation pressure depends linearly with the reciprocal of grain size. It is shown that the transformation is described with a classic nucleation model that includes the combined effect of strain energy, shear strain, microcracking, and twinning.

#### 5.2 Introduction

Martensitic phase transformations in ceramics are of interest for a variety of applications, including transformation toughening [21], [84], [85], [103], [238]–[240], transformation plasticity [241]–[243], and shape memory ceramics [244]–[246]. By far, the largest number of studies have been performed on  $\text{ZrO}_2$ , in the context of transformation toughening where decades of research and development focused mainly on microstructure design have led to ceramics that display fracture toughnesses greater than 15  $\text{MPa}\cdot\text{m}^{1/2}$  [20], [84], [87], [247]. There exist numerous other ceramic systems that exhibit martensitic transformations but are less studied than  $\text{ZrO}_2$  [102], [104], [240], [248]–[250]. Martensitic phase transformations are activated by changes in temperature and stress, and they proceed in a way described well with a classical

nucleation and growth model in which the total free energy of the system is expressed as the sum of various energy terms, including the change in the bulk (chemical) free energy, the transformation strain energy, the interaction energy under an applied stress, and the surface energy [20], [22], [77], [82], [251]. It is well-known that the resulting dependence of the critical grain size on the temperature or pressure emerges from the presence of a nucleation barrier. In a number of ZrO<sub>2</sub> systems, the theoretically predicted linear dependence of the inverse critical grain size with temperature has been experimentally observed. However, there are relatively few studies in which the effect of pressure on the critical grain is systematically examined [69]–[71], [75], [252]–[254]. In the present work, the relation between grain size and the pressure-induced phase transformation from  $\beta$ -eucryptite (LiAlSiO<sub>4</sub>) to  $\varepsilon$ -eucryptite was examined with *in situ* diamond anvil cell studies under x-ray diffraction.

$\beta$ -eucryptite is a prototype lithium aluminum silicate exhibiting unusual behaviors, such as negative coefficient of thermal expansion, one-dimensional Li ionic conductivity and a pressure induced phase transformation [4], [5], [7], [9], [10], [24], [25], [27]–[30], [32], [110], [123], [255]. The crystal structure of  $\beta$ -eucryptite (space group P6<sub>4</sub>22 or P6<sub>2</sub>22) may be visualized as an anisotropic framework with Si/Al centered tetrahedra sharing their corners and arranged in a spiral along the 6<sub>4</sub> (or 6<sub>2</sub>) screw axis parallel to the c-axis.  $\beta$ -eucryptite undergoes various phase transformations as is well documented by Zhang *et. al.*, [13] including the reversible martensitic phase transformation to  $\varepsilon$ -eucryptite at moderate pressure (~1 GPa).  $\varepsilon$ -eucryptite has an orthorhombic crystal structure with Pna2<sub>1</sub> space group and a 9% volume shrinkage from  $\beta$ -eucryptite [104]. It has been suggested that the reverse transformation ( $\varepsilon$ -eucryptite to  $\beta$ -eucryptite) may be employed for transformation toughening if it were possible to create  $\varepsilon$ -eucryptite metastably under ambient conditions [17].

The conditions for stability of  $\varepsilon$ -eucryptite are not well defined. It has been shown that doping with  $\text{Zn}^{2+}$  or  $\text{Mg}^{2+}$  ions helps to stabilize  $\beta$ -eucryptite [19], [104], implying that doping may not work to form metastable  $\varepsilon$ -eucryptite under ambient conditions, a necessary requirement to activate transformation toughening. However, it is clear from discussions above that the grain size could be a useful parameter by which to create metastable  $\varepsilon$ -eucryptite. This has motivated the present study to determine the critical transformation pressure for various  $\beta$ -eucryptite grain sizes.

### **5.3 Experimental procedure**

#### **5.3.1 Sample preparation**

The production of  $\beta$ -eucryptite powders with various grain sizes used a chemical solution method, which can be viewed as a sol-gel plus a precipitation process [42], [126]–[129]. Hydrolysis occurs when tetraethylorthosilicate (TEOS) and water are mixed in a mutual solvent, generally ethanol [130]. Thus, an equal volume of TEOS (Sigma Aldrich, St. Louis, MO USA) and ethanol (95%) were first mixed in a clean beaker with half the volume of distilled water to achieve an R-factor (water moles/TEOS moles) of about 7 [126], [127]. A certain amount of  $\text{HNO}_3$  (70 wt%) was added to help obtain a clear solution with a pH of about 0.5-1 after a few minutes of stirring at room temperature. The Li and Al metal ions of  $\beta$ -eucryptite were provided by lithium nitrate ( $\text{LiNO}_3$ -Sigma Aldrich, St. Louis, MO USA) and aluminum nitrate ( $(\text{Al}(\text{NO}_3)_3 \cdot 9\text{H}_2\text{O})$ -Sigma Aldrich, St. Louis, MO USA). An aqueous nitrate solution was then obtained by mixing these nitrate precursors and an equal weight of water together with the stoichiometric quantity of the TEOS solution. After about 30 minutes of mixing on a hot plate with a magnetic stirrer at about 50 °C, a homogeneous solution was obtained. An amorphous gel was formed by treating the solution with excess aqueous ammonium hydroxide (~10-15%). After drying at

about 80 °C, the amorphous powders were calcined at 1100 °C and above for different time lengths to obtain pure  $\beta$ -eucryptite but with different grain sizes. The samples used in the x-ray diffraction study are labeled as S1, S2, S3 and S4. The phase purity was confirmed through x-ray diffraction, and grain sizes were characterized through scanning electron microscopy (SEM).

### 5.3.2 X-ray diffraction

*In-situ* DAC-Synchrotron X-ray diffraction experiments, over a pressure range from 0 to 5 GPa, were performed at Cornell High Energy Synchrotron Source (CHESS) on B1 station. The samples were loaded in a Mao-Bell type diamond anvil cell (DAC) with culet sizes of 500  $\mu\text{m}$ . The deformable gaskets placed between the opposing diamond faces were pre-indented and drilled with a 200  $\mu\text{m}$  hole to contain the samples. The deposition of sample powders was carried under a microscopy with  $\times 40$  magnification [226]. Micro-sized ruby crystals were introduced on the top of the samples as a pressure reference. A few drops of 16:3:1 methanol-ethanol-water were added as pressure medium, which could maintain hydrostatic pressure up to  $\sim 10.5$  GPa [187]. X-ray diffraction patterns were collected on a MAR345 image plate detector with the monochromatic beam of  $\lambda = 0.485946$  Å. The sample-to-detector distance and the image plate inclination angles were precisely calibrated using a  $\text{CeO}_2$  standard. The pressures on the samples were added by tightening the screws on the cell. A minimum increment was kept for each step to get the best accuracy of transformation pressures. After each increment, the ruby fluorescence method was used to measure the pressure on the samples, and the cell was then exposed under x-ray for 20 mins to get a clear diffraction image. Two-dimensional diffraction images were transformed to intensity vs.  $2\theta$  diffractograms through Fit2D software [197], [198].



## 5.4 Results

Selected x-ray diffraction patterns of the four samples with different grain sizes under compressive loading, and their corresponding SEM images are shown in Figure 5.1. At ambient pressure, only  $\beta$ -eucryptite is present in all four samples, and the dominant peak corresponds to the (202) plane. As pressure passes a threshold, a new peak starts to appear next to the (202) peak. With continuously increasing pressure, the other  $\beta$ -eucryptite peaks fade away. The transformation pressure is determined by the appearance of the new peak next to (202). The transformation pressures and the relative grain size values are labeled accordingly.

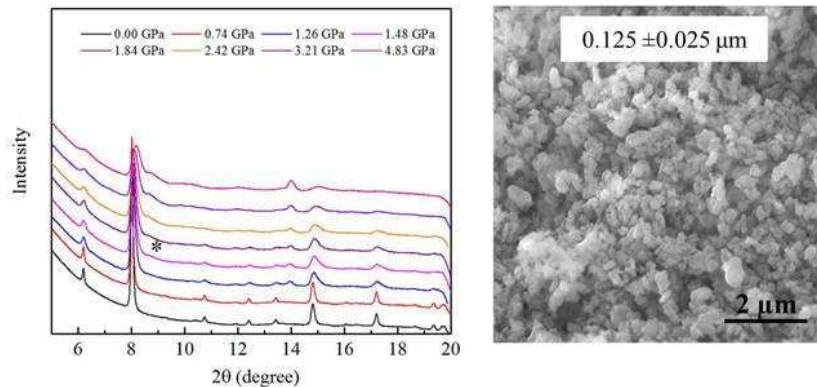


Figure 5.1 X-ray diffraction patterns for different grain size samples and the relative SEM images are shown. The increment has been kept as small as 0.1 GPa from ambient pressure to 5 GPa, thus only selected patterns at certain pressures of each sample are shown here. The grain radii are labeled on the SEM images accordingly. The peak at  $2\theta=14^\circ$  existing in certain patterns indicates the diffraction from the high-pressure-cell metal gasket. S1 was prepared by long time ball milling, which results in fine grains, whereas S2, S3 and S4 were as-calcined samples.

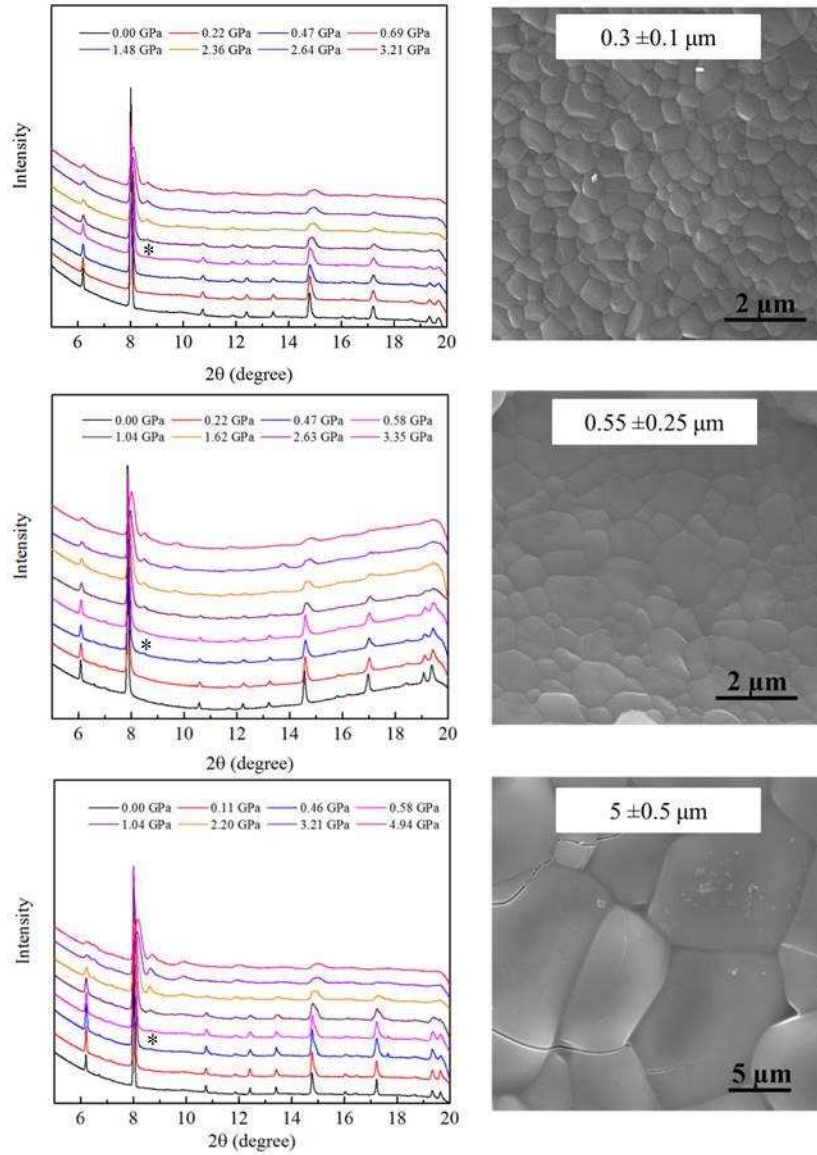


Figure 5.1 Continued

## 5.5 Discussion

In high pressure studies, the barrier to transition is usually explained in terms of nucleation dynamics. The nucleation and growth model has been widely accepted to explain the size effects on phase transformations in CdSe, PbS, ZnS,  $\gamma$ -Fe<sub>2</sub>O<sub>3</sub> and CdS systems [69], [71], [73]–[75], [252], [256]. Table 5.1 summarizes some examples in existing literature that include

material systems, how phase transformation is effected by grain size and the reasons of these effects that have been proposed. Tolbert *et al.* [69], [71], [252] found that the transformation pressure increases with decreasing the grain size in Si, CdSe, CdS nanocrystals. However, Jiang *et al.* [73] reported that the transition pressure for  $\gamma$ -Fe<sub>2</sub>O<sub>3</sub> to  $\alpha$ -Fe<sub>2</sub>O<sub>3</sub> phase transformation is lower for nanocrystals than for bulk material. Thus, the change of the transition pressure affected by grain size is highly depending on the system under investigation.

Table 5.1 Studies on grain size effects on pressure-induced phase transformations

| Author                   | Material   | Grain size effects   | Mechanistic explanation   |
|--------------------------|--|--|---|
| Tolbert [69]–[71]        | CdSe, CdS, Si  | Transformation pressure increases with decreasing grain size.            | The increase in transformation pressure for the nanocrystals is due to the surface energy differences between the phases involved.  |
| Qadri [72]               | PbS  | Transformation pressure increases with decreasing grain size.            | The increase in phase transformation pressure as the particle size decreases is due to an increased surface energy at the solid-solid phase transformation, which impedes the formation of the high pressure phase. |
| Jiang [73]               | $\gamma$ -Fe <sub>2</sub> O <sub>3</sub> ( $\gamma$ - $\alpha$ irreversible) | Transformation pressure is lower in nanophase material than in the bulk. | The transformation barrier of nanophase is smaller than bulk material, which is resulted from the larger volume change upon transformation in nanophase than bulk material.   |
| Qadri [74]<br>Jiang [75] | ZnS  | Transformation pressure increases with decreasing grain size.            | Transformation pressures are controlled by the surface energy of the particles associated with the two phases.  |

If one considers nucleation and growth of  $\epsilon$ -eucryptite from a  $\beta$ -eucryptite grain within the partially sintered powder of  $\beta$ -eucryptite, the total free energy change,  $\Delta G$ , due to the formation of the nucleus may be expressed as [66]–[68]:

$$\Delta G = \Delta G_{bulk} + \Delta G_{interfacial} = N\Delta G_{u.f.} + \eta N^{2/3}\gamma \quad (5.1)$$

where  $\Delta G_{bulk}$  and  $\Delta G_{interfacial}$  are the bulk free energy change and interfacial free energy change from  $\beta$  to  $\varepsilon$ -eucryptite, respectively;  $N$  is the number of unit formulae in a cluster (nucleus) and  $N^{1/3}$  is proportional to  $r$  (nucleus size);  $\Delta G_{u.f.}$  is the bulk free energy difference per unit formula between  $\varepsilon$  and  $\beta$ -eucryptite;  $\eta$  is a shape factor; and  $\gamma$  is the interfacial energy per unit interface area. In the present case, if the new  $\varepsilon$ -eucryptite grain remains bonded to the neighboring  $\beta$ -eucryptite grains, then  $\gamma$  represents the difference between the new  $\beta$ -eucryptite/ $\varepsilon$ -eucryptite interface energy and the original  $\beta$ -eucryptite grain boundary energy; in this case, an additional barrier to nucleation would be present due to the mechanical constraint imposed by the neighboring  $\beta$ -eucryptite. However, with a negative 9% transformation strain, it is likely that the transformation is accompanied by debonding at the interface, in which case  $\gamma$  is represented as

$$\gamma = \gamma_s^\beta + \gamma_s^\varepsilon - \gamma_{gb}^\beta \quad (5.2)$$

where the subscripts  $s$  denote surface energy for the given phase ( $\beta$ - or  $\varepsilon$ -eucryptite) and  $gb$  for the grain boundary energy ( $\beta$ -eucryptite).

Since the entropy change for solid-solid phase transformations is very small compared with the enthalpy change [257]–[260], the entropy change may be ignored, and the bulk free energy change per unit volume associated with the transition can be expressed as:

$$\Delta G_{u.f.} = \Delta H + \Delta G_e \quad (5.3)$$

where  $\Delta H$  is the enthalpy change due to the transition, and  $\Delta G_e$  represents possible energy terms other than enthalpy changes, for example, dilational strain energy, shear strain,

microcracking, and/twinning. The values of critical nucleus size ( $N^*$ ) are obtained from the condition:

$$\frac{\partial \Delta G}{\partial N^*} = 0 \quad (5.4)$$

Thus,

$$N^{*1/3} = -\frac{2\eta\gamma}{3(\Delta H + \Delta G_e)} \quad (5.5)$$

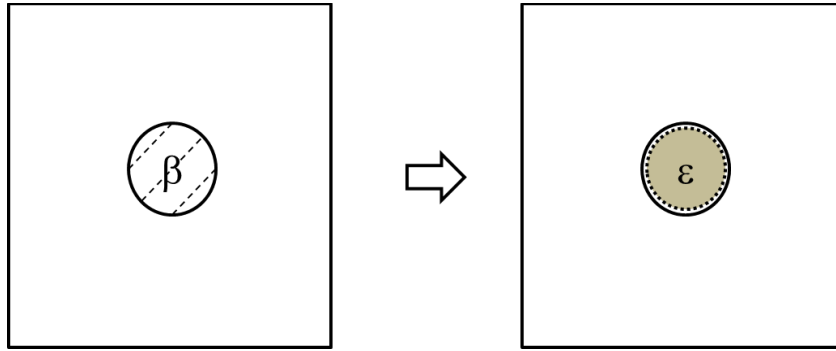


Figure 5.2 Schematic description of a grain before and after phase transformation.

For the phase transformation to proceed,  $\Delta G_{u.f.}$  must be negative since the interfacial energy term in equation (5.1) is positive. While  $\Delta G_e$  is not well defined,  $\Delta H$  has been calculated as a function of pressure with density functional theory (DFT) (Figure 5.3) [104].

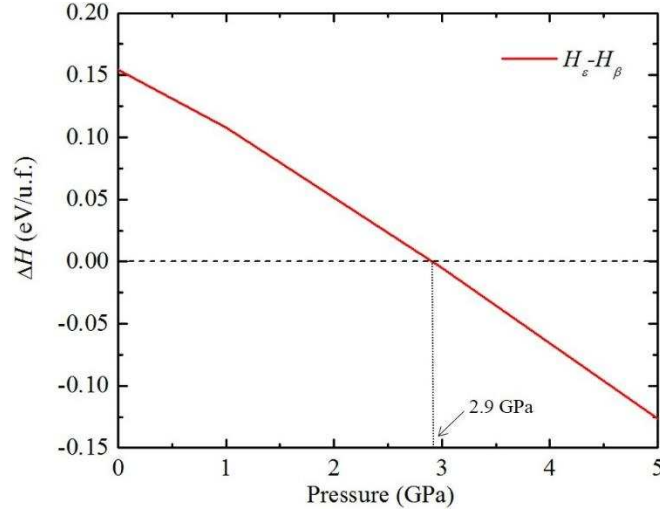


Figure 5.3 The change in enthalpy in going from  $\beta$  to  $\epsilon$ -eucryptite as a function of pressure calculated by DFT is shown.

It is nonetheless possible to make some general conclusions about the value of  $\Delta G_e$ . On the one hand, strain energy represents a barrier to the transformation [68], but on the other, shear strain, microcracking, and twinning are expected to change the stress state, thus, lower the barrier [21], [243]. While the contributions of these microscale processes are difficult to quantify, it is clear that their net effect is to reduce the barrier (negative  $\Delta G_e$ ) since the measured critical pressures (Figure 5.1) fall below the pressure at which  $\Delta H = 0$  (2.9 GPa in Figure 5.3). This reduction in barrier is illustrated in Figure 5.4 where  $\Delta G_{u.f.}$  is plotted as a function of pressure.

For simplicity, it is assumed that  $\Delta G_e$  is not a function of pressure. The pressure where equilibrium  $\beta$  and  $\epsilon$ -eucryptite exist in equilibrium ( $\Delta G_{u.f.} = 0$ ) is denoted as  $P^*$ . Two terms,  $k$  and  $\delta P$ , are introduced to describe the effect of  $\Delta G_e$  on  $\Delta G_{u.f.}$ :  $k$  is the slope of  $\Delta G_{u.f.}$  vs.  $P$  and  $\delta P = P - P^*$ , where  $P$  is the pressure at which the transformation occurs, dependent on the grain size. Analogous with the case of undercooling for thermally activated phase transformations [67], [68], the present model (Figure 5.4) suggests that overloading is necessary for the transformation to

proceed. The energy associated with the driving force in this overloaded system is  $k\delta P$ . Thus, equation (5.5) may be re-written as

$$N^{*1/3} = -\frac{2\eta\gamma}{3(k\delta P)} \quad (5.6)$$

where  $k$  is given by the slope of  $\Delta H$  versus  $P$  (Figure 5.3) ( $k = -0.0566$  eV/GPa) [104], and  $\delta P$  depends on  $\Delta G_e$ .

The number of unit formulae,  $N$ , is related to the grain size,  $r$ , by

$$N = \frac{V_{grain} \times 12}{V_{unit\ cell}} = \frac{4/3\pi r^3 \times 12}{V_{unit\ cell}} \quad (5.7)$$

where  $V_{grain}$  is the volume of one grain, here assumed to be perfectly spherical, and  $V_{unit\ cell}$  is the volume of a single unit cell ( $V_{unit\ cell} = 1064 \text{ \AA}^3$ ); each unit cell of  $\beta$ -eucryptite has 12 unit formulae [25]. The grain radii, expressed as  $N^{-1/3}$  and  $r$ , are plotted as a function of the measured transformation pressure in Figure 5.5. The increment of pressure for each sample was kept as  $\sim 0.1$  GPa, so the error bars of the transformation pressure points are actually within the symbols. The error bars on  $N^{-1/3}$  represent the standard deviation of grain size in each sample.

The linear trend apparent for the smaller grain sizes (S1, S2, and S3) confirms the general applicability of the nucleation and growth model employed here (equation 5.1). This approach is likely valid only for grains below a critical radius, where the entire grain undergoes transformation at the critical pressure and the critical nucleus size equals the grain size. At larger grain sizes, the critical nucleus size is smaller than the grain size, and thus a grain size dependence on pressure would not be expected. While the critical radius below which the model

applies is not known, it is estimated to be approximately 0.5  $\mu\text{m}$  based on the observation that S3 and S4 exhibited approximately the same transformation pressure (Figure 5.5).

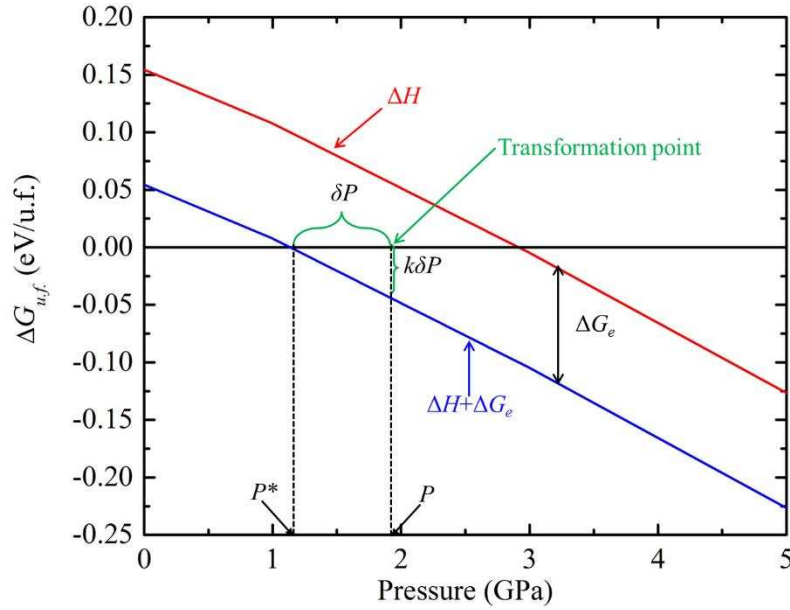


Figure 5.4  $\Delta G_{u.f.}$  as a function of pressure with the existence of  $\Delta G_e$ , where  $\Delta G_e$  includes the influence of dilational strain energy, shear strain and microcracking. The value of  $\Delta G_e$  cannot be fully defined from the present study.  $P$  represents the transformation pressure, and  $P^*$  is the pressure at  $\Delta G_{u.f.}=0$ . Hence,  $\delta P=P-P^*$ , and  $k\delta P$  represents the bulk free energy difference associated with the transformation.

The slope of the curve in Figure 5.5 (only includes S1, S2 and S3) may be used to estimate the interfacial energy (equation (5.7)):

$$\gamma = \frac{3k}{2\eta A} \quad (5.8)$$

where  $A$ , the slope of the curve that describes samples S1, S2, and S3 in Figure 5.5 with a linear fit, is 0.0017. For a spherical nucleus,  $\eta=(36\pi)^{1/3}\Omega^{2/3}$ . Note that equation (5.8) does not



depend on  $\Delta G_e$  which quantifies the combined effect of strain energy, shear strain, microcracking, and twinning. From equation (5.8),  $\gamma$  is calculated to be  $8.5 \pm 3.0 \text{ J/m}^2$ . If one inspects equation (5.2), and realizes that surface energies reported for ceramics generally vary between  $0.01$  and  $10 \text{ J/m}^2$  [261]–[263], the value of  $\gamma$  obtained here appears reasonable. The result is especially noteworthy considering the possible errors accumulated due to the grain size distribution in the specimens and the resolution of the transformation pressure in the experiment, both of which influence the slope  $A$  of the curve in Figure 5.5. Nonetheless, the present analysis indicates that the model applied here sufficiently captures the nucleation and growth of  $\epsilon$ -eucryptite from  $\beta$ -eucryptite.

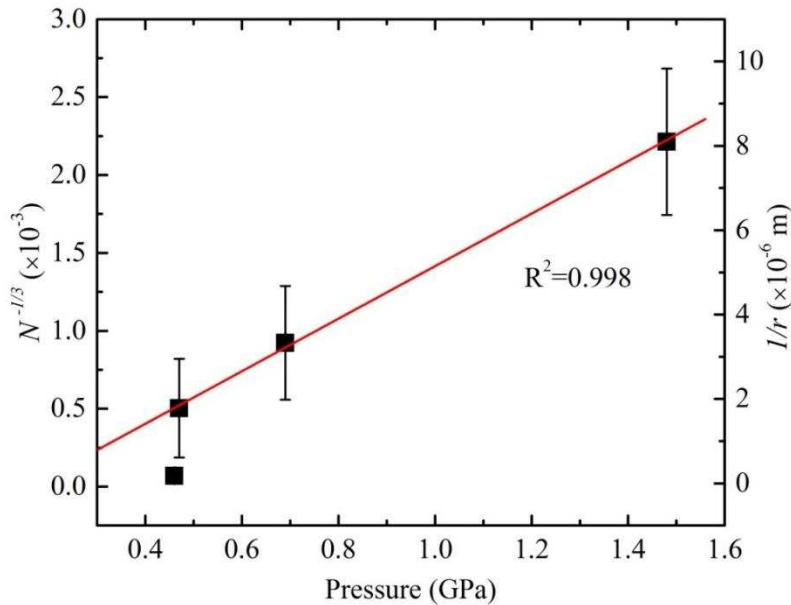


Figure 5.5 Experimental data shows the transformation pressure of each sample that expressed by both number of unit formula  $N$  (left axis) and grain radius  $r$  (right axis). The error bars are associated with the left axis. The red line is the fitting of S1, S2 and S3.

## **5.6 Conclusion**

*In-situ* DAC-X-ray diffraction experiments have been performed to study the relation between grain size and transformation pressure for the transformation of  $\beta$ -eucryptite to  $\varepsilon$ -eucryptite. Transformation pressure increases with decreasing grain size, displaying a linear relation between reciprocal grain size and transformation pressure, described by a nucleation and growth model. Above grain sizes of about 0.5  $\mu\text{m}$ , the transformation is not affected by grain size. Though the effects of dilational strain energy, shear strain, microcracking, and twinning are not known individually known, their combined effect is included in the model.

## **5.7 Acknowledgement**

We gratefully acknowledge the support of U.S. Department of Energy's Office of Basic Energy Sciences through grant no. DE-FG02-07ER46397. CHESS is supported by the NSF and NIH/NIGMS via NSF award DMR-1332208. We appreciate the insightful discussions with Dr. Corinne Packard.

## CHAPTER 6

### THERMAL REGIMES OF LI-ION CONDUCTIVITY OF $\beta$ -EUCRYPTITE

A paper submitted to the Journal of the American Ceramic Society [264]

Yachao Chen, Sukriti Manna, Cristian V. Ciobanu and Ivar E. Reimanis

#### 6.1 Abstract

While it is well established that ionic conduction in lithium aluminosilicates proceeds via hopping of Li ions, the nature of the various hopping-based mechanisms in different temperature regimes has not been fully elucidated. The difficulties associated with investigating the conduction in these materials, which are usually polycrystalline materials. Herein, we investigate the ion conduction mechanisms in  $\beta$ -eucryptite, a prototypical lithium aluminosilicate, using impedance spectroscopy. In the absence of significant structural transitions in grain boundaries, we have found that there are three conduction regimes for the one-dimensional ionic motion along the  $c$  axis channels in the grains, and determined the activation energies for each of these temperature regimes. Activation energies computed from molecular statics calculations of the potential energy landscape encountered by Li ions suggest that at temperatures below 440 °C conduction proceeds via cooperative or correlated motion, in agreement with established literature. Between 440 °C and 500 °C, the activation barriers extracted from EIS measurements are consistent with those computed from atomistic calculations for uncorrelated Li ion hopping. Above 500 °C the activation barriers decrease significantly, which indicates that after the transition to the Li-disordered phase of  $\beta$ -eucryptite, the Li ion motion largely regains the correlated character.

## 6.2 Introduction

As a prototype of lithium aluminum silicates (LAS),  $\beta$ -eucryptite ( $\text{LiAlSiO}_4$ ) has attracted both fundamental and technological interest for decades due to its phase transformation behaviors [10], [13], [104], [125], [223], unusual thermo-mechanical properties [41], [265]–[268], and the one-dimensional nature of its ionic conduction [4], [8], [29], [110], [123]. The superior Li ion conduction makes  $\beta$ -eucryptite a promising candidate for electrolyte applications, including thermal batteries and high-temperature solid electrodes [40], [269], [270]. Furthermore, applications such as electrothermal devices can benefit from the overall negative coefficient of thermal expansion (CTE) of  $\beta$ -eucryptite [16], [32], [40]–[42], [52], [121], [267], [269], [271]. The crystal structure of  $\beta$ -eucryptite (space group  $P6_422$  or  $P6_222$ ) [10], [27], [28], [30], [33], [272] is a Li-stuffed derivative of  $\beta$ -quartz in which half of the Si-centered tetrahedra,  $[\text{SiO}_4]^{4-}$ , are replaced with Al-centered tetrahedral,  $[\text{AlO}_4]^{5-}$  [9], [25]. In ordered  $\beta$ -eucryptite,  $[\text{SiO}_4]^{4-}$  and  $[\text{AlO}_4]^{5-}$  tetrahedra are arranged in a spiral along the  $6_4$  (or  $6_2$ ) screw axis, forming open channels along which the  $\text{Li}^+$  ions reside at well-defined locations [10], [32]. The effect of temperature on this structure consists in disordering of the Li ions at  $\sim 440$  °C [5], [9], [27], [36], [116]–[119], while at very high temperatures disordering of the Si- and Al- centered tetrahedra could also occur [9], [32].

Li motion in the channels is of special interest [267], [273] for applications of eucryptite as an ionic conductor. It has been reported that the Li ionic conductivity parallel to  $c$ -axis is three orders of magnitude greater than that perpendicular to the  $c$ -axis in the temperature range from 200 °C to 600 °C [4], [29], which makes  $\beta$ -eucryptite an excellent example to study one-dimensional diffusion [5], [117], [122]. While such studies have been reported in the literature for different preparations and different temperature regimes [4]–[6], [8], [29], [121]–[124] and

the mechanism of conduction is accepted to be Li ion hopping along the channel, the activation energies associated with this hopping vary significantly. For example, the activation energy below 500 °C has been reported to be 0.89 eV [8], 0.8 eV [121], 0.79 eV [6], 0.74 eV [4], [29], and 0.62 eV [122], with the variations attributed to differences in the measurement or computation techniques, crystallinity, and sample preparations: the variation from 0.62 eV [122] to 0.89 eV [8] is significant, as the same temperature would lead to vastly different conductivity because of the activated nature of Li ion hopping. The presence of channels in the structure of eucryptite may lead one to expect large ionic conductivity and low activation energy. However, the activation energy of  $\beta$ -eucryptite is not particularly small, as illustrated by any of the above figures [4]–[6], [8], [29], [121]–[124]. Two factors may conspire to decrease the ionic conductivity in polycrystalline eucryptite: first, under normal processing conditions, the grains in the microstructure are randomly oriented and therefore their *c*-axis channels are not all parallel to each other; second, grain boundaries likely present an impediment to Li-ion diffusion.

Despite a significant body of work on Li-ion conduction in  $\beta$ -eucryptite [6], [7], [29], [40], [123], [270], particularly on single-crystal and glasses, there remain two key outstanding questions for the polycrystalline material. First, why is there a variation of activation energy over a large temperature range? Such variation may correspond to different mechanisms operating in different thermal regimes, or it may correspond to the (continuous) thermal expansion or contraction of the structure along different directions. Second, what is the role of the conduction through grain boundaries and other slow ion conduction pathways (such as hopping perpendicular to the *c*-axis)? Using electrochemical impedance spectroscopy (EIS) measurements performed at temperatures up to 900 °C and atomistic-based modeling, we address these questions here and show that the thermal expansion/contraction does not play a

significant role in determining the ionic conductivity. We determined the activation energies at different temperatures using a brick layer model, and found that at temperatures below 440 °C conduction proceeds via cooperative or correlated motion, in agreement with established literature. Between 440 °C and 500 °C, the activation barriers extracted from EIS measurements are consistent with those computed from atomistic calculations for uncorrelated Li ion hopping. Above 500 °C the activation barriers obtained from EIS decrease significantly, which indicates that after the transition to the Li-disordered phase of  $\beta$ -eucryptite, the Li ion motion largely regains the correlated character.

### **6.3 Experimental procedure**

Pure  $\beta$ -eucryptite powders were synthesized via a chemical precursor route [42], [126], [127], in which tetraethylorthosilicate (TEOS-Sigma Aldrich, St. Louis, MO USA), aluminum nitrate ( $\text{Al}(\text{NO}_3)_3 \cdot 9\text{H}_2\text{O}$ -Sigma Aldrich), and lithium nitrate ( $\text{LiNO}_3$ -Sigma Aldrich) were used as precursors. Proper amounts of ethanol (95%), distilled water and  $\text{HNO}_3$  were added to help form a homogeneous solution. This solution was then treated with excess ammonium hydroxide (~10-15%) to form gel, which was then dried at 80 °C to obtain amorphous powders. These powders were first heated up to 400 °C and held for 1 hour in order to remove water and gaseous products formed by decomposition of the nitrates, then calcined in air at 1100 °C for 15 hours to form single phase  $\beta$ -eucryptite as confirmed by x-ray diffraction. The crystalline  $\beta$ -eucryptite powders were then ball-milled using  $\text{ZrO}_2$  balls and ethanol to achieve a final particle size of about 1  $\mu\text{m}$  [42]. The powders were subsequently poured into a graphite die, 25 mm in diameter, and sintered in a vacuum hot press at 1200 °C for 2 h under an applied load of 30 MPa, followed by slow cooling (1°C/min) [42]. All pellets were found to have about 97%–98% of the theoretical density (2.34 g/cm<sup>3</sup>) and remained single phase  $\beta$ -eucryptite.

The samples used for the ionic conductivity measurements were cut with a diamond saw to obtain the dimensions of about  $1 \times 1 \times 0.1 \text{ cm}^3$  and were polished on the surfaces to be contacted. Silver mesh and gold wire was attached to the pellet surfaces using platinum as a current collector. Electrochemical impedance spectroscopy (EIS) of  $\beta$ -eucryptite was performed by a two-probe method using Solartron with a signal amplitude of 10 mV under open circuit voltage (OCV) conditions in the temperature range of 300 °C to 900 °C with the frequency from 1 Hz to 6MHz. A thermocouple was placed next to the sample in the tube. Data analysis was performed with software Zview (Scribner Associates, Southern Pines, NC) [274]. A schematic microstructure based on a brick layer model (BLM) [275] are shown in Figure 6.1, which illustrates fast conduction portions (green, conduction parallel to the  $c$  axis) and slow portions (grain boundaries and unfavorably oriented grains) for a given pathway.

#### 6.4 Results and discussion

Impedance spectroscopy coupled with the BLM model for analysis [276] is a technique meant strictly for a “composite” medium with different ionic conductivities for the two isotropic components that make up the sample. For example, the use of this technique for polycrystalline zirconia samples [277], [278], yields the conductivity of both the grains and the grain boundaries. In the case of zirconia, the grains are isotropic or very nearly so. Applying the EIS for highly anisotropic materials such as  $\beta$ -eucryptite poses several problems: (i) the conduction pathways pass through grains that do not all conduct equally well because of how their  $c$  axis is oriented (Figure 6.1 (a)); (ii) grain boundaries are slow conduction avenues, and as such they would act similar to the slow-conducting (i.e., unfavorably oriented) grains. Because of this, the conductivity and the activation barriers obtained from EIS applied to highly anisotropic materials are approximate (or effective), in the sense that the parallel conduction refers to pathways

parallel or nearly parallel to  $c$  axis, and the slow conduction includes both grain boundaries and unfavorably oriented grains. Below we describe our results and analysis in terms of resistances determined from EIS, ionic conductivities, and activation energies for Li conduction processes.

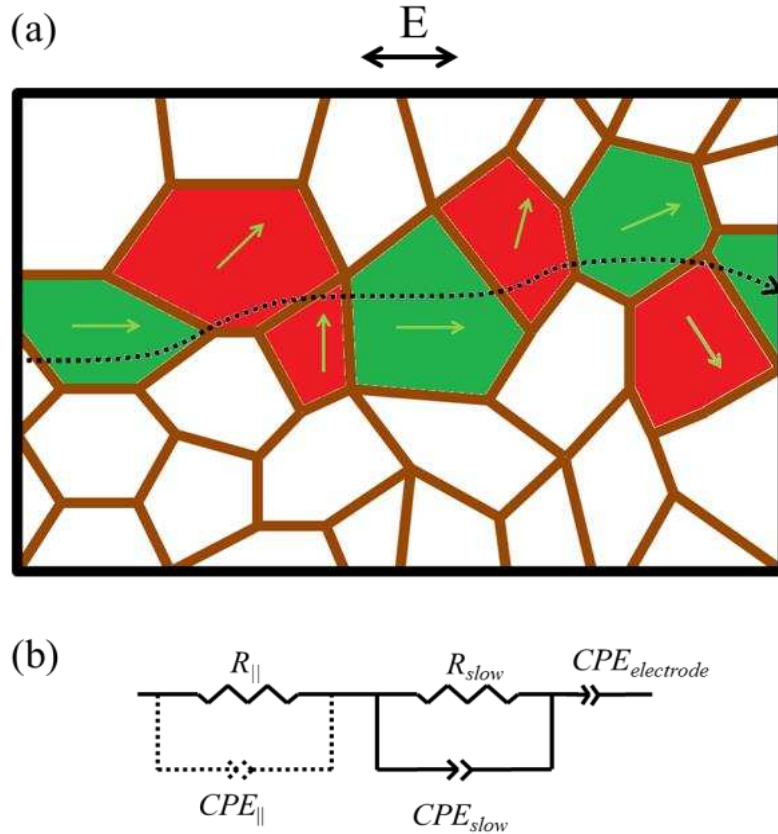


Figure 6.1 (a) Schematic drawing of polycrystalline  $\beta$ -eucryptite, with one current pathway through the structure. The green arrows represent the direction of the  $c$ -axis, whose orientation with respect to the pathway renders some grains fast (green, pathway approximately along the  $c$  axis), and some grains slow (red, orientation not sufficiently aligned with the pathway). (b) Equivalent circuit to interpret complex impedance spectra:  $R_{\parallel}$ , bulk resistance for conduction parallel to the  $c$  axis;  $R_{slow}$  and  $CPE_{slow}$ , resistance and capacitance of the possible slow paths, including grain boundaries and unfavorably oriented grains;  $CPE_{electrode}$ , capacitance of the electrode. The constant-phase element  $CPE_{\parallel}$  is represented as dotted lines since, even when present, it cannot be detected from the experiments.



Figure 6.2 (a) displays several typical impedance spectra of pure  $\beta$ -eucryptite at selected temperatures between 300 °C to 900 °C in Nyquist form, with the imaginary part  $-Z_{imag}$  as a function of the real part  $Z_{real}$ . The analysis of polycrystalline materials is much more complicated than single crystals, because of the presence of grain boundaries. For modeling isotropic materials, the equivalent circuits normally adopt the elements corresponding to bulk (b), grain boundary (gb) and electrode [275], [279], [280]. However, in highly anisotropic materials, such as  $\beta$ -eucryptite, the effect of different grain orientations is not completely captured by the simple equivalent circuits because its grain boundaries and slow conducting grains cannot be readily resolved. In general, the capacitance values per unit length are in the range of  $10^{-11}$  to  $10^{-8}$  F/cm for grain boundary and of the order of  $10^{-12}$  F/cm for bulk [280]. The anisotropy is very large for  $\beta$ -eucryptite, *i.e.* the conductivity along the  $c$ -axis is about a thousand times higher than that perpendicular, but the capacitance associated with both directions should be similar, so the EIS responses of the unfavorably oriented grains overlaps largely with that of the grain boundaries. The simplified equivalent circuit (Figure 6.1 (b)), therefore, adopts two parallel RC circuits connected in series. In Figure 6.1 (b),  $R_{||}$  and  $CPE_{||}$  represent the conduction along the  $c$ -axis in the favorably oriented grains and  $R_{slow}$  and  $CPE_{slow}$  represent the slow paths for Li ions corresponding to arcs in the Nyquist plots for temperature between 300 °C and 440 °C in Figure 6.2. The sample-electrode impedance is represented by a  $CPE$  ( $CPE_{electrode}$ ).

Inspection of the data presented in Figure 6.2 reveals that there are two types of impedance plots, one consisting only of a linear portion (Figure 6.2 (b)), and the other comprising an arc and a linear portion at the low-frequency (Figure 6.2 (c)). Figure 6.2 (b) represents the case when  $R_{slow}$  decreases and becomes comparable with  $R_{||}$  (*e.g.*, temperatures higher than 440 °C), it is only possible to extract total resistance ( $R_t$ ) from the intercept of the

linear portion with the horizontal axis [276], [281]. Figure 6.2 (c) corresponds to the case where the characteristic frequency associated with the Li motion along the  $c$  axis is within the experimentally attainable frequency domains: this corresponds to temperatures from 300 °C to 440 °C, where the Nyquist plots consist of an arc followed by linear spike at lower frequencies. The low-frequency tails in the spectra are due to the blocking effect of the platinum electrode [282]–[284], and they are well described using a constant phase element. The high-frequency end of the arc does not pass through the origin when extrapolated. The non-zero intercept at high frequencies corresponds to the grain bulk resistance for fast conduction (i.e. parallel to the  $c$  axis),  $R_{\parallel}$ . The equivalent circuit is shown as an inset in Figure 6.2 (c). A second resistance,  $R_{slow}$ , that effectively corresponds to grain boundaries and unfavorably oriented grains, is extracted from the length of the horizontal chord of the arc as illustrated in Figure 6.2 (c). The resistance of the contact electrodes is negligible, so  $R_t = R_{\parallel} + R_{slow}$ .

The resistance determined from the Nyquist plots can be used to determine the overall (total) conductivity of the samples using  $\sigma = L/RA$ , where  $A$  is the electrode cross section area and  $L$  is the length of the pellet; for temperatures below 440 °C, we can use length and area estimates to also determine the effective conductivity of the slow paths (grain boundary and unfavorably oriented grains) and that along the  $c$  axis in grains. These conductivity results are plotted in Figure 6.3. The values in Figure 6.3 for the one dimensional conduction are consistent with those reported by Alpen *et al.* [4], [29], and those for the total conductivity are somewhat lower than those of Shin-Ichi *et al* [123].

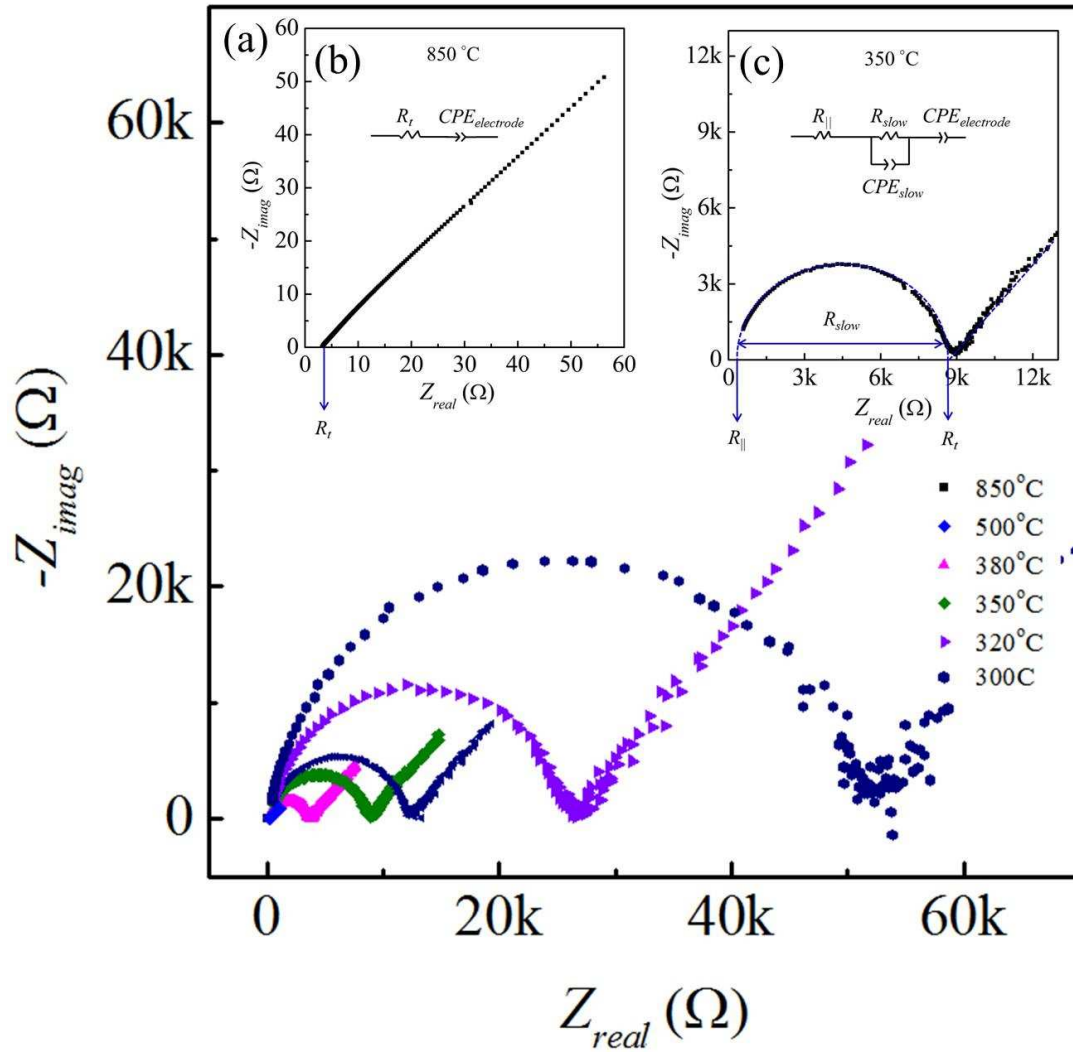


Figure 6.2 (a) Impedance spectra of pure  $\beta$ -eucryptite at selected temperatures from 300 to 900°C. (b, c) Impedance spectra and equivalent circuit at (b) 850 °C and (c) 350 °C.

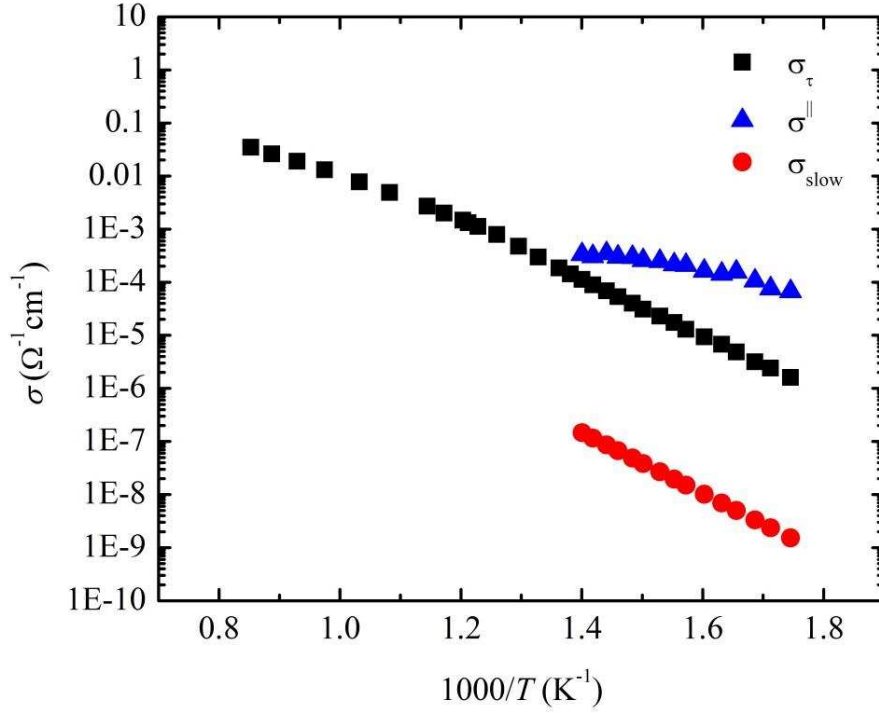


Figure 6.3 Conductivity of total, along the  $c$ -axis grains and slow paths as a function of temperature, respectively.

Next, the activation energies which determine ionic conductivity via the Arrhenius equation are discussed:

$$\sigma T = B \exp\left(-\frac{E_a}{kT}\right) \quad (6.1)$$

in which  $\sigma$  is the conductivity,  $B$  is a pre-exponential constant,  $E_a$  is the activation energy,  $k$  is Boltzmann's constant, and  $T$  is the temperature. This relation holds for the one dimensional bulk conduction along the  $c$  axis. In an effective way, we will adopt this Arrhenius relation for the slow paths as well, since either in the grain boundary or perpendicular to the  $c$  axis the Li ion diffusion is more likely to occur by hopping than by partial attach of Li ions on the Si-O bonds.

Expressing the conductivity in terms of resistance ( $\sigma=L/RA$ ) and taking the natural logarithm of equation 6.1 leads to a linear relation between  $\ln (R/T)$  and  $1/kT$ , with the slope equal activation energy,  $E_a$ :

$$\ln \frac{R}{T} = \ln \left( \frac{L}{BA} \right) + \frac{E_a}{kT} \quad (6.2)$$

The temperature dependence of  $\ln (R/T)$  is shown in Figure 6.4, along with the resulting slopes for different conduction pathways, i.e., the activation barriers for the motion along the  $c$  axis channels and the slow pathways. In processing the data in Figure 6.4, we have assumed that the motion along slow pathways (grain boundaries, and motion across the  $c$  axis channels) remains governed by the same mechanisms and therefore its effective activation energy does not change. We have therefore determined the corresponding activation energy  $E_{slow}$  from EIS data at temperatures below 440 °C, and the used this value to determine the resistance  $R_{slow}$  for all temperatures above 440 °C. From these extrapolated values and the total resistance  $R_t$  (from EIS measurements above 440 °C), we have extracted the one-dimensional (along  $c$  axis) resistance as  $R_{||}=R_t-R_{slow}$  at all the temperatures for which it could not be obtained directly from EIS data. Figure 6.4 distinctly shows three regions for the one-dimensional ionic conductivity, and, by virtue of our initial assumption, one region for the slow conduction along the grain boundaries and across the  $c$ -axis.

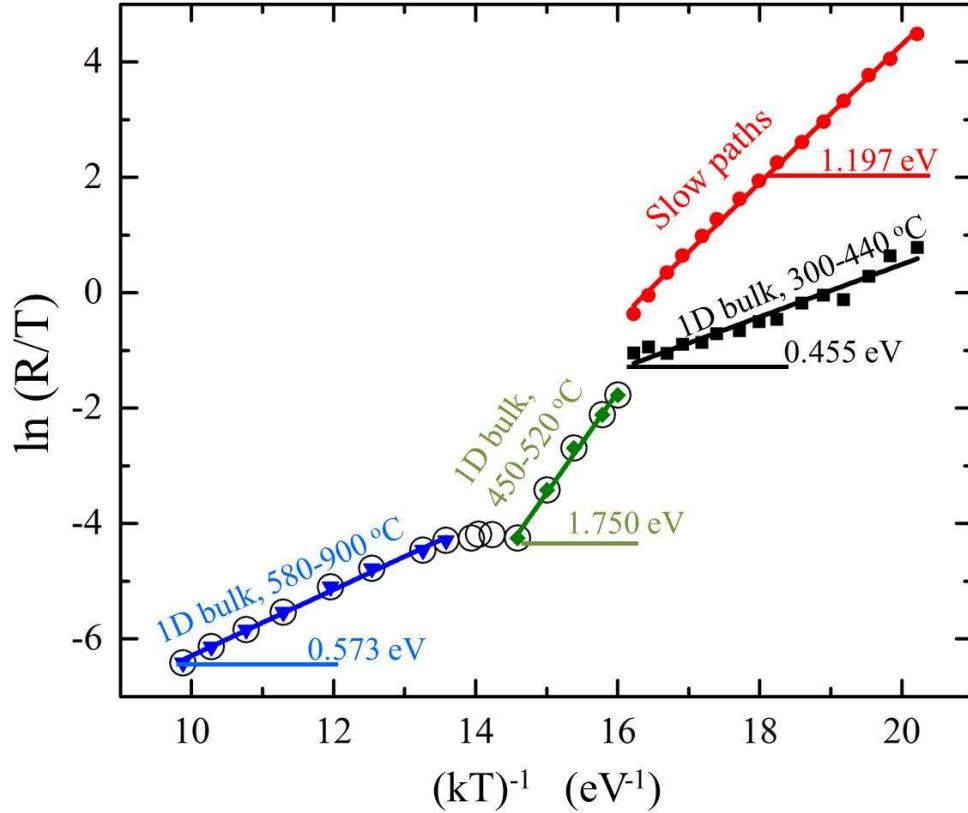


Figure 6.4 Experimental measured  $\ln(R/T)$  as a function of  $1/kT$  for total, paralleled grains and slow paths at low temperatures (solid symbols) combined with calculated values at high temperatures (open symbols).

Table 6.1 Activation energies of the total, bulk, and grain boundary in  $\beta$ -eucryptite, determined from resistance measurements using Arrhenius's law. Above 440 °C, the activation energy is assumed to be 1.197 eV, hence no standard deviation is reported at these temperatures.

| Temperature range (°C) | Activation Energy (eV)    |                  |
|------------------------|---------------------------|------------------|
|                        | <i>Bulk</i> <sup>  </sup> | <i>Slow path</i> |
| 900-500                | 0.573±0.015               | 1.197            |
| 500-440                | 1.75±0.072                | 1.197            |
| 440-300                | 0.455±0.03                | 1.197±0.014      |

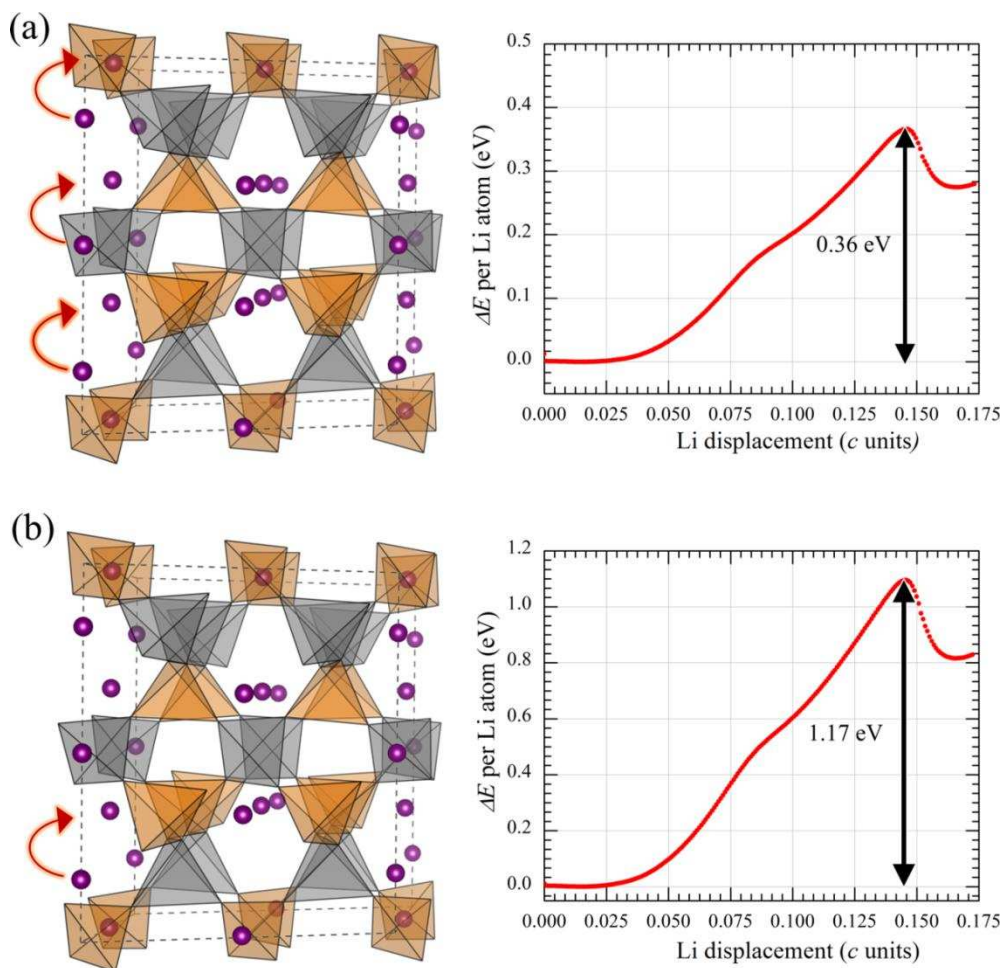


Figure 6.5 Side view of the  $\beta$ -eucryptite structures, with vertical channels in which Li motion can be correlated (a) or uncorrelated (b). Energy variation along the channels and the corresponding activation barrier for moving (a) three Li atoms at a time (correlated), and (b) one Li atom at a time (uncorrelated).

The physical origin of the different regimes for the activation barriers is investigated using atomic scale calculation in which Li ion pathways on the potential energy landscape in a  $c$ -axis channel have been traced using the ReaxFF potential [64] and  $2 \times 2 \times 1$  computational cells. The ReaxFF potential was previously used to study the amorphisation of  $\beta$ -eucryptite under pressure [104], [223], and its response to irradiation [223], [224]. The diffusion barriers have been determined via molecular statics calculations, in which Li ions are moved along a channel

while the total energy is evaluated at each position along the channels. The results are shown in Figure 6.5, where two cases were considered: one in which all Li ions along a channel moved in unison (Figure 6.5 (a)), and the other in which only one Li ion was moved along the channel from one local minimum of the energy to the next (Figure 6.5 (b)). These are referred to as correlated and uncorrelated diffusion, respectively [121]. Figure 6.5 shows that the barrier for correlated Li motion ( $\sim 0.45$  eV) per Li atom is significantly smaller than the energy required for uncorrelated hopping ( $\sim 1.2$  eV). These results are for single crystal calculations: as such, they are consistent with the results for the activation barriers for the diffusion along  $c$ -axis ( $\text{bulk}_{\parallel}$ ) obtained from the EIS experiments (Table 6.1): in both of ReaxFF calculations and the experimental values, there is a factor of  $\sim 3$  between the activation energy associated with the uncorrelated and correlated motion. Regardless of the correlated or uncorrelated hopping, the activation energy values from the ReaxFF calculations are somewhat smaller than those obtained in experiments: however, this does not prevent the assignment of correlated and uncorrelated motions to various temperature regimes, since the difference between barriers is rather larger. Using ReaxFF we have carried out the same calculations for lattice constants corresponding to different temperature up to  $900$  °C. The energy barriers determined via ReaxFF have not registered significant variations with temperature which is consistent with the low thermal expansion coefficient of  $\beta$ -eucryptite [41], [265]–[267], [285].

We now focus on providing a qualitative reasoning for the relative magnitudes of the activation energies listed in Table 6.1. Those are intrinsically related to the order-disorder transition in  $\beta$ -eucryptite, in which Li ions change their positions in the channels in the temperature range from  $460$  °C to  $550$  °C [5], [9], [32], [125], [286]. At room temperature, Li atoms occupy half of the available sites in the channels. There are two types of channels (one



primary and three secondary) for Li, with six available tetrahedral sites in each channel. Li ions in the primary channel occupy sites with  $z=1/6, 1/2, 5/6$  along the origin channel ( $x=y=0$ ), and are coplanar with Al atoms. Li ions occupy the other three secondary channels on sites with  $z=0, 1/3, 2/3$ , and are coplanar with Si atoms. This type of distribution occurs because the Al tetrahedra sheets are larger than the Si tetrahedra sheets, since Al ions are larger than Si ions. Stuffing Li ions into the channels within the Si layers reduces the dimensional mismatch of the Si sheets with Al sheets by enlarging the Si-tetrahedra sheets [32]. As a result, Li is distributed such that 25% of the channel Li ions are coplanar with the Al sheet and the other 75% are coplanar with the Si sheet for a fully ordered  $\beta$ -eucryptite at room temperature [32]. At temperatures above the transition, Li ions interchange with the initial vacancy sites, resulting in a random distribution over all framework channel sites [28]. This breaks the 25 to 75 ratio of Al tetrahedra sheets to Si tetrahedra sheets and causes the shrinkage of the size of the Si tetrahedral sheets. Thus, the activation energy for conduction in the disordered structure is slightly higher than that at low temperature for the ordered structure. Since there is no significant change in structure as the transformation is approached, the activation energies of order and disordered structure remain similar. However, in between the fully ordered and disordered structure,  $\beta$ -eucryptite seems to exhibit a very high activation energy in the temperature range of 440 °C to 500 °C. This is believed to arise because the disordering process requires that Li ions rearrange, thereby creating an additional barrier [9]. A similar phenomenon has been detected in solid acid proton conductor  $\text{CsH}_2\text{PO}_4$ , where the disordered structure at high temperature brings the conductivity to a much higher level while the activation energy remains similar to the low temperature ordered structure [281]. Others have shown that an incommensurate structure coexists with the low-temperature structure for 50 to 60 degrees in  $\beta$ -eucryptite [5], [125].

## 6.5 Conclusions

In conclusion, we have reported on the conductivity of polycrystalline  $\beta$ -eucryptite in various temperature regimes, focusing on resistance, ionic conductivity, energy barriers and the associated hopping mechanisms. Under the assumption that the grain boundaries do not change their structure significantly, we have extracted the one-dimensional conductivity along  $c$ -axis channels in polycrystalline samples, which has only been done previously for single crystals [4], [29]. Although the conduction along grain boundaries and that perpendicular to  $c$ -axis cannot be individually resolved in our EIS experiments, and premise of a common effective or average activation energy yields a value of 1.197 eV for the slow pathways. While not atypical, this value is rather high, and shows that grain boundaries limit severely the use of polycrystalline eucryptite for widespread ionic conduction applications. From a fundamental point of view, the use of one average conductivity for all slow pathways enabled us to determine three thermal regimes for the 1-dimensional ionic conduction (in bulk, parallel to the  $c$  axis): the low temperature regime (below 440 °C), order-disorder transformation regime (440 °C-500 °C), the calculated barriers are consistent with uncorrelated, individual hopping of Li atoms which occurs likely because in this temperature range the Li atoms have not yet assumed (on average) equispaced positions, and therefore the correlation between hops along the same channel is broken by closely spaced ions.

## 6.6 Acknowledgement

We gratefully acknowledge the support of U.S. Department of Energy's Office of Basic Energy Sciences through Grant No. DE-FG02-07ER46397, as well the partial support from the National Science Foundation through Grant No. 1534503. We thank Dr. Ryan O'Hayre for insightful discussions, and Mr. Chuancheng Duan for his help in designing some of the experiments.

## CHAPTER 7

### GENERAL DISCUSSION

The experiments investigated through this research were motivated by the desire to understand the unique property - structure relationships of  $\beta$ -eucryptite under high pressures and temperatures. The relevant discussions of the experiments and results of each section has been presented under specific chapters. This chapter provides a general discussion about the results obtained from last three sub-topics (CHAPTER 4-CHAPTER 6) and about the contributions of these investigations.

#### 7.1 Structural phase transformation under high pressures

Ceramics are recognized as hard, brittle materials. Thus, the importance of studying phase transformations in order to provide high toughness in ceramics has been realized for a long time. Most of the studies on phase transformations have focused on those have transformation pressures higher than that which are practical in materials processing for transformation toughening. In other words, materials that have phase transformation at moderate pressures are of more interest.  $\beta$ -eucryptite exhibits various phase transformations under high temperatures and pressures. The phase transformation that has the most potential usage happens between  $\beta$  and  $\varepsilon$ -eucryptite at about 1 GPa. In order to better tailor the phase transformation property, it is important to make the transformation applicable for transformation toughening. It is critical to know what the crystal structure of  $\varepsilon$ -eucryptite is. The crystal structure of pressure stabilized  $\varepsilon$ -eucryptite has been fully investigated in the present study by combining high energy x-ray diffraction and density functional theory. The 9% volume change associated with the transformation further confirmed the possibility of using metastable  $\varepsilon$ -eucryptite as a transformation toughening material. *In-situ* DAC-x-ray diffraction experiments of Mg doped  $\beta$ -

eucryptite were performed at the same conditions with pure  $\beta$ -eucryptite.  $\beta$ -eucryptite doped with 0.3 % Mg exists as single phase  $\beta$ -eucryptite under ambient conditions, but at high pressure evolves to a mixture of two phases, one that is  $\varepsilon$ -eucryptite ( $Pna2_1$ ) and a second phase with the  $Pca2_1$  space group. In addition, the presence of Mg dopant resulted in an increase in transformation pressure from  $\beta$  to  $\varepsilon$ -eucryptite compared with pure  $\beta$ -eucryptite.

Mg and Zn dopants tend to stabilize  $\beta$ -eucryptite instead of  $\varepsilon$ -eucryptite, grain size control becomes more important in stabilizing high pressure  $\varepsilon$ -eucryptite for using as a transformation toughener. The effects of grain size on transformation pressures were studied *in-situ* diamond anvil cell-x-ray diffractions on various grain sizes samples. The larger grain size samples were found to have lower phase transformation pressures than the fine grain size samples, indicating the grain size plays a role in determining the pressure at which  $\varepsilon$ -eucryptite is stable. When grain size exceeds about 1  $\mu\text{m}$ , the transformation pressure becomes independent with grain size. It has been shown that enthalpy between the different phases play a key role in the nucleation and growth. Spontaneous microcracking occurs when grain size is larger than about 2.8  $\mu\text{m}$  [49]. Thus, the importance of studying grain size effects on transformation pressure is that one can use the model to predict the transformation pressure for certain grain sizes in order to best fit the ceramic matrix and make materials with no microcracking.

## **7.2 Order-disorder transition at high temperatures**

The potential of using  $\beta$ -eucryptite as a solid electrolyte in Li batteries has been well realized due to its high anisotropic Li ionic conductivity. The interest to study structural changes of  $\beta$ -eucryptite at high temperature is because of its order-disorder transformation.

A large amount of studies have focused on measuring Li conductivity of single crystal  $\beta$ -eucryptite from room temperature up to 600 °C. The present study extends the measurement temperature to 900 °C to fully cover the order-disorder transition range. Although Li ion behaviors in the structure are really hard to study through x-ray diffractions, they can be characterized in an indirect way such as electrochemical impedance spectroscopy (EIS). Previous studies on the conductivity of  $\beta$ -eucryptite utilized single crystals to eliminate grain boundary effects which are present in polycrystalline samples. Though using EIS to study order-disorder transition of  $\beta$ -eucryptite has been developed in previous studies, grain boundary effects were for the first time taken into account in the present study. The brick layer model (BLM) was successfully applied on impedance results and separated the resistance of grain interior and grain boundary at low temperature range, where the semicircles were obvious. The present study contributes a method to study the grain interior responses by using the BLM and assuming that the grain boundary conducting mechanism does not change in the testing temperature range. This method can be applied to other material systems whose bulk conductivities are too high to be measured directly from impedance spectroscopy. The activation energy of  $\beta$ -eucryptite along *c*-axis clearly shows three regimes over the temperature range from 300 °C to 900 °C. The activation energies of high temperature range (500 °C to 900 °C) and low temperature range (300 °C to 440 °C) are close to each other, whereas the activation energy of intermediate temperature range (440 °C to 500 °C) is almost three times than the other two. This phenomenon indicates that Li may have more than one motion as temperature changes.

## CHAPTER 8

### CONCLUSION

It was demonstrated that  $\beta$ -eucryptite can be synthesized and processed by different routes to get single phase and crack-free specimens. Powder samples were used to perform *in-situ* diamond anvil cell-X-ray diffraction experiments. Structural changes under high pressures have been examined. A reversible phase transformation between low pressure  $\beta$ -eucryptite and high pressure  $\varepsilon$ -eucryptite has been detected in both pure  $\beta$ -eucryptite and 0.3 mol% Mg doped  $\beta$ -eucryptite. High pressure  $\varepsilon$ -eucryptite has been confirmed to adopt an orthorhombic crystal structure with  $Pna2_1$  space group, determined with the assistance of density functional theory study. This is the first time that  $\varepsilon$ -eucryptite has been reported with crystal structure, space group and atomic positions. The volume shrinkage associated with the phase transformation could thus be calculated, and it was found to be 9%. 0.3 mol% Mg doped  $\beta$ -eucryptite was observed to have a higher transformation pressure than pure  $\beta$ -eucryptite, indicating Mg dopants tend to stabilize the  $\beta$ -eucryptite. In addition, it is also observed that, unlike pure  $\beta$ -eucryptite which transforms to single phase  $\varepsilon$ -eucryptite, the presence of Mg leads to a phase mixture of  $Pna2_1$  and  $Pca2_1$  space groups at high pressure. The stability of  $\varepsilon$ -eucryptite has been examined by measuring phase transformation pressures of samples with various grain sizes. A linear relation between the reciprocal radius and pressure has been observed, indicating larger grain sizes lead to an “easier” phase transformation from  $\beta$  to  $\varepsilon$ -eucryptite. A modified traditional nucleation and growth model has been developed to fit the experimental results.

The structure changes (i.e. Li order-disorder transition) under high temperature have been studied by electrochemical impedance spectroscopy. Li conductivity increased with increasing

temperatures. Grain interior and grain boundary resistance have been separated by using a brick layer model. It has been shown that the grain bulk has three activation energies through the temperature range from 300 °C to 900 °C. The one at intermediate temperatures is three times the other two. The results motivated atomic calculations which were performed by others to simulate lithium ion diffusion to investigate the activation barriers. The Li correlated motion is shown to have 1/3 of activation barrier than the uncorrelated motion, consistent with the experimental results.  $\beta$ -eucryptite is confirmed to have a fully ordered structure at low temperature range (300 °C to 440 °C) and a disordered structure at high temperature range (500 °C to 900 °C). The order to disorder transition happens due to the Li uncorrelated motion and Li redistribution in the structure.

## CHAPTER 9

### SUGGESTIONS OF FUTURE WORK

This study focuses on examining the structure-property relationships of  $\beta$ -eucryptite under pressure and temperature individually. Although the crystal structure of high pressure  $\varepsilon$ -eucryptite has been determined and the grain size effect of the pressure-induced phase transformation from  $\beta$  to  $\varepsilon$ -eucryptite has been developed, it is interesting to develop how the structure changes with both pressure and temperature. Li order-disorder transition under temperature may also play a role to effect the pressure-induced phase transformation from  $\beta$  to  $\varepsilon$ -eucryptite. This chapter includes some preliminary results that show the transformation character in a certain temperature-pressure range. *In-situ* diamond anvil cell-Raman spectroscopy has been developed to be a promising technique to study structure-property relations under both pressure and temperature. The details of experimental setup are described in 3.4. Raman spectra of pure  $\beta$ -eucryptite under loading at room temperature are shown in Figure 9.1. The spectra at ambient pressure show two strong scattering around 484 and 1034  $\text{cm}^{-1}$ , which are in good agreement with previous reports [14], [125], [287]. The onset of the phase transformation is determined by the appearance of a secondary peak at about 518  $\text{cm}^{-1}$ , which is believed to correspond to  $\varepsilon$ -eucryptite [19]. The spectra under both temperature and pressure are similar with those under pressure only. Nevertheless, the temperature that can be applied to the samples is limited by the design of the diamond anvil cell. In addition, ruby is not a good pressure marker at high temperature. New pressure calibrator needs to be introduced as described in 3.2.5. Some preliminary results are shown in Figure 9.1 and Figure 9.2. In order to better understand the kinetics of phase transformation through *in-situ* DAC-Raman spectroscopy, several tasks need to achieve in the future:



- The ability to keep the high temperature stable in a diamond anvil cell is very important. For now, the temperature can only be controlled by adjusting the input current. The temperature has to be manually lower the input current when it exceeds the targeted point.
- New pressure calibrator needs to be developed other than ruby.  $\text{SrB}_4\text{O}_7: \text{Sm}^{2+}$  has been shown as a great candidate as its Raman spectra are almost independent with temperatures. In addition, the peaks are very intense even at high temperatures.
- Raman spectra of  $\beta$ -eucryptite are easily to adopt a high background at high temperatures due to the laser heating on the samples. It is critical to figure out the optimized integration times and accumulation parameters at high temperatures.

The experimental design in the preliminary study is to increase the temperature to a certain point first and then increase the pressure. In the future, another set of systematic tests can be considered to keep the pressure at a certain point (below or above the phase transformation point) and then vary the temperature to study the reversibility of the phase transformation to complete the temperature-pressure phase diagram of  $\beta$  and  $\epsilon$ -eucryptite.

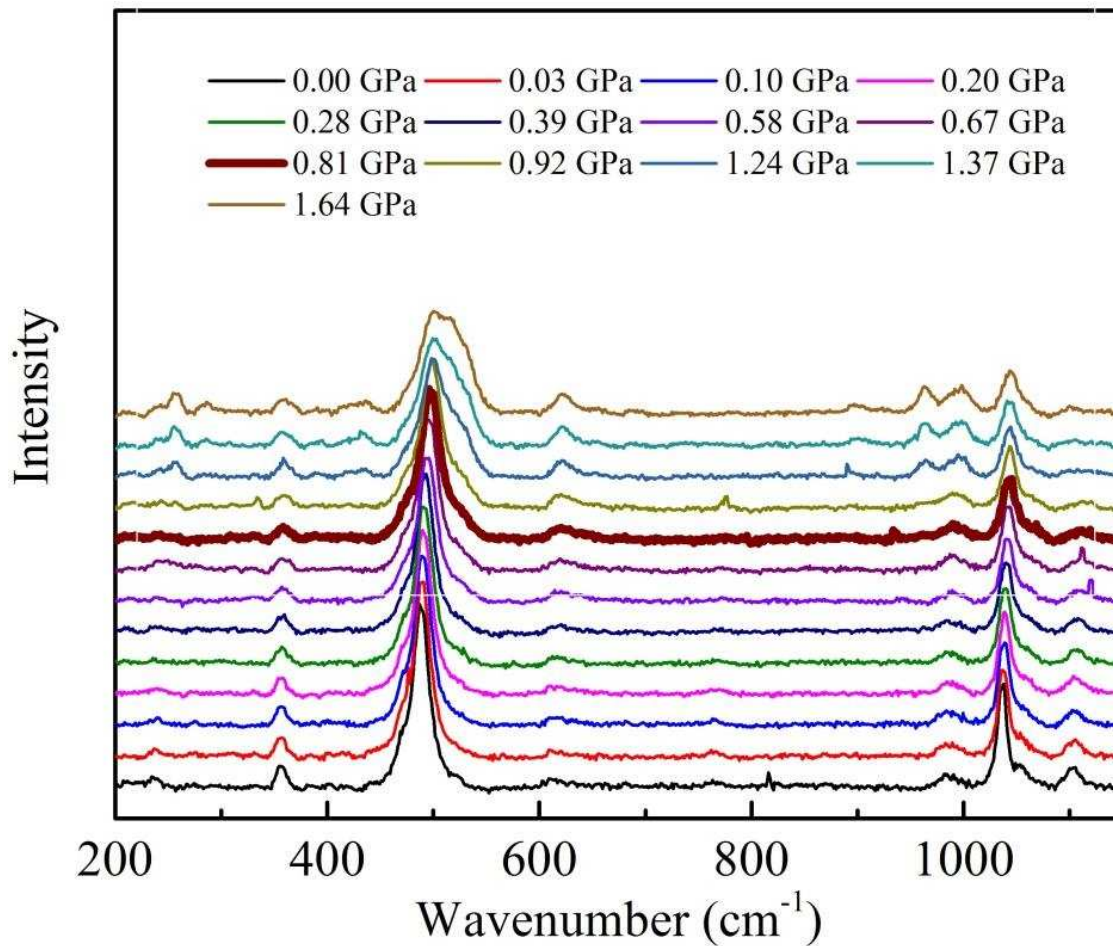


Figure 9.1 Raman spectra of pure  $\beta$ -eucryptite as a function of pressure collected during compression. The onset of phase transformation is indicated by the bold line.

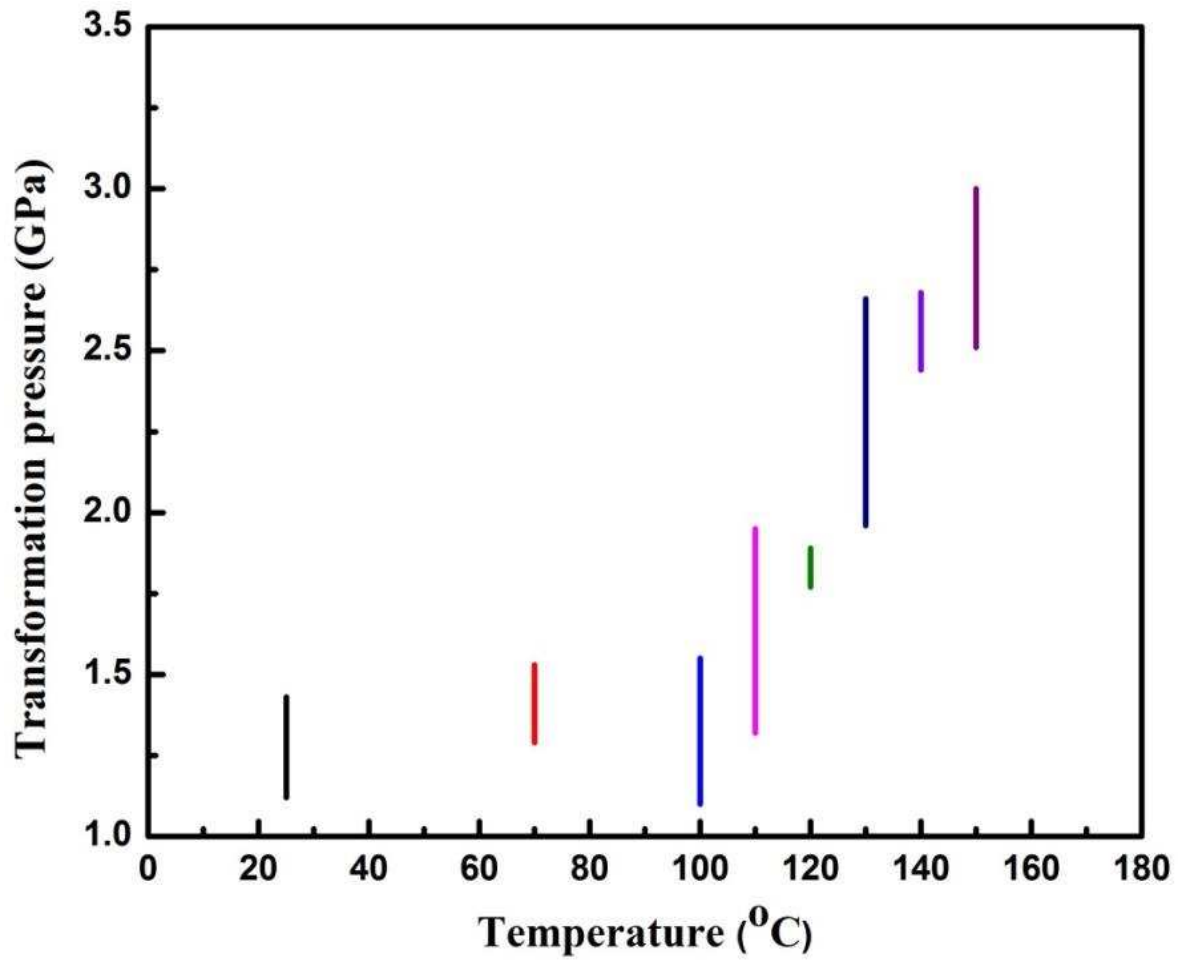


Figure 9.2 Transformation pressure of  $\beta$  to  $\epsilon$ -eucryptite at different temperatures.

## REFERENCES

- [1] H. Bach and D. Krause, *Low thermal expansion glass ceramics*. Springer, 2005.
- [2] P. J. Heaney, *Silica-Physical behavior, geochemistry and materials applications*. Washington, 1994.
- [3] W. Holand and G. H. Beall, *Glass ceramic technology*. American Ceramic Society, 2012.
- [4] U. V. Alpen, H. Schulz, G. H. Talat, and H. Böhm, “One-dimensional cooperative Li-diffusion in  $\beta$ -eucryptite,” *Solid State Commun.*, vol. 23, no. 12, pp. 911–914, Sep. 1977.
- [5] W. Press, B. Renker, H. Schulz, and H. Böhm, “Neutron scattering study of the one-dimensional ionic conductor  $\beta$ -eucryptite,” *Phys. Rev. B*, vol. 21, no. 3, pp. 1250–1257, Feb. 1980.
- [6] W. Nagel and H. Böhm, “Ionic Conductivity Solid Solutions Studies on  $\text{LiAlSiO}_4 - \text{SiO}_2$  of the High Quartz Type,” *Solid State Commun.*, vol. 42, no. 9, pp. 625–631, Jun. 1982.
- [7] B. Renker, H. Bernotat, G. Heger, N. Lehner, and W. Press, “Li-diffusion and lattice relaxation in the 1-D superionic-conductor beta-eucryptite ( $\text{LiAlSiO}_4$ ),” *Solid State Ionics*, vol. 9–10, no. PART 2, pp. 1341–1343, Dec. 1983.
- [8] A. Sartbaeva, S. A. Wells, and S. A. T. Redfern, “ $\text{Li}^+$  ion motion in quartz and  $\beta$ -eucryptite studied by dielectric spectroscopy and atomistic simulations,” *J. Phys. Condens. Matter*, vol. 16, no. 46, p. 8173, Nov. 2004.
- [9] W. W. Pillars and D. R. Peacor, “The Crystal Structure of Beta Eucryptite as a Function of Temperature,” *Am. Miner.*, vol. 58, pp. 681–690, 1973.
- [10] H. Xu, P. J. Heaney, and H. Bohm, “Structural modulations and phase transitions in  $\beta$ -eucryptite: an in-situ TEM study,” *Phys. Chem. Miner.*, vol. 26, no. 8, pp. 633–643, Sep. 1999.
- [11] P. Richet and P. Gillet, “Pressure-induced amorphization of minerals: a review,” *Eur. J. Mineral.*, pp. 907–934, 1997.
- [12] J. Zhang, A. Celestian, J. B. Parise, H. Xu, and P. J. Heaney, “A new polymorph of eucryptite ( $\text{LiAlSiO}_4$ ),  $\epsilon$ -eucryptite, and thermal expansion of  $\alpha$ - and  $\epsilon$ -eucryptite at high pressure,” *Am. Mineral.*, vol. 87, no. 4, pp. 566–571, Apr. 2002.
- [13] J. Zhang, Y. Zhao, H. Xu, M. V. Zelinskas, L. Wang, Y. Wang, and T. Uchida, “Pressure-induced amorphization and phase transformations in  $\beta$ - $\text{LiAlSiO}_4$ ,” *Chem. Mater.*, vol. 17, no. 11, pp. 2817–2824, May 2005.

- [14] T. Jochum, I. E. Reimanis, M. J. Lance, and E. R. Fuller, "In situ Raman indentation of  $\beta$ -eucryptite: Characterization of the pressure-induced phase transformation," *J. Am. Ceram. Soc.*, vol. 92, no. 4, pp. 857–863, Apr. 2009.
- [15] B. Morosin and P. S. Peercy, "Pressure-induced phase transition in  $\beta$ -eucryptite ( $\text{LiAlSiO}_4$ )," *Phys. Lett. A*, vol. 53, no. 2, pp. 147–148, Jun. 1975.
- [16] S. Ramalingam, I. E. Reimanis, and C. E. Packard, "Determining activation volume for the pressure-induced phase transformation in  $\beta$ -eucryptite through nanoindentation," *J. Am. Ceram. Soc.*, vol. 95, no. 6, pp. 2051–2058, Jun. 2012.
- [17] S. Ramalingam, "Thermo-mechanical behavior of  $\beta$ -eucryptite and eucryptite based composites," Colorado School of Mines, 2013.
- [18] I. E. Reimanis, C. Seick, and K. Fitzpatrick, "Implementing a Pressure-Induced Phase Transformation in Beta-Eucryptite to Impart Toughening," 2010.
- [19] S. Ramalingam, C. E. Packard, and I. E. Reimanis, "In situ diamond anvil cell-Raman spectroscopy and nanoindentation study of the pressure-induced phase transformation in pure and zinc-doped  $\beta$ -eucryptite," *J. Am. Ceram. Soc.*, vol. 96, no. 6, pp. 1909–1915, Jun. 2013.
- [20] R. H. J. Hannink, P. M. Kelly, and B. C. Muddle, "Transformation Toughening in Zirconia-Containing Ceramics," *J. Am. Ceram. Soc.*, vol. 83, no. 3, pp. 461–487, Mar. 2000.
- [21] A. H. HEUER, N. CLAUSSEN, W. M. KRIVEN, and M. RUHLE, "Stability of Tetragonal  $\text{ZrO}_2$  Particles in Ceramic Matrices," *J. Am. Ceram. Soc.*, vol. 65, no. 12, pp. 642–650, Dec. 1982.
- [22] R. C. Garvie and M. V. Swain, "Thermodynamics of the tetragonal to monoclinic phase transformation in constrained zirconia microcrystals Part 1: In the absence of an applied stress field," *J. Mater. Sci.*, vol. 20, no. 4, pp. 1193–1200, Apr. 1985.
- [23] R. C. Garvie, "Stabilization of the tetragonal structure in zirconia microcrystals," *J. Phys. Chem.*, vol. 82, no. 2, pp. 218–224, Jan. 1978.
- [24] H. Winkler, "Synthese und Kristallstruktur des Eukryptits,  $\text{LiAlSiO}_4$ ," *Acta Crystallogr.*, vol. 1, no. 1, pp. 27–34, Mar. 1948.
- [25] M. Buoncon, "The Stuffed Derivatives of the Silica Structures," *Am. Miner.*, vol. 39, pp. 600–615, 1954.
- [26] E. J. Hornyak, "Ph.D. Thesis," University of Michigan, 1969.

- [27] H. Schulz and V. Tscherry, "Structural relations between the low- and high-temperature forms of  $\beta$ -eucryptite ( $\text{LiAlSiO}_4$ ) and low and high quartz. I. Low-temperature form of  $\beta$ -eucryptite and low quartz," *Acta Crystallogr. Sect. B Struct. Crystallogr. Cryst. Chem.*, vol. 28, no. 7, pp. 2168–2173, 1972.
- [28] H. Schulz and V. Tscherry, "Structural relations between the low and high-temperature forms of  $\beta$ -eucryptite ( $\text{LiAlSiO}_4$ ) and low and high quartz. II. High-temperature form of  $\beta$ -eucryptite and high quartz," *Acta Crystallogr. Sect. B Struct. Crystallogr. Cryst. Chem.*, vol. 28, no. 7, pp. 2174–2177, 1972.
- [29] U. V Alpen, E. Schönherr, H. Schulz, and G. H. Talat, " $\beta$ -eucryptite—a one-dimensional Li-ionic conductor," *Electrochim. Acta*, vol. 22, no. 7, pp. 805–807, Jul. 1977.
- [30] V. Tscherry, H. Schulz, and F. Laves, "Average and super structure of  $\beta$ -eucryptite ( $\text{LiAlSiO}_4$ ) Part I. Average structure," *Zeitschrift Fur Krist.*, vol. 135, no. 3–4, pp. 161–174, 1972.
- [31] R. D. Shannon and C. T. Prewitt, "Effective ionic radii in oxide and fluorides," *Acta Crystallogr.*, vol. 25, pp. 925–946, 1969.
- [32] H. Xu, P. J. Heaney, D. M. Yates, R. B. Von Dreele, and M. A. Bourke, "Structural mechanisms underlying near-zero thermal expansion in  $\beta$ -eucryptite: A combined synchrotron x-ray and neutron Rietveld analysis," *J. Mater. Res.*, vol. 14, no. 7, pp. 3138–3151, 1999.
- [33] V. Tscherry, H. Schulz, and F. Laves, "Average and super structure of  $\beta$ -eucryptite ( $\text{LiAlSiO}_4$ ) Part II. Superstructure," *Zeitschrift Fur Krist.*, vol. 135, no. 3–4, pp. 175–198, 1972.
- [34] H. Xu, P. J. Heaney, P. Yu, and H. Xu, "Synthesis and structure of a stuffed derivative of  $\alpha$ -quartz,  $\text{Mg}_{0.5}\text{AlSiO}_4$ ," *Am. Mineral.*, vol. 100, no. 10, pp. 2191–2198, Oct. 2015.
- [35] W. Loewenstein, "The distribution of aluminum in the tetrahedra of silicates and aluminates," *Am. Mineral.*, vol. 39, pp. 92–96, 1954.
- [36] H. Guth and G. Heger, *Fast Ion Transport in Solid, Electrodes and Electrolytes*. .
- [37] H. Xu, P. J. Heaney, A. Navrotsky, L. Topor, and J. Liu, "Thermochemistry of stuffed quartz-derivative phases along the join  $\text{LiAlSiO}_4\text{-SiO}_2$ ," *Am. Mineral.*, vol. 84, pp. 1360–1369, 1999.
- [38] B. Singh, M. K. Gupta, R. Mittal, M. Zbiri, S. Rols, S. J. Patwe, S. N. Achary, H. Schober, A. K. Tyagi, and S. L. Chaplot, "Role of Phonons in Li-Diffusion, Thermal Expansion and Phase Transitions in  $\beta$ -eucryptite: Inelastic Neutron Scattering and Lattice Dynamics Studies," *arXiv Prepr. arXiv1602.08285*, 2016.

- [39] N. Khosrovani and A. W. Sleight, "Strong anisotropic thermal expansion in oxides," *Int. J. Inorg. Mater.*, vol. 1, no. 1, pp. 3–10, Apr. 1999.
- [40] R. T. Johnson, "Ionic Conductivity in Solid Electrolytes Based on Lithium Aluminosilicate Glass and Glass-Ceramic," *J. Electrochem. Soc.*, vol. 123, no. 5, p. 680, May 1976.
- [41] F. H. Gillery and E. A. Bush, "Thermal Contraction of  $\beta$ -Eucryptite ( $\text{Li}_2\text{O}\cdot\text{Al}_2\text{O}_3\cdot 2\text{SiO}_2$ ) by X-Ray and Dilatometer Methods," *J. Am. Ceram. Soc.*, vol. 42, no. 4, pp. 175–177, Apr. 1959.
- [42] S. Ramalingam and I. E. Reimanis, "Effect of doping on the thermal expansion of  $\beta$ -eucryptite prepared by sol-gel methods," in *Journal of the American Ceramic Society*, 2012, vol. 95, no. 9, pp. 2939–2943.
- [43] J. S. O. Evans, "Negative thermal expansion materials<sup>†</sup>," *J. Chem. Soc. Dalt. Trans.*, vol. 0, no. 19, pp. 3317–3326, 1999.
- [44] V. Donduft, R. Dimitrijević, and N. Petranović, " $\text{Li}^+$  ion mobility in eucryptite phases," *J. Mater. Sci.*, vol. 23, no. 11, pp. 4081–4084, Nov. 1988.
- [45] E. Gmelin, "Low temperature heat capacity and thermodynamic standard values at 298.15 of  $\beta$ -eucryptite ( $\text{LiAlSiO}_4$ )," *Thermochim. Acta*, vol. 399, no. 1–2, pp. 241–244, Mar. 2003.
- [46] L. Xia, G. W. Wen, C. L. Qin, X. Y. Wang, and L. Song, "Mechanical and thermal expansion properties of  $\beta$ -eucryptite prepared by sol-gel methods and hot pressing," *Mater. Des.*, vol. 32, no. 5, pp. 2526–2531, May 2011.
- [47] V. Correcher, Y. Rodriguez-Lazcano, J. Garcia-Guinea, and E. Crespo-Feo, "Blue thermoluminescence emission of annealed lithium rich aluminosilicates," *Brazilian J. Phys.*, vol. 40, no. 3, pp. 348–352, Sep. 2010.
- [48] S. Haussühl, W. Nagel, and H. Böhm, "Elastic and thermoelastic constants of hexagonal  $\beta$ - $\text{LiAlSiO}_4$ ," *Zeitschrift für Krist. - Cryst. Mater.*, vol. 169, no. 1–4, pp. 299–304, Jan. 1984.
- [49] A. Pelletant, H. Reveron, J. Chêvalier, G. Fantozzi, L. Blanchard, F. Guinot, and F. Falzon, "Grain size dependence of pure  $\beta$ -eucryptite thermal expansion coefficient," *Mater. Lett.*, vol. 66, no. 1, pp. 68–71, Jan. 2012.
- [50] Y. Chen and I. Reimanis, "Unpublished data," 2015.
- [51] H. Schulz, W. Hoffmann, and G. M. Muchow, "Structural characteristics of a Mg-Al silicate of the high quartz type," *Naturwissenschaften*, vol. 57, no. 5, pp. 242–243, May

1970.

- [52] A. I. Lichtenstein, R. O. Jones, S. de Gironcoli, and S. Baroni, “Anisotropic thermal expansion in silicates: A density functional study of  $\beta$ -eucryptite and related materials,” *Phys. Rev. B*, vol. 62, no. 17, pp. 11487–11493, Nov. 2000.
- [53] W. Schreyer and J. Schairer, “Metastable solid solutions with quartz-type structures on the join  $\text{SiO}_2\text{—MgAl}_2\text{O}_4$ ,” *Zeitschrift für Krist. - Cryst. Mater.*, vol. 116, no. 1–6, pp. 60–82, Jan. 1961.
- [54] M. Sternitzke and G. Müller, “Crystal structure and thermal expansion of quartz-type aluminosilicates,” *J. Mater. Sci.*, vol. 26, no. 11, pp. 3051–3056, 1991.
- [55] G. Müller, M. Hoffmann, and R. Neeff, “Hydrogen substitution in lithium-aluminosilicates,” *J. Mater. Sci.*, vol. 23, no. 5, pp. 1779–1785, May 1988.
- [56] I. E. Reimanis, C. Seick, K. Fitzpatrick, E. R. Fuller, and S. Landin, “Spontaneous Ejecta from  $\beta$ -Eucryptite Composites,” *J. Am. Ceram. Soc.*, vol. 90, no. 8, pp. 2497–2501, Aug. 2007.
- [57] I. Reimanis, “Private communication with H. Xu.” 2007.
- [58] H. Somekawa and C. A. Schuh, “Effect of solid solution elements on nanoindentation hardness, rate dependence, and incipient plasticity in fine grained magnesium alloys,” *Acta Mater.*, vol. 59, pp. 7554–7563, 2011.
- [59] Q. Wei, “Strain rate effects in the ultrafine grain and nanocrystalline regimes—influence on some constitutive responses,” 2007.
- [60] C. A. Schuh, “Nanoindentation studies of materials,” *Mater. Today*, vol. 9, pp. 32–40, 2006.
- [61] C. A. Schuh, J. K. Mason, and A. C. Lund, “Quantitative insight into dislocation nucleation from high-temperature nanoindentation experiments,” 2005.
- [62] J. K. Mason, A. C. Lund, and C. A. Schuh, “Determining the activation energy and volume for the onset of plasticity during nanoindentation,” *Phys. Rev. B*, vol. 73, p. 54102, 2006.
- [63] C. A. Schuh and A. C. Lund, “Application of nucleation theory to the rate dependence of incipient plasticity during nanoindentation,” *J. Mater. Res.*, vol. 19, no. 7, pp. 2152–2158, Jul. 2004.
- [64] B. Narayanan, A. C. T. van Duin, B. B. Kappes, I. E. Reimanis, and C. V Ciobanu, “A



- reactive force field for lithium–aluminum silicates with applications to eucryptite phases,” *Model. Simul. Mater. Sci. Eng.*, vol. 20, no. 1, p. 15002, Jan. 2012.
- [65] G. Burns and A. M. Glazer, *Space Groups for Solid State Scientists*. 1990.
- [66] D. A. Porter and K. E. S. Y. Easterling, *Phase Transformations in Metals and Alloys*. CRC press, 2009.
- [67] R. O’Hayre, *Materials Kinetics Fundamental*. John Wiley & Sons, 2015.
- [68] R. W. Balluffi, S. M. Allen, and W. C. Carter, *Kinetics of materials*. John Wiley & Sons, 2005.
- [69] S. H. Tolbert and A. P. Alivisatos, “Size Dependence of a First Order Solid-Solid Phase Transition: The Wurtzite to Rock Salt Transformation in CdSe Nanocrystals,” *Science (80-. )*, vol. 265, pp. 373–376, 1994.
- [70] S. H. Tolbert and A. P. Alivisatos, “The wurtzite to rock salt structural transformation in CdSe nanocrystals under high pressure,” *J. Chem. Phys.*, vol. 102, no. 11, p. 4642, 1995.
- [71] S. H. Tolbert, A. B. Herhold, L. E. Brus, and A. P. Alivisatos, “Pressure-Induced Structural Transformations in Si Nanocrystals: Surface and Shape Effects,” 1996.
- [72] S. B. Qadri, J. Yang, B. R. Ratna, E. F. Skelton, J. Z. Hu, E. F. Skelton, and J. Z. Hu, “Pressure induced structural transitions in nanometer size particles of PbS,” *Appl. Phys. Lett.*, vol. 69, 1996.
- [73] J. Z. Jiang, J. S. Olsen, L. Gerward, and S. Mørup, “Enhanced bulk modulus and reduced transition pressure in  $\gamma$ -Fe<sub>2</sub>O<sub>3</sub> nanocrystals,” *Europhys. Lett.*, vol. 44, no. 5, pp. 620–626, Dec. 1998.
- [74] S. B. Qadri, E. F. Skelton, A. D. Dinsmore, J. Z. Hu, W. J. Kim, C. Nelson, and B. R. Ratna, “The effect of particle size on the structural transitions in zinc sulfide,” *J. Appl. Phys.*, vol. 89, no. 1, p. 115, 2001.
- [75] J. Z. Jiang, L. Gerward, D. Frost, R. S. Secco, J. Peyronneau, J. Olsen, L. Gerward, D. Frost, R. Secco, J. Peyronneau, and J. S. Olsen, “Grain-size effect on pressure-induced semiconductor-to-metal transition in ZnS,” *J. Appl. Phys.*, vol. 86, no. 6608, 1999.
- [76] J. D. Eshelby, “The Determination of the Elastic Field of an Ellipsoidal Inclusion, and Related Problems,” *Proc. R. Soc. A Math. Phys. Eng. Sci.*, vol. 241, no. 1226, pp. 376–396, Aug. 1957.
- [77] D. Green, R. Hannink, and M. Swain, *Transformation toughening of ceramics*. CRC Press,

Boca Raton, FL, 1989.

- [78] M. V Swain and R. H. Hannink, "R-curve behavior in zirconia ceramics," in *Science and technology of zirconia II*, 1983.
- [79] A. Evans, "Toughening mechanisms in zirconia alloys," in *Science and technology of zirconia II*, 1983.
- [80] R. C. Garvie, R. H. Hannink, and R. T. Pascoe, "Ceramic steel?," *Nature*, vol. 258, no. 5537, pp. 703–704, Dec. 1975.
- [81] N. Claussen, "Fracture Toughness of  $\text{Al}_2\text{O}_3$  with an Unstabilized  $\text{ZrO}_2$  Dispersed Phase," *J. Am. Ceram. Soc.*, vol. 59, no. 1–2, pp. 49–51, Jan. 1976.
- [82] R. H. J. Hannink, "Growth morphology of the tetragonal phase in partially stabilized zirconia," *J. Mater. Sci.*, vol. 13, no. 11, pp. 2487–2496, Nov. 1978.
- [83] D. L. Porter and A. H. Heuer, "Mechanisms of Toughening Partially Stabilized Zirconia (PSZ)," *J. Am. Ceram. Soc.*, vol. 60, no. 3–4, pp. 183–184, Mar. 1977.
- [84] A. G. Evans and A. H. Heuer, "REVIEW—Transformation Toughening in Ceramics: Martensitic Transformations in Crack-Tip Stress Fields," *J. Am. Ceram. Soc.*, vol. 63, no. 5–6, pp. 241–248, 1980.
- [85] A. G. Evans, N. Burlingame, M. Drory, and W. M. Kriven, "Martensitic transformations in zirconia-particle size effects and toughening," *Acta Metall.*, vol. 29, no. 2, pp. 447–456, 1981.
- [86] R. McMeeking and A. G. Evans, "Mechanics of Transformation-Toughening in Brittle Materials," *J. Am. Ceram. Soc.*, vol. 65, no. 5, pp. 242–246, May 1982.
- [87] J. Wang and R. Stevens, "Zirconia-toughened alumina (ZTA) ceramics," *Journal of Materials Science*, vol. 24, no. 10, pp. 3421–3440, Oct-1989.
- [88] Y. Ikuma, W. Komatsu, and S. Yaegashi, " $\text{ZrO}_2$ -toughened MgO and critical factors in toughening ceramic materials by incorporating zirconia," *J. Mater. Sci. Lett.*, vol. 4, no. 1, pp. 63–66, 1985.
- [89] M. McCOY, W. E. LEE, and A. H. HEUER, "Crystallization of  $\text{MgO-Al}_2\text{O}_3\text{-SiO}_2\text{-ZrO}_2$  Glasses," *J. Am. Ceram. Soc.*, vol. 69, no. 3, pp. 292–296, Mar. 1986.
- [90] N. CLAUSSEN and J. JAHN, "Mechanical Properties of Sintered, In Situ-Reacted Mullite-Zirconia Composites," *J. Am. Ceram. Soc.*, vol. 63, no. 3–4, pp. 228–229, Mar. 1980.

- [91] K. D. KEEFER and T. A. MICHALSKE, "Determination of Phase Transformation Depth Profiles with Synchrotron Radiation," *J. Am. Ceram. Soc.*, vol. 70, no. 4, pp. 227–231, Apr. 1987.
- [92] A. G. Evans and R. M. Cannon, "Overview no. 48: Toughening of brittle solids by martensitic transformations," *Acta Metall.*, vol. 34, no. 5, pp. 761–800, May 1986.
- [93] D. B. Marshall, A. G. Evans, and M. D. Drory, "Transformation Toughening in Ceramics," in *Fracture Mechanics of Ceramics*, and F. F. L. R. C. Bradt, A. G. Evans, D. P. H. Hasselman, Ed. Plenum Press, New York, 1983, pp. 289–307.
- [94] B. L. Karihaloo and J. H. Andreasen, *Mechanics of Transformation Toughening and Related Topics*. New York, 1996.
- [95] A. G. Evans, "Perspective on the Development of High-Toughness Ceramics," *J. Am. Ceram. Soc.*, vol. 73, no. 2, pp. 187–206, 1990.
- [96] J. H. Andreasen and B. L. Karihaloo, *Mechanics of Transformation Toughening and Related Topics*. Elsevier, 1996.
- [97] D. L. Porter and A. H. Heuer, "Microstructural Development in MgO-Partially Stabilized Zirconia (Mg-PSZ)," *J. Am. Ceram. Soc.*, vol. 62, no. 5–6, pp. 298–305, 1979.
- [98] E. D. Whitney, "Electrical Resistivity and Diffusionless Phase Transformations of Zirconia at High Temperatures and Ultrahigh Pressures," *J. Electrochem. Soc.*, vol. 112, no. 1, p. 91, 1965.
- [99] E. D. Whitney, "Effect of Pressure on Monoclinic-Tetragonal Transition of Zirconia; Thermodynamics," *J. Am. Ceram. Soc.*, vol. 45, no. 12, pp. 612–613, Dec. 1962.
- [100] R. C. Garvie, "The Occurrence of Metastable Tetragonal Zirconia as a Crystallite Size Effect."
- [101] W. Lee and A. H. Heuer, "On the Polymorphism of Enstatite," *J. Am. Ceram. Soc.*, vol. 70, no. 5, pp. 349–360, May 1987.
- [102] W. M. Kriven, "Possible Alternative Transformation Tougheners to Zirconia: Crystallographic Aspects," *J. Am. Ceram. Soc.*, vol. 71, no. 12, pp. 1021–1030, Dec. 1988.
- [103] W. M. Kriven, "Martensitic toughening of ceramics," *Mater. Sci. Eng. A*, vol. 127, no. 2, pp. 249–255, Aug. 1990.
- [104] Y. Chen, S. Manna, B. Narayanan, Z. Wang, I. E. Reimanis, and C. V Ciobanu, "Pressure-induced phase transformation in  $\beta$ -eucryptite: An X-ray diffraction and density functional

- theory study,” *Scr. Mater.*, vol. 122, pp. 64–67, 2016.
- [105] U. V Alpen, A. Rabenau, and G. H. Talat, “Ionic conductivity in Li<sub>3</sub>N single crystals,” *Appl. Phys. Lett.*, vol. 30, no. 12, pp. 621–623, 1977.
- [106] Y.-F. Y. Yao and J. Kummer, “Ion exchange properties of and rates of ionic diffusion in beta-alumina,” *J. inorg. nucl. Chem.*, vol. 29, pp. 2453–2475, 1967.
- [107] J. B. Boyce and J. C. Mikkelsen, “Anisotropic conductivity in a channel-structured superionic conductor: Li<sub>2</sub>Ti<sub>3</sub>O<sub>7</sub>,” *Solid State Commun.*, vol. 31, pp. 741–745, 1979.
- [108] L. Cheng, C. H. Wu, A. Jarry, W. Chen, Y. Ye, J. Zhu, R. Kostecki, K. Persson, J. Guo, M. Salmeron, G. Chen, and M. Doeff, “Interrelationships among Grain Size, Surface Composition, Air Stability, and Interfacial Resistance of Al-Substituted Li<sub>7</sub>La<sub>3</sub>Zr<sub>2</sub>O<sub>12</sub> Solid Electrolytes,” *ACS Appl. Mater. Interfaces*, vol. 7, no. 32, pp. 17649–17655, Aug. 2015.
- [109] P. M. Panchmatia, A. R. Armstrong, P. G. Bruce, and M. S. Islam, “Lithium-ion diffusion mechanisms in the battery anode material Li<sub>1+x</sub>V<sub>1-x</sub>O<sub>2</sub>,” *Phys. Chem. Chem. Phys.*, vol. 16, no. 39, pp. 21114–21118, Jul. 2014.
- [110] R. T. Johnson Jr., B. Morosin, M. L. Knotek, and R. M. Biefeld, “Ionic conductivity in LiAlSiO<sub>4</sub>,” *Phys. Lett. A*, vol. 54, no. 5, pp. 403–404, Oct. 1975.
- [111] R. A. Huggins, “Recent results on lithium ion conductors,” *Electrochimica Acta*, vol. 22, pp. 773–781, 1977.
- [112] H. Y. P. Hong, “Crystal structure and ionic conductivity of Li<sub>14</sub>Zn(GeO<sub>4</sub>)<sub>4</sub> and other new Li<sup>+</sup> superionic conductors,” *Mater. Res. Bull.*, 1978.
- [113] J. Kuwano and A. R. West, “New Li<sup>+</sup> ion conductors in the system, Li<sub>4</sub>GeO<sub>4</sub>-Li<sub>3</sub>VO<sub>4</sub>,” *Mat. Res. Bull.*, vol. 15, pp. 1661–1667, 1980.
- [114] H. Aono, E. Sugimoto, Y. Sadaoka, N. Imanaka, and G. Adachi, “Ionic Conductivity of Solid Electrolytes Based on Lithium Titanium Phosphate,” *J. Electrochem. Soc.*, vol. 137, no. 4, p. 1023, 1990.
- [115] M. Itoh, Y. Inaguma, W. H. Jung, L. Chen, and T. Nakamura, “High lithium ion conductivity in the perovskite-type compounds Ln<sub>12</sub>Li<sub>12</sub>TiO<sub>3</sub> (Ln=La,Pr,Nd,Sm),” *Solid State Ionics*, 1994.
- [116] V. Tscherry and F. Laves, “Synthesis and X-ray reflection pattern of β-eucryptite,” *Naturwissenschaften*, vol. 57, no. 4, p. 194, 1970.

- [117] G. C. Farrington and J. L. Briant, "Fast ionic transport in solids.," *Science*, vol. 204, no. 4400, pp. 1371–1379, Jun. 1979.
- [118] D. M. Follstaedt and P. M. Richards, "NMR Relaxation in the Superionic Conductor  $\beta$ -eucryptite," *Phys. Rev. Lett.*, vol. 37, no. 23, pp. 1571–1574, Dec. 1976.
- [119] P. M. Richards, "Microwave conductivity evidence for order-disorder transition in the superionic conductor  $\beta$ -eucryptite," *Phys. Lett. A*, vol. 69, no. 1, pp. 58–60, Nov. 1978.
- [120] A. Sartbaeva, S. a. T. Redfern, and W. T. Lee, "A neutron diffraction and Rietveld analysis of cooperative Li motion in beta-eucryptite," *J. Phys. Condens. Matter*, vol. 16, no. 29, pp. 5267–5278, Jul. 2004.
- [121] A. I. Lichtenstein, R. O. Jones, H. Xu, and P. J. Heaney, "Anisotropic thermal expansion in the silicate  $\beta$ -eucryptite: A neutron diffraction and density functional study," *Phys. Rev. B*, vol. 58, no. 10, pp. 6219–6223, Sep. 1998.
- [122] H. Böhm, "Dielectric properties of  $\beta$ -eucryptite," *Phys. status solidi*, vol. 30, no. 2, pp. 531–536, Aug. 1975.
- [123] F. Shin-Ichi, S. Satoshi, S. Kaduhiro, and T. Hitoshi, "Preparation and ionic conductivity of  $\beta$ -LiAlSiO<sub>4</sub> thin film," *Solid State Ionics*, vol. 167, no. 3–4, pp. 325–329, Feb. 2004.
- [124] S. M. Munro B and H. P., "AC impedance studies of glassy and crystalline lithium aluminosilicate compounds," *Ber. Bunsenges. Phys. Chem*, vol. 96, pp. 1718–1723, 1992.
- [125] M. Zhang, H. Xu, E. K. H. Salje, and P. J. Heaney, "Vibrational spectroscopy of beta-eucryptite (LiAlSiO<sub>4</sub>): optical phonons and phase transition(s)," *Phys. Chem. Miner.*, vol. 30, no. 8, pp. 457–462, Sep. 2003.
- [126] D. Mazza and M. Lucco-Borlera, "Effect of the substitution of boron for aluminium in the  $\beta$ -eucryptite LiAlSiO<sub>4</sub> structure," *J. Eur. Ceram. Soc.*, vol. 13, no. 1, pp. 61–65, 1994.
- [127] D. Mazza, M. Lucco-Borlera, G. Busca, and A. Delmastro, "High-quartz solid-solution phases from xerogels with composition 2MgO<sub>2</sub>Al<sub>2</sub>O<sub>3</sub><sub>5</sub>SiO<sub>2</sub> ( $\mu$ -cordierite) and Li<sub>2</sub>O<sub>·</sub>Al<sub>2</sub>O<sub>3</sub><sub>n</sub>SiO<sub><sub>2</sub>>," *J. Eur. Ceram. Soc.*, vol. 11, no. 4, pp. 299–308, 1993.
- [128] W. I. Abdel-Fattah, M. S. Fayed, S. R. Gooda, and W. F. F. Mekky, " $\beta$ -eucryptite by a sol-gel Route," *J. Sol-Gel Sci. Technol.*, vol. 13, pp. 981–985, 1998.
- [129] A. E. Danks, S. R. Hall, and Z. Schnepp, "The evolution of 'sol-gel' chemistry as a technique for materials synthesis," *Mater. Horiz.*, vol. 3, no. 2, pp. 91–112, 2016.
- [130] M. J. Buckley, A.M.; Greenblatt, "Sol-Gel Preparation of Silica Gels," *J. Chem. Ed.*, vol.

71, no. 7. p. 599, 1994.

- [131] C. A. Milea, C. Bogatu, and A. Duță, "THE INFLUENCE OF PARAMETERS IN SILICA SOL-GEL PROCESS," *Bull. Transilv. Univ. Braşov*, vol. 4, no. 1, 2011.
- [132] C. J. Barbé, D. J. Cassidy, G. Triani, B. A. Latella, D. R. G. Mitchell, K. S. Finnie, K. Short, J. R. Bartlett, J. L. Woolfrey, and G. A. Collins, "Sol-gel bonding of silicon wafers Part 1: Influence of the processing temperature on final bond morphology and interfacial energy," 2005.
- [133] C. J. Brinker and G. W. Scherer, *Sol-gel science : the physics and chemistry of sol-gel processing*. Academic Press, 1990.
- [134] M. A. Fardad, "Catalysts and the structure of SiO<sub>2</sub> sol-gel films," *J. Mater. Sci.*, vol. 35, no. 7, pp. 1835–1841, 2000.
- [135] R. K. Iler, *The chemistry of silica*. Wiley, New York, 1979.
- [136] M. Morpurgo, D. Teoli, M. Pignatto, M. Attrezzi, F. Spadaro, and N. Realdon, "The effect of Na<sub>2</sub>CO<sub>3</sub>, NaF and NH<sub>4</sub>OH on the stability and release behavior of sol-gel derived silica xerogels embedded with bioactive compounds," 2009.
- [137] H. K. Schmidt, E. Geiter, M. Mennig, H. Krug, C. Becker, and R.-P. Winkler, "The Sol-Gel Process for Nano-Technologies: New Nanocomposites with Interesting Optical and Mechanical Properties," *J. Sol-Gel Sci. Technol.*, vol. 16, no. 13, pp. 397–404, 1998.
- [138] B. Topuz and M. Çiftçioğlu, "Preparation of particulate/polymeric sol-gel derived microporous silica membranes and determination of their gas permeation properties," *J. Memb. Sci.*, vol. 350, no. 1–2, pp. 42–52, 2010.
- [139] S. Vives and C. Meunier, "Influence of the synthesis route on sol-gel SiO<sub>2</sub>–TiO<sub>2</sub> (1:1) xerogels and powders," 2006.
- [140] M. Shang, J. Tong, and R. O 'Hayre, "A novel wet-chemistry method for the synthesis of multicomponent nanoparticles A case study of BaCe<sub>0.7</sub>Zr<sub>0.1</sub>Y<sub>0.1</sub>Yb<sub>0.1</sub>O<sub>3-δ</sub>," *Mater. Lett.*, vol. 92, pp. 382–385, 2012.
- [141] H. Anderson, M. Nasrallah, F. Blum, and M. Smith, "Polymeric Synthesis of Perovskite Powders and Films," *NIST Spec. Publ.*, 1991.
- [142] W. A. Bassett, "Diamond anvil cell, 50th birthday," *High Press. Res.*, vol. 29, no. 2, pp. 163–186, Jun. 2009.
- [143] I. Spain and D. Dunstan, "The technology of diamond anvil high-pressure cells: II.

- Operation and use,” *J. Phys. E.*, vol. 22, pp. 913–923, 1989.
- [144] J. D. Barnett, S. Block, and G. J. Piermarini, “An Optical Fluorescence System for Quantitative Pressure Measurement in the Diamond Anvil Cell,” *Rev. Sci. Instrum.*, vol. 44, no. 1, pp. 1–9, Jan. 1973.
- [145] A. Jayaraman, “Diamond anvil cell and high-pressure physical investigations,” *Rev. Mod. Phys.*, vol. 55, no. 1, p. 65, 1983.
- [146] A. Jayaraman, “Ultrahigh pressures,” *Rev. Sci. Instrum.*, vol. 57, no. 41, 1986.
- [147] F. J. Manjón and D. Errandonea, “Pressure-induced structural phase transitions in materials and earth sciences,” *Phys. status solidi*, vol. 246, no. 1, pp. 9–31, Jan. 2009.
- [148] G. J. Piermarini, S. Block, and J. D. Barnett, “Hydrostatic limits in liquids and solids to 100 kbar,” *J. Appl. Phys.*, vol. 44, no. 12, pp. 5377–5382, 1973.
- [149] D. J. Dunstan and I. L. Spain, “Technology of diamond anvil high-pressure cells: I. Principles, design and construction,” *J. Phys. E.*, vol. 22, no. 11, pp. 913–923, Nov. 1989.
- [150] D. L. Decker, “Equation of State of NaCl and Its Use as a Pressure Gauge in High-Pressure Research,” *J. Appl. Phys.*, vol. 36, no. 1, p. 157, 1965.
- [151] D. L. Decker, “High-Pressure Equation of State for NaCl, KCl, and CsCl,” *J. Appl. Phys.*, vol. 42, no. 8, p. 3239, 1971.
- [152] R. N. Jeffery, J. D. Barnett, H. B. Vanfleet, H. T. Hall, and R. G. Wilson, “Pressure Calibration to 100 kbar Based on the Compression of NaCl,” *J. Appl. Phys.*, vol. 37, no. 8, 1966.
- [153] J. M. Brown, “The NaCl pressure standard,” *J. Appl. Phys.*, vol. 86, no. 92, 1999.
- [154] A. D. Chijioke, W. J. Nellis, A. Soldatov, and I. F. Silvera, “The ruby pressure standard to 150 GPa,” *J. Appl. Phys.*, vol. 98, no. 11, 2005.
- [155] K. Syassen, “Ruby under pressure,” *High Press. Res.*, vol. 28, no. 2, pp. 75–126, Jun. 2008.
- [156] G. C. J. Brown, “Fluorescence Lifetimes of Ruby,” *J. Appl. Phys.*, vol. 35, no. 158, pp. 3062–3063, 1964.
- [157] H. K. Mao, J. Xu, and P. M. Bell, “Calibration of the ruby pressure gauge to 800 kbar under quasi-hydrostatic conditions,” *J. Geophys. Res.*, vol. 91, no. B5, pp. 4673–4676, 1986.

- [158] H. Yamaoka, Y. Zekko, I. Jarrige, J.-F. Lin, N. Hiraoka, H. Ishii, K.-D. Tsuei, and J. Mizuki, "Ruby pressure scale in a low-temperature diamond anvil cell," *J. Appl. Phys.*, vol. 112, no. 12, p. 124503, Dec. 2012.
- [159] D. D. Ragan, R. Gustavsen, and D. Schiferl, "Calibration of the ruby R1 and R2 fluorescence shifts as a function of temperature from 0 to 600 K," *J. Appl. Phys.*, vol. 72, p. 5539, 1992.
- [160] M. Chai and J. Michael Brown, "Effects of static non-hydrostatic stress on the R lines of ruby single crystals," *Geophys. Res. Lett.*, vol. 23, no. 24, pp. 3539–3542, Dec. 1996.
- [161] S. M. Sharma and Y. M. Gupta, "Theoretical analysis of R-line shifts of ruby subjected to different deformation conditions," vol. 43, no. 1, 1991.
- [162] Q. Ma and D. R. Clarke, "Stress Measurement in Single-Crystal and Polycrystalline Ceramics Using Their Optical Fluorescence," *J. Am. Ceram. Soc.*, vol. 76, no. 6, pp. 1433–1440, Jun. 1993.
- [163] Q. Ma and D. R. Clarke, "Piezospectroscopic Determination of Residual Stresses in Polycrystalline Alumina," *J. Am. Ceram. Soc.*, vol. 77, no. 2, pp. 298–302, Feb. 1994.
- [164] J. He and D. R. Clarke, "Determination of the piezospectroscopic coefficients for chromium-doped sapphire," *Journal of the American Ceramic Society*, vol. 78, no. 5, pp. 1347–1353, May-1995.
- [165] H. K. Mao, P. M. Bell, J. W. Shaner, and D. J. Steinberg, "Specific volume measurements of Cu, Mo, Pd, and Ag and calibration of the ruby R1 fluorescence pressure gauge from 0.06 to 1 Mbar," *J. Appl. Phys.*, vol. 49, no. 6, pp. 3276–3283, Jun. 1978.
- [166] T. Kawamoto, K. N. Matsukage, T. Nagai, K. Nishimura, T. Mataka, S. Ochiai, and T. Taniguchi, "Raman spectroscopy of cubic boron nitride under high temperature and pressure conditions: A new optical pressure marker," *Rev. Sci. Instrum.*, vol. 75, pp. 2451–2454, 2004.
- [167] N. J. Hess and D. Schiferl, "Pressure and temperature dependence of laser-induced fluorescence of Sm:YAG to 100 kbar and 700 °C and an empirical model," *J. Appl. Phys.*, vol. 68, no. 5, p. 1953, 1990.
- [168] A. Lacam, "The SrB<sub>4</sub>O<sub>7</sub>:Sm<sup>2+</sup> optical sensor and the pressure homogeneization through thermal cycles in diamond anvil cells," *High Press. Res.*, vol. 5, no. 1–6, pp. 782–784, Apr. 1990.
- [169] A. Lacam and C. Chateau, "High-pressure measurements at moderate temperatures in a diamond anvil cell with a new optical sensor: SrB<sub>4</sub>O<sub>7</sub>:Sm<sup>2+</sup>," *J. Appl. Phys.*, vol. 66, no. 1, p. 366, 1989.



- [170] F. Dé, R. Datchi, P. Loubeyre, and R. Letoullec, “Extended and accurate determination of the melting curves of argon, helium, ice (H<sub>2</sub>O), and hydrogen (H<sub>2</sub>),” *Phys. Rev. B*, vol. 61, pp. 6535–6546, 2000.
- [171] D. Schiferl, M. Nicol, J. M. Zaug, S. K. Sharma, T. F. Cooney, S.-Y. Wang, T. R. Anthony, and J. F. Fleischer, “The diamond <sup>13</sup>C/<sup>12</sup>C isotope Raman pressure sensor system for high-temperature/pressure diamond-anvil cells with reactive samples,” *J. Appl. Phys.*, vol. 82, no. 7, pp. 3256–3265, Oct. 1997.
- [172] O. L. Anderson, D. G. Isaak, and S. Yamamoto, “Anharmonicity and the equation of state for gold,” *J. Appl. Phys.*, vol. 65, no. 4, p. 1534, 1989.
- [173] F. Datchi, A. Dewaele, P. Loubeyre, R. Letoullec, Y. Le Godec, and B. Canny, “Optical pressure sensors for high-pressure–high-temperature studies in a diamond anvil cell,” *High Press. Res.*, vol. 27, no. 4, pp. 447–463, 2007.
- [174] G. J. Piermarini, S. Block, J. D. Barnett, and R. A. Forman, “Calibration of the pressure dependence of the R1 ruby fluorescence line to 195 kbar,” *J. Appl. Phys.*, vol. 46, no. 6, p. 2774, Sep. 1975.
- [175] A. F. Goncharov, J. M. Zaug, J. C. Crowhurst, and E. Gregoryanz, “Optical calibration of pressure sensors for high pressures and temperatures,” *J. Appl. Phys.*, vol. 97, no. 9, p. 94917, May 2005.
- [176] S. L. Wunder and P. E. Schoen, “Pressure measurement at high temperatures in the diamond anvil cell,” *J. Appl. Phys.*, vol. 52, no. 6, pp. 3772–3775, 1981.
- [177] F. Datchi, R. LeToullec, and P. Loubeyre, “Improved calibration of the SrB<sub>4</sub>O<sub>7</sub>:Sm<sup>2+</sup> optical pressure gauge: Advantages at very high pressures and high temperatures,” *J. Appl. Phys.*, vol. 81, no. 8, p. 3333, 1997.
- [178] S. YAMAOKA, O. SHIMOMURA, and O. FUKUNAGA, “Simultaneous Measurements of Temperature and Pressure by the Ruby Fluorescence Line,” *Proc. Japan Acad. Ser. B Phys. Biol. Sci.*, vol. 56, no. 3, pp. 103–107, 1980.
- [179] J. C. Chervin, B. Canny, and M. Mancinelli, “Erratum: ‘ruby-spheres as pressure gauge for optically transparent high pressure cells,’” *High Press. Res.*, vol. 23, no. 4, pp. 493–493, Dec. 2003.
- [180] J. C. Chervin, B. Canny, and M. Mancinelli, “Ruby-spheres as pressure gauge for optically transparent high pressure cells,” *High Press. Res.*, vol. 23, no. 4, pp. 493–493, 2003.
- [181] S. Rekhi, L. Dubrovinsky, and S. Saxena, “Temperature-induced ruby fluorescence shifts up to a pressure of 15 GPa in an externally heated diamond anvil cell,” *HIGH Temp.*

- Press.*, vol. 31, no. 3, pp. 299–305, 1999.
- [182] J.-K. Hyun, S. M. Sharma, and Y. M. Gupta, “Ruby R-line shifts for shock compression along (1102),” *J. Appl. Phys. AIP Conf. Proc.*, vol. 84, no. 4, p. 1947, 1998.
- [183] F. Dé, R. Datchi, and B. Canny, “Raman spectrum of cubic boron nitride at high pressure and temperature,” *Physical*, vol. 69, p. 144106, 2004.
- [184] S. V. Rashchenko, A. Y. Likhacheva, and T. B. Bekker, “Preparation of a macrocrystalline pressure calibrant  $\text{SrB}_4\text{O}_7:\text{Sm}^{2+}$  suitable for the HP -HT powder diffraction,” *High Press. Res.*, vol. 33, no. 4, pp. 720–724, 2013.
- [185] R. Stefani, A. D. Maia, E. E. S. Teotonio, M. A. F. Monteiro, M. C. F. C. Felinto, and H. F. Brito, “Photoluminescent behavior of  $\text{SrB}_4\text{O}_7:\text{RE}^{2+}$  (RE=Sm and Eu) prepared by Pechini, combustion and ceramic methods,” *J. Solid State Chem.*, vol. 179, no. 4, pp. 1086–1092, Apr. 2006.
- [186] J. M. Leger, C. Chateau, and A. Lacam, “ $\text{SrB}_4\text{O}_7:\text{Sm}^{2+}$  pressure optical sensor: Investigations in the megabar range,” *J. Appl. Phys.*, vol. 68, no. 5, p. 2351, 1990.
- [187] R. J. Angel, M. Bujak, J. Zhao, G. D. Gatta, and S. D. Jacobsen, “Effective hydrostatic limits of pressure media for high-pressure crystallographic studies,” *J. Appl. Crystallogr.*, vol. 40, no. 1, pp. 26–32, Feb. 2007.
- [188] T. Kenichi, P. C. Sahu, K. Yoshiyasu, and T. Yasuo, “Versatile gas-loading system for diamond-anvil cells,” *Rev. Sci. Instrum.*, vol. 72, no. 10, p. 3873, 2001.
- [189] K. Takemura, “Evaluation of the hydrostaticity of a helium-pressure medium with powder x-ray diffraction techniques,” *J. Appl. Phys.*, vol. 89, no. 1, p. 662, 2001.
- [190] J. M. Besson and J. P. Pinceaux, “Melting of helium at room temperature and high pressure,” *Science*, vol. 206, no. 4422, pp. 1073–5, Nov. 1979.
- [191] T. Kenichi, “Bulk modulus of osmium: High-pressure powder x-ray diffraction experiments under quasihydrostatic conditions,” *Phys. Rev. B*, vol. 70, p. 12101, 2004.
- [192] R. T. Downs, C.-S. Zha, T. S. Duffy, and L. W. Finger, “The equation of state of forsterite to 17.2 GPa and effects of pressure media,” *Am. Mineral.*, vol. 81, pp. 51–55, 1996.
- [193] A. Lacam, M. Madon, and J. P. and Poirier, “Olivine glass and spinel formed in a heated, diamond-anvil high pressure cell,” *Nature*, vol. 2889, pp. 155–157, 1980.
- [194] W. Clegg, “Synchrotron chemical crystallography,” *J. Chem. Soc. Dalt. Trans.*, no. 19, pp. 3223–3232, 2000.

- [195] H. Winick and D. Sebastian, *Synchrotron radiation research*. Springer Science & Business Media, 2012.
- [196] W. Clegg, “Synchrotron chemical crystallography,” *J. Chem. Soc. Dalton Trans.*, no. 19, pp. 3223–3232, 2000.
- [197] A. Hammersley and others, “The FIT2D home page.” ESRF: Grenoble, 2009.
- [198] A. P. Hammersley, “Fit2d reference manual,” in *European Synchrotron Radiation Facility (ESRF) International Report No. EXP/AH/93-02*, 1993.
- [199] H. M. Rietveld and IUCr, “A profile refinement method for nuclear and magnetic structures,” *J. Appl. Crystallogr.*, vol. 2, no. 2, pp. 65–71, Jun. 1969.
- [200] J. T. White, “NICKEL OXIDE IN ZIRCONIA AND YTTRIA STABILIZED ZIRCONIA STUDIED WITH MAGNETOMETRY,” Colorado School of Mines, 2011.
- [201] I. C. Madsen and R. J. Hill, “Collection and Analysis of Powder Diffraction Data with Near-Constant Counting Statistics,” *J. Appl. Cryst.*, vol. 27, pp. 385–392, 1994.
- [202] K. Shankland, W. I. F. David, and D. S. Sivia, “Routine ab initio structure determination of chlorothiazide by X-ray powder diffraction using optimised data collection and analysis strategies,” *J. Mater. Chem.*, vol. 7, no. 3, pp. 569–572, 1997.
- [203] G. Caglioti, A. Paoletti, and F. P. Ricci, “Choice of collimators for a crystal spectrometer for neutron diffraction,” *Nucl. Instruments*, vol. 3, no. 4, pp. 223–228, Oct. 1958.
- [204] P. Thompson, D. E. Cox, J. B. Hastings, and IUCr, “Rietveld refinement of Debye–Scherrer synchrotron X-ray data from  $\text{Al}_2\text{O}_3$ ,” *J. Appl. Crystallogr.*, vol. 20, no. 2, pp. 79–83, Apr. 1987.
- [205] L. B. McCusker, R. B. Von Dreele, D. E. Cox, D. Louër, and P. Scardi, “Rietveld refinement guidelines,” *J. Appl. Crystallogr.*, vol. 32, no. 1, pp. 36–50, Feb. 1999.
- [206] D. S. Young, D. S. Young, B. S. Sachais, and L. C. Jefferies, “The Rietveld Method,” pp. 167–185, 1993.
- [207] B. H. Toby, “R factors in Rietveld analysis: How good is good enough?,” *Powder Diffr.*, vol. 21, no. 1, pp. 67–70, Mar. 2006.
- [208] B. H. Toby, IUCr, and B. I. D., “*EXPGUI*, a graphical user interface for *GSAS*,” *J. Appl. Crystallogr.*, vol. 34, no. 2, pp. 210–213, Apr. 2001.
- [209] A. C. Larson and R. B. Von Dreele, “GSAS (GENERAL STRUCTURE ANALYSIS

SYSTEM).” .

- [210] “[www.crystallography.net/cod/](http://www.crystallography.net/cod/).” .
- [211] L. W. Finger, D. E. Cox, A. P. Jephcoat, and IUCr, “A correction for powder diffraction peak asymmetry due to axial divergence,” *J. Appl. Crystallogr.*, vol. 27, no. 6, pp. 892–900, Dec. 1994.
- [212] H. Xu, P. J. Heaney, and G. H. Beall, “Phase transitions induced by solid solution in stuffed derivatives of quartz: A powder synchrotron XRD study of the  $\text{LiAlSiO}_4\text{-SiO}_2$  join,” *Am. Mineral.*, vol. 85, no. 7–8, pp. 971–979, Jul. 2000.
- [213] V. F. Lvovich, *Impedance spectroscopy: applications to electrochemical and dielectric phenomena*. John Wiley & Sons, Ltd., 2012.
- [214] S. Kochowski and K. Nitsch, “Description of the frequency behaviour of metal– $\text{SiO}_2$ –GaAs structure characteristics by electrical equivalent circuit with constant phase element,” *Thin Solid Films*, vol. 415, no. 1–2, pp. 133–137, Aug. 2002.
- [215] M. Rubat du Merac, I. E. Reimanis, and H.-J. Kleebe, “Electrochemical Impedance Spectroscopy of Transparent Polycrystalline Magnesium Aluminate ( $\text{MgAl}_2\text{O}_4$ ) Spinel,” *J. Am. Ceram. Soc.*, vol. 98, no. 7, pp. 2130–2138, Jul. 2015.
- [216] E. Barsoukov and E. J. Ross Macdonald, *Impedance Spectroscopy: Theory, Experiment, and Applications*. 2005.
- [217] J.-B. Jorcin, M. E. Orazem, N. Ere, and B. Tribollet, “CPE analysis by local electrochemical impedance spectroscopy,” *Electrochim. Acta*, vol. 51, pp. 1473–1479, 2006.
- [218] J. Ross Macdonald, “Note on the parameterization of the constant-phase admittance element,” *Solid State Ionics*, vol. 13, no. 2, pp. 147–149, 1984.
- [219] J.-H. Hwang, D. S. McLachlan, and T. O. Mason, “Brick Layer Model Analysis of Nanoscale-to-Microscale Cerium Dioxide,” *J. Electroceramics*, vol. 3, no. 1, pp. 7–16.
- [220] B. Horgan, “Investigating Grain Boundaries in  $\text{BaCuS}_{1-x}\text{Se}_x\text{F}$  Using Impedance Spectroscopy Author: Briony Horgan Physics Department Oregon State University Advisor: Dr . Janet Tate Oregon State University Submitted for review: 0 Contents,” Oregon State University Advisor:, 2004.
- [221] J. R. Macdonald, “Impedance Spectroscopy,” *Ann. Biomed. Eng.*, vol. 20, pp. 289–305, 1992.

- [222] J. S. Tse and D. D. Klug, “Structural Memory in Pressure-Amorphized  $\text{AlPO}_4$ ,” *Science* (80- ), vol. 255, no. 5051, pp. 1559–1561, 1992.
- [223] B. Narayanan, I. E. Reimanis, and C. V Ciobanu, “Atomic-scale mechanism for pressure-induced amorphization of  $\beta$ -eucryptite,” *J. Appl. Phys.*, vol. 114, no. 8, p. 83520, Aug. 2013.
- [224] B. Narayanan, I. E. Reimanis, H. Huang, and C. V. Ciobanu, “Radiation effects and tolerance mechanism in  $\beta$ -eucryptite,” *J. Appl. Phys.*, vol. 113, no. 3, p. 33504, Jan. 2013.
- [225] T. Shimada, M. Mizuno, K. Kurachi, N. Kato, O. Sakurada, M. Hashiba, and Y. Nurishi, “Simultaneous fabrication of a composite with low thermal expansion and high strength in the eucryptite-yttria-stabilized PSZ system,” *J. Mater. Sci.*, vol. 31, pp. 3691–3695, 1996.
- [226] Z. Quan, Y. Wang, I. T. Bae, W. S. Loc, C. Wang, Z. Wang, and J. Fang, “Reversal of hall-petch effect in structural stability of PbTe nanocrystals and associated variation of phase transformation,” *Nano Lett.*, vol. 11, no. 12, pp. 5531–5536, Dec. 2011.
- [227] Z. Wang, O. Chen, C. Y. Cao, K. Finkelstein, D.-M. Smilgies, X. Lu, and W. A. Bassett, “Integrating in situ high pressure small and wide angle synchrotron x-ray scattering for exploiting new physics of nanoparticle supercrystals,” *Rev. Sci. Instrum.*, vol. 81, no. 9, p. 93902, Sep. 2010.
- [228] “<http://www.materialsproject.org>.” [Online]. Available: <http://www.materialsproject.org>.
- [229] J. P. Perdew, K. Burke, and M. Ernzerhof, “Generalized Gradient Approximation Made Simple,” vol. 77, 1996.
- [230] G. Kresse and J. Furthmüller, “Efficient iterative schemes for ab initio total-energy calculations using a plane-wave basis set,” *Phys. Rev. B*, vol. 54, no. 16, pp. 11169–11186, Oct. 1996.
- [231] “L. Lutterotti, MAUD, version 2.55 released April 30, 2015, <http://www.ing.unitn.it/~luttero/maud>.” .
- [232] L. Lutterotti, P. Scardi, and P. Maistrelli, “LSI - a computer program for simultaneous refinement of material structure and microstructure,” *J. Appl. Crystallogr.*, vol. 25, no. 3, pp. 459–462, Jun. 1992.
- [233] F. Sánchez-Bajo and F. L. Cumbreira, “The Use of the Pseudo-Voigt Function in the Variance Method of X-ray Line-Broadening Analysis,” *J. Appl. Crystallogr.*, vol. 30, no. 4, pp. 427–430, Aug. 1997.
- [234] E. T. Hahn, “International Tables for Crystallography,” in *International Tables for Crystallography*, 2005, pp. 191–31.

- [235] J. Barbier, N. Penin, A. Denoyer, and L. M. D. Cranswick, "BaBiBO<sub>4</sub>, a novel non-centrosymmetric borate oxide," *Solid State Sci.*, vol. 7, no. 9, pp. 1055–1061, Sep. 2005.
- [236] A. F. Goncharov, M. R. Manaa, J. M. Zaug, R. H. Gee, L. E. Fried, and W. B. Montgomery, "Polymerization of formic acid under high pressure," *Phys. Rev. Lett.*, vol. 94, no. 6, p. 65505, Feb. 2005.
- [237] Y. Chen, Z. Wang, C. V. Ciobanu, and I. E. Reimanis, "Grain size effect on the pressure induced phase transformation of  $\beta$ -euryptite," *J. Am. Ceram. Soc.*, p. To be submitted.
- [238] A. H. Heuer, F. F. Lange, M. V. Swain, and A. G. Evans, "Transformation Toughening: An Overview," *J. Am. Ceram. Soc.*, vol. 69, no. 3, Mar. 1986.
- [239] A. H. HEUER, "Transformation Toughening in ZrO<sub>2</sub>-Containing Ceramics," *J. Am. Ceram. Soc.*, vol. 70, no. 10, pp. 689–698, Oct. 1987.
- [240] W. M. Kriven, "The transformation mechanism of spherical zirconia particles in alumina," *Adv. Ceram.*, vol. 12, pp. 64–77, 1984.
- [241] R. S. Hay, E. E. Boakye, P. Mogilevsky, G. E. Fair, T. A. Parthasarathy, and J. E. Davis, "Transformation Plasticity in (Gd<sub>x</sub>Dy<sub>1-x</sub>)PO<sub>4</sub> Fiber Coatings During Fiber Push Out," *J. Am. Ceram. Soc.*, vol. 96, no. 5, pp. 1586–1595, May 2013.
- [242] R. S. Hay, E. E. Boakye, and P. Mogilevsky, "Transformation plasticity in TbPO<sub>4</sub> and (Gd,Dy)PO<sub>4</sub> orthophosphates during indentation of polycrystalline specimens," *J. Eur. Ceram. Soc.*, vol. 34, pp. 773–781, 2014.
- [243] R. S. Hay, P. Mogilevsky, and E. Boakye, "Phase transformations in xenotime rare-earth orthophosphates," *Acta Mater.*, vol. 61, no. 18, pp. 6933–6947, 2013.
- [244] A. Lai, Z. Du, C. L. Gan, and C. A. Schuh, "Shape Memory and Superelastic Ceramics at Small Scales," *Science (80-. )*, vol. 341, no. 6153, 2013.
- [245] M. V. Swain, "Shape memory behaviour in partially stabilized zirconia ceramics," *Nature*, vol. 322, no. 6076, pp. 234–236, Jul. 1986.
- [246] P. E. REYES-MOREL, J.-S. CHERNG, and I.-W. CHEN, "Transformation Plasticity of CeO<sub>2</sub>-Stabilized Tetragonal Zirconia Polycrystals: II, Pseudoelasticity and Shape Memory Effect," *J. Am. Ceram. Soc.*, vol. 71, no. 8, pp. 648–657, Aug. 1988.
- [247] P. M. Kelly and L. R. F. Rose, "The martensitic transformation in ceramics - Its role in transformation toughening," *Progress in Materials Science*, vol. 47, no. 5, pp. 463–557, 2002.

- [248] J. Tang, T. Zhang, P. Zoogman, J. Fabbri, S. W. Chan, Y. M. Zhu, L. E. Brus, and M. L. Steigerwald, "Martensitic phase transformation of isolated  $\text{HfO}_2$ ,  $\text{ZrO}_2$ , and  $\text{Hf}_x\text{Zr}_{1-x}\text{O}_2$  ( $0 < x < 1$ ) nanocrystals," *Adv. Funct. Mater.*, vol. 15, no. 10, pp. 1595–1602, Oct. 2005.
- [249] M. P. Pasternak, G. K. Rozenberg, A. P. Milner, M. Amanowicz, T. Zhou, U. Schwarz, K. Syassen, R. Dean Taylor, M. Hanfland, and K. Brister, "Pressure-Induced Concurrent Transformation to an Amorphous and Crystalline Phase in Berlinite-Type  $\text{FePO}_4$ ," *Phys. Rev. Lett.*, vol. 79, no. 22, pp. 4409–4412, Dec. 1997.
- [250] Z. Wang, S. K. Saxena, V. Pischedda, H. P. Liermann, and C. S. Zha, "In situ x-ray diffraction study of the pressure-induced phase transformation in nanocrystalline  $\text{CeO}_2$ ," *Phys. Rev. B*, vol. 64, no. 1, p. 12102, Jun. 2001.
- [251] A. H. Heuer, M. Ruhle, and D. B. Marshall, "On the Thermoelastic Martensitic Transformation in Tetragonal Zirconia," *J. Am. Ceram. Soc.*, vol. 73, no. 4, pp. 1084–1093, Apr. 1990.
- [252] S. H. Tolbert and A. P. Alivisatos, "The wurtzite to rock salt structural transformation in  $\text{CdSe}$  nanocrystals under high pressure," *J. Chem. Phys.*, vol. 102, no. 11, p. 4642, 1995.
- [253] S. H. Tolbert and A. P. Alivisatos, "High-Pressure structural transformations in semiconductor nanocrystals," *Annu. Rev. Phys. Chem.*, vol. 46, no. 46, pp. 595–625, 1995.
- [254] S. Tolbert and A. Alivisatos, "Size dependence of a first order solid-solid phase transition: the wurtzite to rock salt transformation in  $\text{CdSe}$  nanocrystals," *Sci. YORK THEN*, 1994.
- [255] B. Morosin and P. S. Peercy, "Pressure-induced phase transition in beta-eucryptite," *Phys. Lett. A*, vol. 53, no. 2, pp. 147–148, Jun. 1975.
- [256] S. B. Qadri, E. F. Skelton, D. Hsu, A. D. Dinsmore, J. Yang, H. F. Gray, and B. R. Ratna, "Size-induced transition-temperature reduction in nanoparticles of  $\text{ZnS}$ ," *Phys. Rev. B*, vol. 60, no. 13, pp. 9191–9193, Oct. 1999.
- [257] E. Haussühl, J. Schreuer, B. Winkler, S. Haussühl, L. Bayarjargal, and V. Milman, "Structure–property relations and thermodynamic properties of monoclinic petalite,  $\text{LiAlSi}_4\text{O}_{10}$ ," *J. Phys. Condens. Matter*, vol. 24, no. 34, p. 345402, Aug. 2012.
- [258] W. A. Bassett, T. Takahashi, H.-K. Mao, and J. S. Weaver, "Pressure-Induced Phase Transformation in  $\text{NaCl}$ ," *J. Appl. Phys.*, vol. 39, no. 1, pp. 319–325, 1968.
- [259] E. König, I. G. Ritter, I. S. K. Kulshreshtha, I. J. Waigel, and H. A. Goodwin2, "Hysteresis Effects, Concurrent Crystallographic Phase Change, Entropy of the Transition, and Effect of Pressure," *Inorg. Chem*, vol. 23, pp. 1896–1902, 1984.
- [260] M. Akaogi and E. Ito, "Calorimetric study on majorite-perovskite transition in the system

- Mg<sub>4</sub>Si<sub>4</sub>O<sub>12</sub>-Mg<sub>3</sub>Al<sub>2</sub>Si<sub>3</sub>O<sub>12</sub>: transition boundaries with positive pressure-temperature slopes,” *Phys. Earth Planet. Inter.*, vol. 114, pp. 129–140, 1999.
- [261] G. A. Parks, “Surface and interfacial free energies of quartz,” *J. Geophys. Res. Solid Earth*, vol. 89, no. B6, pp. 3997–4008, Jun. 1984.
- [262] G. a. Parks, “Surface and interfacial free energies of quartz,” *J. Geophys. Res.*, vol. 89, no. B6, p. 3997, 1984.
- [263] S. Krijt, C. Güttler, D. Heißelmann, C. Dominik, and a G. G. M. Tielens, “Energy dissipation in head-on collisions of spheres,” *J. Phys. D. Appl. Phys.*, vol. 46, no. 43, p. 435303, 2013.
- [264] Y. Chen, S. Manna, C. V. Ciobanu, and I. E. Reimanis, “Thermal regimes of Li-ion conductivity of β-eucryptite,” *J. Am. Ceram. Soc.*, p. To be submitted.
- [265] R. A. EPPLER, “Glass Formation and Recrystallization in the Lithium Metasilicate Region of the System Li<sub>2</sub>O-Al<sub>2</sub>O<sub>3</sub>-SiO<sub>2</sub>,” *J. Am. Ceram. Soc.*, vol. 46, no. 2, pp. 97–101, Feb. 1963.
- [266] F. A. Hummel, “Thermal Expansion Properties of Some Synthetic Lithia Minerals,” *J. Am. Ceram. Soc.*, vol. 34, no. 8, pp. 235–239, Aug. 1951.
- [267] H. Schulz, “Thermal expansion of beta eucryptite,” *J. Am. Ceram. Soc.*, vol. 1973, no. July, pp. 313–318, Jul. 1974.
- [268] B. Narayanan, I. E. Reimanis, E. R. Fuller, and C. V Ciobanu, “Elastic constants of beta-eucryptite: A density functional theory study,” *Phys. Rev. B*, vol. 81, no. 10, pp. 1–7, Mar. 2009.
- [269] B. Morosin and R. T. Johnson Jr., “Solid Electrolyte Materials,” *Sandia Lab. Rep. SAND74-0296*, 1974.
- [270] R. M. Biefeld, R. T. Johnson, and R. J. Baughman, “Effects of Composition Changes, Substitutions, and Hydrostatic Pressure on the Ionic Conductivity in Lithium Aluminosilicate and Related Beta - Eucryptite Materials,” *J. Electrochem. Soc.*, vol. 125, no. 2, pp. 179–185, Feb. 1978.
- [271] W. van Gool and D. D. Yue, “Fast Ion Transport in Solids, Solid State Batteries and Devices,” *J. Electrochem. Soc.*, vol. 121, no. 4, p. 154C, 1974.
- [272] R. A. Hatch, “Phase equilibrium in the system: Li<sub>2</sub>O-Al<sub>2</sub>O<sub>3</sub>-SiO<sub>2</sub>,” *Am. Mineral.*, vol. 28, no. 9 and 10, pp. 471–496, 1943.



- [273] W. F. Müller, “The effect of heating on the domain structure of beta-eucryptite,  $\text{LiAlSiO}_4$ ,” *J. Mater. Sci.*, vol. 14, no. 6, pp. 1433–1439, Jun. 1979.
- [274] D. Johnson, “ZPlot, ZView Electrochemical Impedance Software, Version 2.3b, Scribner Associates Inc.” 2000.
- [275] Y. Kim, D.-K. Shin, E.-C. Shin, H.-H. Seo, and J.-S. Lee, “Oxide ion conduction anisotropy deconvoluted in polycrystalline apatite-type lanthanum silicates,” *J. Mater. Chem.*, vol. 21, p. 2940, 2011.
- [276] E. Barsoukov and J. R. Macdonald, *Impedance Spectroscopy: Theory, Experiment, and Applications*. 2005.
- [277] M. VERKERK, B. MIDDELHUIS, and A. BURGGRAAF, “Effect of grain boundaries on the conductivity of high-purity  $\text{ZrO}_2\text{-Y}_2\text{O}_3$  ceramics,” *Solid State Ionics*, vol. 6, no. 2, pp. 159–170, Mar. 1982.
- [278] H. L. Tuller, “Ionic conduction in nanocrystalline materials,” *Solid State Ionics*, vol. 131, pp. 143–157, 2000.
- [279] J. E. Bauerle, “Study of solid electrolyte polarization by a complex admittance method,” *Solid State Commun.*, vol. 7, no. 15, p. ii, 1969.
- [280] J. T. S. Irvine, D. C. Sinclair, and A. R. West, “Electroceramics: Characterization by Impedance Spectroscopy,” *Adv. Mater.*, vol. 2, no. 3, pp. 132–138, Mar. 1990.
- [281] S. M. Haile, C. R. I. Chisholm, K. Sasaki, D. A. Boysenw, and T. Udaz, “Solid acid proton conductors: from laboratory curiosities to fuel cell electrolytes,” *Faraday Discuss.*, vol. 134, pp. 17–39, 2007.
- [282] Y. Liao, P. Singh, K.-S. Park, W. Li, and J. B. Goodenough, “ $\text{Li}_6\text{Zr}_2\text{O}_7$  interstitial lithium-ion solid electrolyte,” *Electrochim. Acta*, vol. 102, pp. 446–450, Jul. 2013.
- [283] A. Mei, X. Wang, Y. Feng, S. Zhao, G. Li, H. Geng, Y. Lin, and C. Nan, “Enhanced ionic transport in lithium lanthanum titanium oxide solid state electrolyte by introducing silica,” *Solid State Ionics*, vol. 179, no. 39, pp. 2255–2259, Dec. 2008.
- [284] K. Chen, M. Huang, Y. Shen, Y. Lin, and C. W. Nan, “Enhancing ionic conductivity of  $\text{Li}_{0.35}\text{La}_{0.55}\text{TiO}_3$  ceramics by introducing  $\text{Li}_7\text{La}_3\text{Zr}_2\text{O}_{12}$ ,” *Electrochim. Acta*, vol. 80, pp. 133–139, Oct. 2012.
- [285] B. Narayanan, I. E. Reimanis, E. R. Fuller Jr., and C. V. Ciobanu, “Elastic constants of beta-eucryptite: A density functional theory study,” *Phys. Rev. B*, vol. 81, no. 10, Mar. 2010.

- [286] S. Nara, K. Yoshimitsu, and T. Matsubara, "Phenomenological Theory of Phase Transition in Beta-Eucryptite," *Prog. Theor. Phys.*, vol. 66, no. 4, pp. 1143–1159, Oct. 1981.
- [287] R. Sprengard, K. Binder, M. Brändle, U. Fotheringham, J. Sauer, and W. Pannhorst, "On the interpretation of the experimental Raman spectrum of  $\beta$ -eucryptite  $\text{LiAlSiO}_4$  from atomistic computer modeling," *J. Non. Cryst. Solids*, vol. 274, no. 1–3, pp. 264–270, Sep. 2000.

## APPENDIX A

### TRANSPORT IN AN ELECTRICAL POTENTIAL GRADIENT

Particle electrical conductivity of the species  $i$  is defined as:

$$\sigma_i = z_i e c_i \mu_i \quad (\text{A.1})$$

where

$i$  – charged particle type (ions and electrons)

$z_i e$  – charge of charged particle

$\mu_i$  – particle mobility

$c_i$  – concentration

The particle mobility can also be written as a relation with particle mechanical mobility

(B<sub>i</sub>):

$$\mu_i = z_i e B_i \quad (\text{A.2})$$

The relation between the random diffusion coefficient of particles of type  $i$  and the particle's mobility is given by:

$$D_i = k T B_i \quad (\text{A.3})$$

By replacing  $B_i$  in Equ. B.3 with Equ. B.1 and Equ. B.2, the diffusion coefficient can be written as:

$$D_i = k T B_i = \frac{\mu_i k T}{z_i e} = \frac{\sigma_i k T}{c_i z_i^2 e^2} \quad (\text{A.4})$$

Thus, Nernst-Einstein relation between mobility and diffusion coefficient is obtained as:

$$\sigma_i = \frac{(z_i e)^2 c_i D_i}{kT} \quad (\text{A.5})$$

Generally, diffusion coefficient follows an Arrhenius law because it is an activated process:

$$D = D_0 \exp\left(\frac{-E_a}{kT}\right) \quad (\text{A.6})$$

From equation A.5, one can tell that mobility ( $\sigma$ ) is proportional to  $D/T$ , thus,  $(\sigma T)$  follows an Arrhenius law. This indicates that in hopping mechanisms, it is necessary to plot  $\log(\sigma T)$  vs.  $1/T$  instead of  $\log(\sigma)$  vs.  $1/T$ . However, the equation  $\sigma = \sigma_0 \exp\left(\frac{-E_a}{kT}\right)$  is often used in polymer or liquids at very low temperatures.